

Title	Fabrication, characterisation and electroanalysis at 1-dimensional nanostructures
Authors	Wahl, Amélie
Publication date	2013
Original Citation	Wahl, A. J. C. 2013. Fabrication, characterisation and electroanalysis at 1-dimensional nanostructures . PhD Thesis, University College Cork.
Type of publication	Doctoral thesis
Rights	© 2014, Amélie J. C. Wahl - <a href="http://creativecommons.org/licenses/by-nc-nd/3.0/">http://creativecommons.org/licenses/by-nc-nd/3.0/</a>
Download date	2024-04-19 14:31:30
Item downloaded from	<a href="https://hdl.handle.net/10468/1740">https://hdl.handle.net/10468/1740</a>

Ollscoil na hÉireann  
NATIONAL UNIVERSITY OF IRELAND



# **Fabrication, Characterisation and Electroanalysis at 1-Dimensional Nanostructures**

A Thesis Presented to  
the National University of Ireland  
for the degree of Doctor of Philosophy  
by  
**Amélie Wahl**

*Supervised by Dr Alan O’Riordan*



Department of Chemistry  
&  
Tyndall National Institute  
University College Cork  
December 2013





## **Declaration**

I hereby declare that this thesis is my own work and certify to the best of my knowledge it contains no materials previously published or written by another person, or substantial proportions of material which have been accepted for the award of any other degree or diploma at University College Cork or any other educational institution, except where due acknowledgement is made in the thesis in accordance with the standard referencing practices. Any contribution made to the research by others, with whom I have worked directly at University College Cork or Tyndall National Institute or elsewhere, is explicitly acknowledged in the thesis. I also declare that the intellectual content of this thesis is the product of my own work, except to the extent that assistance from others in the project's design and conception or in style, presentation and linguistic expression is acknowledged.

I declare that this is a true copy of my thesis, including any final revisions, as approved by my thesis committee and the Graduate Studies office, and that this thesis has not been submitted to any other University or Institution.

Amélie Wahl



# Table of Contents

## **Chapter 1: Introduction**

1.1 Overview of Fundamental Concepts of Electrochemistry.....	3
1.1.1 Experimental Set-up.....	3
1.1.2 Electron Transfer.....	5
1.1.3 Faradaic and Non-faradaic Currents.....	6
1.1.4 Factors Affecting the Faradaic Response.....	8
1.1.5 Voltammetric Techniques to Study Electrode Reactions.....	15
1.2 Electroanalysis at the Nanoscale.....	18
1.2.1 From Microelectrodes via Ultra-microelectrodes to Nanoelectrodes.....	19
1.2.2 Nanoelectrodes.....	20
1.2.3 Nanoelectrode Fabrication .....	21
1.3 Mass Transport Simulation Overview.....	28
1.3.1 Finite Element Method.....	28
1.3.2 COMSOL Multiphysics®.....	29
1.3.3 Simulation of Mass Transport.....	30
1.4 Scope of Thesis.....	35

## **Chapter 2: Fabrication, Assembly and Characterisation of Platinum/Cobalt-Platinum Segmented Nanowires at Technology Relevant Silicon Chip Substrates**

2.1 Introduction.....	44
2.2 Experimental.....	46
2.2.1 Synthesis of Platinum Nanowires with a Cobalt-Platinum Tip.....	46
2.2.2 Structural Characterisation of Pt/CoPt Nanowires.....	47
2.2.3 Elemental Characterisation of Pt/CoPt Nanowires.....	47
2.2.5 Pt/CoPt Nanowires Assembly, Integration and Packaging.....	48
2.2.5 Electrical Characterisation of Pt/CoPt Nanowire Electrodes.....	49
2.2.6 Electrochemical Characterisation.....	50
2.2.7 Chemicals and Glassware.....	50
2.3 Results and Discussion.....	51

2.3.1	Morphological Analysis of Commercial Anodic Alumina Oxide Templates.....	51
2.3.2	Structural Characterisation.....	51
2.3.3	Elemental Characterisation.....	52
2.3.4	Robotic Assembly Approach.....	54
2.3.5	Self-Assembly Approach.....	57
2.3.6	Pt/CoPt Nanowire Device Integration.....	59
2.3.7	Electrical Characterisation of Pt/CoPt Nanowire Electrodes.....	60
2.3.8	Electrochemical Characterisation.....	61
2.4	Summary and Conclusion.....	63
2.5	References.....	64

**Chapter 3: Comparative Electroanalysis at Single Gold Nanowires Fabricated by Electron-beam Lithography and at Single Commercial Gold Ultra-microdisc Electrodes**

3.1	Introduction.....	66
3.2	Experimental.....	69
3.2.1	Nanowire Electrode Design.....	69
3.2.2	Nanowire Fabrication.....	69
3.2.3	Nanowire Electrochemical Cell Set-up.....	71
3.2.4	Nanowire Structural and Electrical Characterisation.....	72
3.2.5	Electroanalysis at Nanowire Electrodes.....	72
3.2.6	Electroanalysis at Ultra-microdisc Electrodes.....	73
3.2.7	Finite-Element Simulation.....	74
3.2.8	Chemicals and Glassware.....	75
3.3	Results and Discussion.....	76
3.3.1	Electrodes Structural Characterisation.....	76
3.3.2	Nanowire Electrical Characterisation.....	77
3.3.3	Experimental Estimation of the Diffusion Coefficient.....	78
3.3.4	Electrochemical Signal Enhancement at the Nanoscale.....	82
3.3.5	Rapid Analysis at the Nanoscale.....	83
3.4	Summary and Conclusion.....	90
3.5	References.....	91

## **Chapter 4: Electroanalysis at Gold Nanowires Arrays: Simulation Study and Electrochemical Experiments**

4.1 Introduction.....	94
4.2 Experimental.....	97
4.2.1 Finite-Element Simulations.....	97
4.2.2 Nanowire Electrode Array Design, Fabrication and Cell Set-up.....	97
4.2.3 Nanowire Arrays Structural and Electrical Characterisation.....	97
4.2.4 Electrochemical analysis.....	98
4.2.5 Chemicals and Glassware.....	98
4.3 Results and Discussion.....	99
4.3.1 Simulation at Nanowire Electrode Arrays: Assessment of the Inter-electrode Separation.....	99
4.3.2 Nanowire Electrode Arrays Fabrication and Structural Characterisation	
4.3.3 Nanowire Electrode Arrays Electrical Characterisation.....	102
4.3.4 Cyclic Voltammetry at Nanowire Electrode Arrays: Assessment of the Inter-electrode Separation.....	103
4.3.5 Signal Enhancement at Nanowire Arrays vs. Single Nanowire.....	104
4.3.6 Determination of Heterogeneous Kinetics.....	106
4.3.7 Square Wave Voltammetry at Nanowire Electrode Arrays.....	107
4.4 Summary and Conclusion.....	109
4.5 References.....	110

## **Chapter 5: Electroanalysis at Single Gold Nanowires and Arrays of Two, Three and Four Gold Nanowires: Sensing Applicability Enhancement with Increasing Nanowire Population**

5.1 Introduction.....	113
5.2 Experimental.....	115
5.2.1 Finite-Element Simulations.....	115
5.2.2 Nanowire Electrode Array Design, Fabrication and Cell Set-up.....	115
5.2.3 Nanowire Structural and Electrical Characterisation.....	115
5.2.4 Electrochemical analysis.....	116
5.2.5 Chemicals and Glassware.....	116
5.3 Results and Discussion.....	117

5.3.1	Simulations: Optimisation of the Inter-electrode Separation.....	117
5.3.2	Nanowire Electrodes Fabrication and Structural Characterisation.....	119
5.3.3	Nanowire Electrodes Electrical Characterisation.....	120
5.3.4	Cyclic Voltammetry: Optimisation of the Inter-electrode Separation...	121
5.3.5	Signal Enhancement at Nanowire Arrays vs. Single Nanowire Electrode	
5.3.6	Ultra-Rapid Analysis at Nanowire and Nanowire Arrays.....	123
5.4	Summary and Conclusion.....	126
5.5	References.....	127

## ***Chapter 6: Summary, Conclusion and Future Work***

6.1	Summary and Conclusion.....	130
6.2	Future Work.....	133

<i>Appendices</i> .....	135
-------------------------	-----

## Acknowledgments

Firstly, I would like to thank Dr. Alan O’Riordan for giving me the opportunity to read for a doctorate in Chemistry within the Nanotechnology group. I am grateful to Alan for his support, enthusiasm, encouragement and all the scientific and non-science related things he taught me. This thesis includes many examples of the scientific point of view. Non-scientific things principally are new expressions or words, principally Cork slang. For instance @\$##, or %!!\*@\* and \$\$\$%&\*!!’# are new words in my English vocabulary. I think of Alan as a good scientist and a good person.

I also would like to thank the other supervisors and post docs of the Nanotechnology group for their advice, their time whenever I needed it and their kindness: Dr. Aidan Quinn, Dr. Hugh Doyle, Dr Daniela Iacopino, Dr Brenda Long, Dr. Mary Manning, Dr Claire Barrett, Dr. Pierre Lovera, Dr Nicolas Sassiati, Dr Karen Dawson, Dr Micheál Burke (Mimi), Dr Alessio Miranda and Dr Armelle Montrose. Special thanks to Brenda and Mimi for all the support, advice, fun and for the true and lasting friendship we have. Also special thanks to Karen and Pierre, with whom I directly worked over the years and also had some good craic. By the way, I am a big fan of Pierre’s wicked sense of humour and I really enjoyed working with him. Pierre ‘est magique’ like Paris Saint Germain with Zlatan Ibrahimovic.

A big, huge, enormous, giant, massive thanks or as Ethel would say ‘Thanks a million’ to all of my co-students within the Nanotechnology Group for the great and amazeballs craic in the lab but most importantly at tea/coffee breaks, lunch breaks and during nights out: Alfonso (‘fantastic’), Andrea (the brain), Carola (the creative and talented girl), Colm (Ginger Puffo), Daniel J. (Jesus), Daniel L. (Baby Dan), Darragh (Keith’s sausage, also known as Gintin or Giny because of his famous strawberry blond hair styled with gel à la Tintin), Ethel (who would do pretty much anything if you give her chocolate), John (Is he still alive? Oh yes, there he is.), Keith (lost without his sausage), Marcus (the new guy), Micki (my peanut butter or jelly, I don’t remember which one of us is which), Niamh (the supermodel), Roxane (exotic girl...from Corsica) and Seán (my Babes). I know I made some true friends.

I also would like to thank the members of the extended Tyndall team whom I worked and collaborated with, particularly to Dan O’Connell, Alan Blake, Donal O’Sullivan, Vladimir Djara, Brendan McCarthy and Richard Murphy for the fabrication of the electron-beam/photolithography nanowires and for the sample holder.

Huge thanks to the Tyndall Tag rugby team ‘Tyndall Tacklers’: Rosemary, Marie, Sharon, Lisa, Patricia, Lida, Marco, Darragh, Alfonso, Aidan, Seán, Rick, Brian, Pierre, Tristan, Charlie, Niall, Cormac ... and all those that I have forgotten. I had so much fun discovering and playing this game.

Huge thanks to my belote team, with whom I really enjoyed playing cards on a regular basis: Tony, Nanto, Florent, Fred, Pierre.

Thanks to all the staff in Cavanagh’s (my second home), in particular: Sean the best barman in Cork, Tom and John.

Huge thanks to the best housemates and now great friends in ‘Blarney mansion’ Patrycja, Lauriane and Iago. I will always remember those crazy and amazing years together. Random memories include: ‘we love cleaning’, ‘immmmmmediately’, ‘we lost the balls’, crazy Tuesdays, ‘hangover 3’. I also would like to include Cyrille as a great friend and a neighbour from the Blarney mansion. And other friends, on whom I could always count on: Rozenn, Julia, Chris, Caro, Solène, Amélie, Camille, Momo, Robert, Pete, Tara, Tristan, ... and again sorry to those that I am forgetting.

Gigantic thanks to my parents, Chantale and Klaus, who have always supported me ever since I was born. I would not be where I am today without their love. I thereby also would like to thank my twin brother, Bastian, and my other siblings, Samuel and Léonie, as much as my parents, for their love and support. Merci beaucoup beaucoup & vielen vielen dank.

And finally, I would like to thank Seán for his support, love, great sense of humour and amazing ability to calm me down in any stressful period. You are my best friend, mon amour, my everything: nice Juan babes.





## Abstract

Integrated nanowire electrodes that permit direct, sensitive and rapid electrochemical based detection of chemical and biological species are a powerful emerging class of sensor devices. As critical dimensions of the electrodes enter the nanoscale, radial analyte diffusion profiles to the electrode dominate with a corresponding enhancement in mass transport, steady-state sigmoidal voltammograms, low depletion of target molecules and faster analysis. To optimise these sensors it is necessary to fully understand the factors that influence performance limits including: electrode geometry, electrode dimensions, electrode separation distances (within nanowire arrays) and diffusional mass transport. Therefore, in this thesis, theoretical simulations of analyte diffusion occurring at a variety of electrode designs were undertaken using Comsol Multiphysics®. Sensor devices were fabricated and corresponding experiments were performed to challenge simulation results. Two approaches for the fabrication and integration of metal nanowire electrodes are presented: Template Electrodeposition and Electron-Beam Lithography. These approaches allow for the fabrication of nanowires which may be subsequently integrated at silicon chip substrates to form fully functional electrochemical devices. Simulated and experimental results were found to be in excellent agreement validating the simulation model.

The electrochemical characteristics exhibited by nanowire electrodes fabricated by electron-beam lithography were directly compared against electrochemical performance of a commercial ultra-microdisc electrode. Steady-state cyclic voltammograms in ferrocenemonocarboxylic acid at single ultra-microdisc electrodes were observed at low to medium scan rates ( $\leq 500 \text{ mV}\cdot\text{s}^{-1}$ ). At nanowires, steady-state responses were observed at ultra-high scan rates (up to  $50,000 \text{ mV}\cdot\text{s}^{-1}$ ), thus allowing for much faster analysis (20 ms). Approaches for elucidating faradaic signal without the requirement for background subtraction were also developed. Furthermore, diffusional process occurring at arrays with increasing inter-electrode distance and increasing number of nanowires were explored. Diffusion profiles existing at nanowire arrays were simulated with Comsol Multiphysics®. A range of scan rates were modelled, and experiments were undertaken at  $5,000 \text{ mV}\cdot\text{s}^{-1}$  since this allows rapid data capture required for, e.g., biomedical, environmental and pharmaceutical diagnostic applications.



*To my parents: Chantale and Klaus  
& to my brothers and sister: Bastian, Samuel and Léonie*



# *Chapter 1*

## **Introduction**



In recent years, sensors based on electrochemical detection techniques have received increased interest worldwide because of their relative simplicity and lower related cost, compared to other conventional analytical techniques such as spectroscopic or chromatographic methods. Furthermore, advances in micro and nanofabrication methodologies have triggered the development of miniaturised electrochemical sensor devices, which employ electrodes as sensing elements. In this regard, nanoelectrodes are the next step in the miniaturisation of sensors for electrochemical applications. Therefore, the objective of this thesis is to explore nanowire fabrication methods to progressively develop novel nanowire-based electrochemical sensor devices.

In this introduction chapter, a general overview of fundamental concepts in electrochemistry is given. It should help non-electrochemist understand the following chapters. This is followed by a summary of electroanalysis at the nanoscale, principally describing mass transport behaviour at nanoelectrodes and nanowire fabrication approaches. Then, simulations regarding mass transport behaviour are described. Finally, the scope of this thesis is detailed.

## 1.1 Overview of Fundamental Concepts of Electrochemistry

Broadly speaking, electrochemistry is the study of chemical reactions taking place at the interface of an electrode and species in solution and which are driven by the application of an external voltage. A more detailed explanation is given step by step in this section.

### 1.1.1 Electrochemical Experimental Set-up

A standard three-electrode electrochemical cell is one of the most popular experimental set-ups employed for electrochemical studies. It consists of (i) a working electrode, (ii) a reference electrode and (iii) a counter electrode immersed in a solution of interest. An electrochemical cell may be placed in a faraday cage to minimise electromagnetic noise interferences, facilitating lower detection limits. All three electrodes are electrically connected to a potentiostat which allows for the control of the applied potential and the measurement of the current generated by electrochemical reactions occurring at the interface between the working electrode and the solution. All potentials are controlled and reported with respect to the reference electrode. The measured current passes between the working electrode and the counter electrode through the solution. The potentiostat is connected to a computer to acquire data. A standard three-electrode electrochemical experimental set-up is illustrated in Figure 1.2.

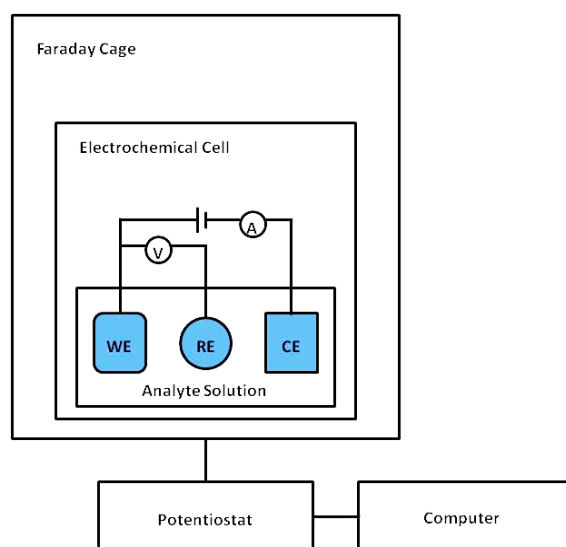


**Figure 1.1:** Schematic diagram of a standard three-electrode electrochemical cell within a Faraday cage, connected to a potentiostat and to a computer. WE, RE and CE are the working, the reference and the counter electrodes, respectively.

**(i) Working Electrode**

A wide range of materials have been used as working electrodes in electrochemical experiments. Some examples include gold, platinum and carbon, which are further discussed in section 1.2. It is crucial to obtain a reproducible and clean surface. Thus, a surface preparation protocol is necessary and depends on the electrode material.

**(ii) Reference Electrode**

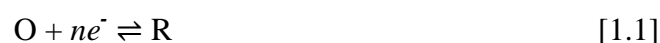
The reference electrode provides a stable and well-known potential, which should not vary when a potential is applied to the working electrode. It must also be chemically stable. No current should pass through the reference electrode or it should be negligible in order to prevent its polarisation and hence prevent a change of its potential. The most reliable reference electrode is the saturated calomel electrode; however its use is restricted because of its high toxicity arising from the presence of mercury. Another reliable reference electrode is the silver/silver chloride (Ag/AgCl) reference electrode. It is a very commonly used reference electrode as it is stable, non-toxic, inexpensive and easy to fabricate. It consists of an AgCl coated silver wire immersed in a sodium chloride or potassium chloride solution contained in a glass capillary. The electrode potential depends on the concentration of that solution, which can vary from 0.1 M to ~ 4.5 M (saturated); saturated solutions are often preferred as the electrode would remain stable longer than with diluted solutions, i.e., water evaporation will not affect the saturated solutions but will affect the concentration of dilute solutions. A permeable frit seals the bottom end of the Ag/AgCl electrode to allow contact with the solution in the electrochemical cell. However, the rather large size of the Ag/AgCl electrode requires relatively high sample volume and limits its use with emerging miniaturised electrochemical devices. Consequently, alternative reference electrodes have been developed. One approach consists of integrating a silver electrode on a chip substrate and modifying it with a chloride salt to form an on-chip Ag/AgCl reference electrode<sup>1,2</sup>. While it provides a quasi-stable reference electrode, the silver electrode needs to be modified with AgCl after each measurement, which is time consuming and not always reliable. Another approach is to use silver as a reference electrode, but silver alone is not stable at all with potential shifts up to  $\pm 0.5$  V because it oxidises easily in water and in air<sup>3</sup>. A third option is to use a noble metal pseudo-reference electrode, e.g., platinum or gold<sup>4, 5</sup>. The term pseudo indicates that noble metal are stable only over a short period of time and calibration is required prior every measurement<sup>6</sup>.

### (iii) Counter Electrode

The counter electrode must be approximately ten times larger than the working electrode as it acts as a supply (or sink) of electrons for the working electrode, and hence should not limit the electrochemical reactions. This also prevents current flowing through the reference electrode, which would result in the electrode polarising with a consequent shift in potential. Moreover, both electrodes must be sufficiently separated to avoid any interference between the opposite redox processes occurring at the same time at the counter electrode and at the working electrode. This spatial separation of the oxidation and the reduction areas of the overall redox reaction is the essential feature of electrochemistry as it maintains electroneutrality in the solution.

### 1.1.2 Electron Transfer

Chemical reactions occurring at an electrode-solution interface by the application of a potential are commonly investigated phenomena in electrochemistry. These chemical reactions involve heterogeneous electron transfer processes, known as electrolysis, which produce positive or negative currents. As such, common electrochemical reactions include: a simple electron transfer from an electrode to an electroactive species in solution (or vice-versa)<sup>7</sup>, a change of the electrode surface, e.g., formation of an oxide layer or deposition of a metal<sup>8</sup>, or a change of physical state, e.g., from liquid to gas<sup>9, 10</sup>. In all cases, electrochemical reactions are invariably reduction (a gain of electron) or oxidation (a loss of electron) reactions, which are typically represented by the following equation:



where O is the oxidised form of a redox species in solution,  $n$  the number of electrons  $e^{-}$  transferred and R is the reduced form of the redox couple. By definition, the electrode where reduction reactions take place is known as cathode and the electrode where oxidation reactions occur is called anode.

In order for electron transfers to happen at the electrode-solution interface, the energy level of an electron must correspond to the energy level of the molecular orbital of the acceptor or of the donor. This energy level is known as the activation energy and depends on the applied potential. Under a voltage bias, when the applied potential  $E$  is

lower than the formal potential of a redox couple  $E^{0'}$ , the energy of electrons at an electrode surface must reach a sufficiently high level to be transferred to the lowest unoccupied molecular orbital (LUMO) of a molecule in solution, thereby forming a reduction current. By contrast, when the electrode potential is higher than the formal potential of a redox couple, the electrode energy decreases such that it reaches a sufficiently low level for electron(s) to transfer from the highest occupied molecular orbital (HOMO) to the electrode, thereby forming an oxidation current. The changes of the electronic states at the electrode-solution interface during reduction and oxidation processes are shown in Figure 1.1.

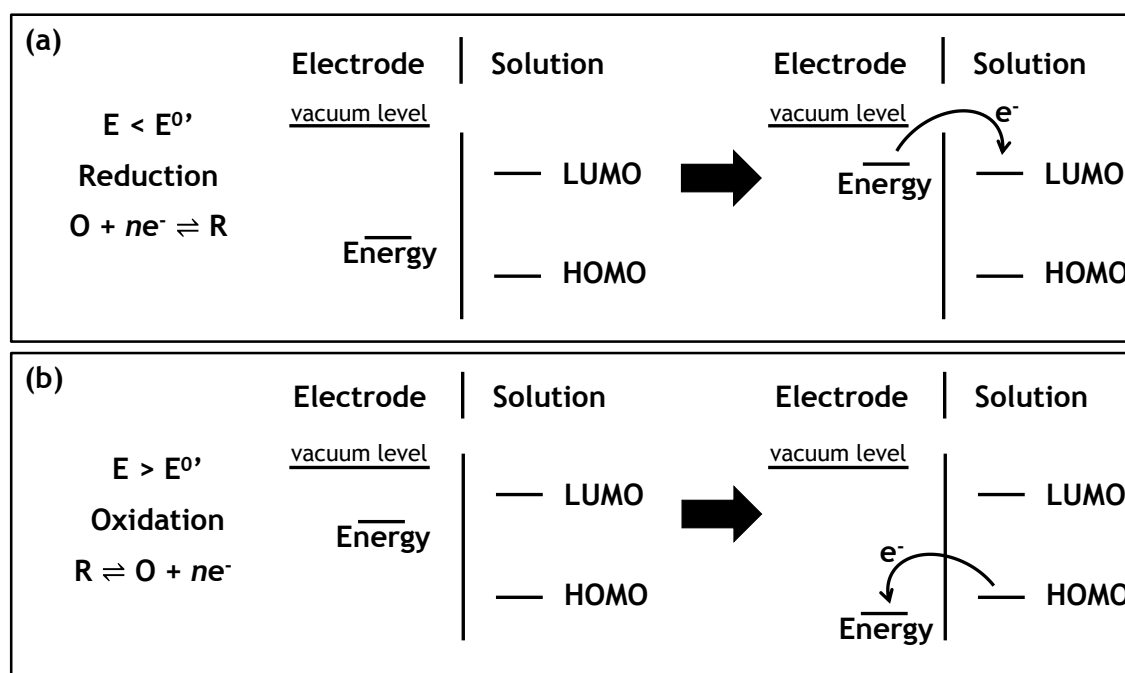


**Figure 1.2:** Diagram of the electron transfer and energy levels at an electrode-solution interface for (a) reduction and (b) oxidation processes.  $E$  is the applied potential and  $E^{0'}$  is the formal potential of a redox couple. LUMO is the lowest unoccupied molecular orbital and HOMO is the highest occupied molecular orbital.

### 1.1.3 Faradaic and Non-faradaic Currents

In electrochemical experiments, charge transfers involved at the interface between the working electrode and the electrolyte solution obey Faraday's law<sup>11</sup>:

$$Q = nNF \quad [1.2]$$

where  $Q$  is the charge (C),  $n$  is the number of electron involved in the reaction,  $N$  is the number of moles (mol) of analyte and  $F$  is Faraday's constant ( $96485 \text{ C}\cdot\text{mol}^{-1}$ ). These processes generate faradaic current, which is of great interest in electrochemistry. However, the currents observed at a working electrode may not only arise from charge

transfers but in fact may also arise from adsorption and desorption processes that can take place at the electrode surface. The contributions of the latter to the measured current do not follow Faraday's law and hence are known as non-faradaic current.

Consider an electrochemical cell where only non-faradaic current is measured. In this regard, when a potential is applied, an electric field develops, which causes charges to accumulate at the electrode-solution interface according to<sup>12</sup>:

$$\frac{Q}{E} = C \quad [1.3]$$

where  $Q$  is the charge stored at the electrode-solution interface (C),  $E$  is the potential across at the electrode-solution interface (V) and  $C$  is the capacitance (F). The electrode-solution interface can be viewed as a capacitor. In other words, the application of a potential results in the formation of a specific interfacial region, known as the double layer. Its capacitance and structure depend on several parameters such as: electrode material, solvent, supporting electrolyte concentration, extent of specific adsorption of ions and molecules, and temperature.

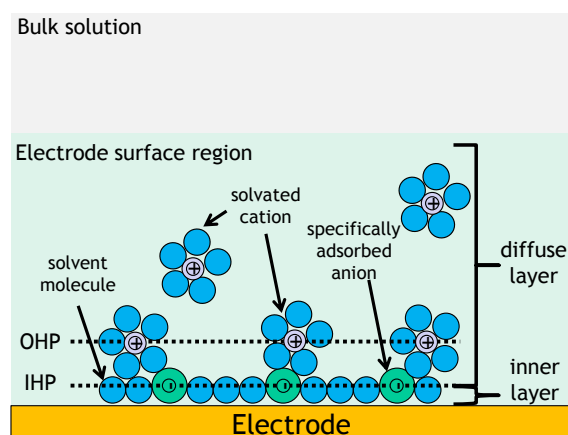


**Figure 1.3:** Simplified model of the double-layer region with specifically adsorbed anions and solvent molecules in the inner layer, and solvated cations in the diffuse layer. IHP and OHP are the inner and outer Helmholtz planes, respectively.

Although detailed description of double-layer models can be found in the literature, e.g., the Helmholtz<sup>13, 14</sup>, the Gouy and Chapman<sup>15, 16</sup>, and the Stern<sup>16</sup> models, there is no general model describing the double-layer. Nevertheless, the most commonly used model is the combination of the Helmholtz and Gouy-Chapman models, which was suggested by Stern<sup>12</sup>. This classic, simplified model of the double layer formed at a metal electrode surface in solution considers two planes defining two layers, see Figure 1.3. The first one, known as the inner Helmholtz plane (IHP), passes through the

centres of specifically adsorbed species. The layer between the electrode surface and the IHP is the inner layer, where solvent molecules and ions are specifically adsorbed onto the electrode surface via chemical interactions. The second one, called the outer Helmholtz plane (OHP), passes through the centres of non-specifically adsorbed solvated counter ions, which are attracted to the positively (or negatively) charged electrode surface via the Coulomb force. Between the OHP and the bulk solution, non-specifically adsorbed species spread in an outer diffuse layer, which thickness depends on the total ionic concentration of the solution. The presence of the double layer is responsible for non-faradaic charging currents, also known as capacitive currents, i.e., not related to any oxidation or reduction reactions. While in most cases capacitive currents are negligible, it can sometimes be a hindrance for monitoring faradaic processes, e.g., at low concentration levels or at fast scan rates. Consequently, different ways are used in electrochemistry to suppress or minimise capacitance.

#### 1.1.4 Factors Affecting the Faradaic Response

As described in section 1.1.2, typical electrochemical reactions involve electron transfer between an electrode and redox species in solution resulting in a current flow. This faradaic current can be controlled by a number of factors, which are principally the rate of charge transfer occurring in the interfacial region (electron kinetics) and the transport of material from the bulk solution to the electrode-solution interface (mass transport). The slowest process between electron kinetics and mass transport dominates the overall reaction rate. The electron kinetics and mass transfer pathways that can be involved in a redox reaction at the electrode surface are shown in figure 1.4.

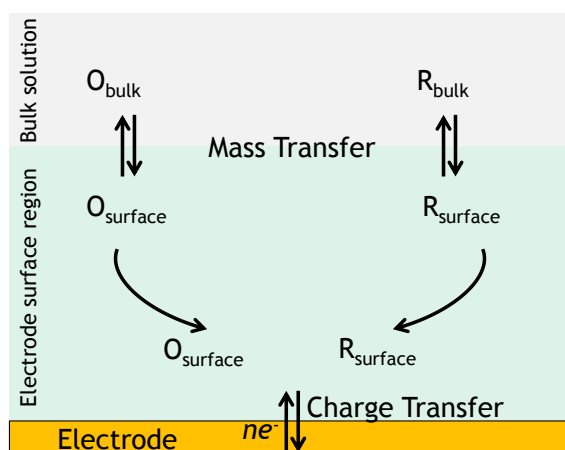


**Figure 1.4:** The electron kinetics and mass transfer pathways that can be involved in a redox reaction at the electrode surface

**(i) Kinetics of One-Step, One-Electron Transfer Process**

For an accurate electrode kinetic theory, the electrode potential should fulfil two requirements<sup>12</sup>. First it should follow the Nernst equation, which links the electrode potential to the bulk concentrations of redox species in solution at equilibrium:

$$E_{eq} = E^{0'} + \frac{RT}{nF} \ln \frac{C_O^*}{C_R^*} \quad [1.4]$$

where  $E_{eq}$  and  $E^{0'}$  are the equilibrium and formal redox potentials (V) of a redox couple,  $R$  is the gas constant ( $8.314 \text{ J.mol}^{-1}.\text{K}^{-1}$ ),  $T$  is temperature (K),  $n$  is the number of electron involved in the reaction,  $F$  is Faraday's constant ( $96485 \text{ C.mol}^{-1}$ ),  $C_O^*$  and  $C_R^*$  respectively are the bulk concentrations ( $\text{mol.cm}^{-3}$ ) of the oxidised and reduced forms (i.e., O and R) of a redox couple. The second requirement for a valid electrode kinetic model is that it should also fulfil the Tafel equation:

$$E - E_{eq} = a + b \log i \quad [1.5]$$

where  $E$  is the applied potential (V),  $a$  and  $b$  are constants (V) and  $i$  is the faradaic current (A).

In this regard, charge transfer kinetics can be treated as a complex multistep process involving  $n$  electrons (see equation 1.1), with one electron transfer taking place in each step since statistically it is highly unlikely that more than one electron will be transferred at a time. By contrast, charge transfer kinetics can be viewed as a simple one-step process involving only one electron. All theoretical kinetic studies presented in this work are based on the Butler-Volmer model for one-step, one-electron transfer processes<sup>12</sup>. The corresponding version for multistep electron transfer processes are not discussed here but can be found in a variety of publications. Other developed models applying for single and multi-step electron transfer mechanisms can be found in the literature, e.g., the Marcus-Hush theory<sup>17</sup>.

*1<sup>st</sup> Requirement: Nernst Equation*

Within the scope of this thesis, a one-step, one-electron transfer process taking place at an electrode-solution interface is considered<sup>12</sup>:



where O is the oxidised form of a redox species in solution,  $e^-$  is the electron transferred, R is the reduced form of the redox couple,  $k_{red}$  and  $k_{ox}$  are the heterogeneous

rate constants for the reduction and for the oxidation ( $\text{cm}\cdot\text{s}^{-1}$ ), respectively. The forward component corresponds to a reduction, which rate is proportional to the surface concentration of species O at time  $t$ :

$$V_{red} = k_{red} C_O(0, t) \quad [1.7]$$

where  $V_{red}$  is the reduction rate ( $\text{mol}\cdot\text{cm}^{-2}\cdot\text{s}^{-1}$ ) and  $C_O(0, t)$  is the surface concentration ( $\text{mol}\cdot\text{cm}^{-3}$ ) of species O at time  $t$  (s). Furthermore, the cathodic current is proportional to the reduction rate:

$$V_{red} = \frac{i_{red}}{FA} \quad [1.8]$$

where  $i_{red}$  is the cathodic current (A),  $F$  is Faraday's constant ( $96485 \text{ C}\cdot\text{mol}^{-1}$ ) and  $A$  is the electrode surface ( $\text{m}^2$ ). Hence, by combining equations 1.7 and 1.8, the cathodic current can be obtained as follows:

$$i_{red} = F A k_{red} C_O(0, t) \quad [1.9]$$

The reverse component represents an oxidation. Likewise, its rate  $V_{ox}$  and the oxidative current  $i_{ox}$  may be expressed as follows:

$$V_{ox} = k_{ox} C_R(0, t) \quad [1.10]$$

$$V_{ox} = \frac{i_{ox}}{FA} \quad [1.11]$$

$$i_{ox} = F A k_{ox} C_R(0, t) \quad [1.12]$$

where  $C_R(0, t)$  is the surface concentration ( $\text{mol}\cdot\text{cm}^{-3}$ ) of species R at time  $t$  (s). Thus the net reaction current,  $i$ , defined as the difference between the cathodic current and the anodic current, corresponds to:

$$i = F A [k_{red} C_O(0, t) - k_{ox} C_R(0, t)] \quad [1.13]$$

In order for an electron transfer to occur between the electrode and species (O or R) in solution and hence produce a current flow, the energy level of the electron must overcome the activation energy barrier, i.e., the minimum energy level allowing an electron transfer. This is achieved by applying a potential. Detailed descriptions of the involved mechanisms and their associated equations can be found in the literature<sup>12</sup>. In brief, the dependence of heterogeneous rate constants on the applied potential is explained. As a result, these constants for the reduction and for the oxidation can then respectively be defined as:

$$k_{red} = k^0 e^{-\alpha F(E-E^0)/RT} \quad [1.14]$$

$$k_{ox} = k^0 e^{(1-\alpha)F(E-E^0)/RT} \quad [1.15]$$

where  $k^0$  is the standard heterogeneous rate constant ( $\text{cm}\cdot\text{s}^{-1}$ ) and  $\alpha$  is the charge transfer coefficient; other variables have previously been defined. Equations 1.14 and 1.15 show that the rate at which electrons are transferred between the electrode surface and redox species in the interfacial region is influenced by the relative values of the applied potential and the standard redox potential. Consequently, the rate of electrolysis can be changed simply by varying the applied voltage, and  $k^0$  gives a relatively straightforward interpretation of the kinetic facility of a redox couple. Generally, large  $k^0$  values ( $> 0.02 \text{ cm}\cdot\text{s}^{-1}$ ) indicate that, following the application of a potential, the electron transfer occurs rapidly as such that equilibrium between redox species O and R will be re-established quickly; the reaction is called reversible<sup>12</sup>. However, small  $k^0$  values ( $< 5.0 \times 10^{-5} \text{ cm}\cdot\text{s}^{-1}$ ) are usually typical of slow electron transfer and hence require longer time to reach equilibrium; the system is known as irreversible<sup>12</sup>. Intermediate rates ( $5.0 \times 10^{-5} \text{ cm}\cdot\text{s}^{-1} < k^0 < 0.02 \text{ cm}\cdot\text{s}^{-1}$ ) are defined as quasi-reversible regime<sup>12</sup>.  $\alpha$  is a measure of the symmetry between the forward and reverse electron transfer steps, with a value between 0 and 1. In most systems,  $\alpha$  turns out to lie between 0.3 and 0.7, e.g., for metal electrodes  $\alpha$  is typically close to 0.5<sup>18</sup>.

Substitution of equations 1.14 and 1.15 into equation 1.13 gives the Butler–Volmer equation of electrode kinetics:

$$i = F A k^0 [C_O(0, t) e^{-\alpha F(E - E^{0'})/RT} - C_R(0, t) e^{(1-\alpha)F(E - E^{0'})/RT}] \quad [1.16]$$

Under equilibrium conditions ( $E = E_{eq}$ ), the reductive and oxidative currents are equal in magnitude but have opposite signs; hence the net current is zero, meaning that:

$$F A k^0 C_O(0, t) e^{-\alpha F(E_{eq} - E^{0'})/RT} = F A k^0 C_R(0, t) e^{(1-\alpha)F(E_{eq} - E^{0'})/RT} \quad [1.17]$$

Since equilibrium applies, the concentrations of O and R at the surface are equal to their value in the bulk ( $C_O^*$  and  $C_R^*$ , respectively), thus by rearranging equation 1.17, we obtain:

$$e^{F(E_{eq} - E^{0'})/RT} = \frac{C_O^*}{C_R^*} \quad [1.18]$$

Equation 1.18 is simply an exponential form of the Nernstian relation (equation 1.4); note that  $n$  does not appear as  $n = 1$ . Consequently, the Butler-Volmer theory fulfils the first requirement for a successful kinetic theory.

2<sup>nd</sup> Requirement: Tafel Equation

Furthermore, even though at equilibrium the net current is zero, faradaic activity is still in progress such that the magnitudes of reduction and oxidation currents are equal. This is known as the exchange current,  $i_0$ , which may be written as:

$$i_0 = F A k^0 C_O^* e^{-\alpha F(E_{eq} - E^{0'})/RT} \quad [1.19]$$

By raising both sides of equation 1.18 to the power of  $-\alpha$ , we get:

$$e^{-\alpha F(E_{eq} - E^{0'})/RT} = \left(\frac{C_O^*}{C_R^*}\right)^{-\alpha} \quad [1.20]$$

Therefore, the combination of equations 1.19 and 1.20, gives:

$$i_0 = F A k^0 C_O^{*(1-\alpha)} C_R^{*\alpha} \quad [1.21]$$

In the particular case where  $C_O^* = C_R^* = C$ , we have:

$$i_0 = F A k^0 C \quad [1.22]$$

In both cases, it is evident that the exchange current is directly proportional to the standard heterogeneous rate constant. Actually, the exchange current is often substituted for  $k^0$  in kinetic equations; the division of equation 1.16 by 1.21, yields:

$$\frac{i}{i_0} = \frac{C_O(0,t)}{C_O^*} e^{-\alpha F(E - E^{0'})/RT} \left(\frac{C_O^*}{C_R^*}\right)^\alpha - \frac{C_R(0,t)}{C_R^*} e^{(1-\alpha)F(E - E^{0'})/RT} \left(\frac{C_O^*}{C_R^*}\right)^{-(1-\alpha)} \quad [1.23]$$

An advantage of working with  $i_0$  rather than  $k^0$ , is that the current can be related to the overpotential ( $E - E_{eq}$ ) rather than the formal potential  $E^{0'}$ ; rearrangement of equation 1.23 by taking into account equations 1.18 and 1.20, gives:

$$i = i_0 \left[ \frac{C_O(0,t)}{C_O^*} e^{-\alpha F(E - E_{eq})/RT} - \frac{C_R(0,t)}{C_R^*} e^{(1-\alpha)F(E - E_{eq})/RT} \right] \quad [1.24]$$

This equation is known as the current-overpotential equation; the first term describes the cathodic current at any potential, and the second one represents the anodic contribution. When the surface concentrations are approximately equal to the bulk concentration (i.e., no mass transfer effects), equation 1.24 approximately becomes:

$$i = i_0 \left[ e^{-\alpha F(E - E_{eq})/RT} - e^{(1-\alpha)F(E - E_{eq})/RT} \right] \quad [1.25]$$

Equation 1.25 is a good approximation for a given redox process when reduction (or oxidation) contributes to 99% or more to the total current. For large positive overpotentials, the cathodic (reductive) component tends to zero; the net faradaic current becomes the same as the anodic current (oxidative). Large positive overpotentials can then be obtained from:

$$E - E_{eq} = -\frac{RT}{(1-\alpha)F} i_0 + \frac{RT}{(1-\alpha)F} \ln i \quad [1.26]$$

or

$$E - E_{eq} = -2.3 \frac{RT}{(1-\alpha)F} \log i_0 + 2.3 \frac{RT}{(1-\alpha)F} \log i \quad [1.27]$$

Similarly, for large negative overpotentials, the anodic component is negligible; the net faradaic current is essentially the cathodic current. Therefore, large negative overpotentials can then be expressed as:

$$E - E_{eq} = 2.3 \frac{RT}{\alpha F} \log i_0 - 2.3 \frac{RT}{\alpha F} \log i \quad [1.28]$$

Equations 1.27 and 1.28 are in the form of the Tafel equation (equation 1.5). In this manner, the Butler-Volmer model fulfils the other requirement for a valid electrode kinetic theory.

In conclusion, the Butler-Volmer model is an accurate electrode kinetic theory as it fulfils the two requirements, i.e., the Nernst equation and the Tafel equation. Therefore, for many electrochemical systems, experimental current of a one-step, one-electron mechanism can be well described using the simple Butler-Volmer kinetic model presented above. It allows for the determination of the standard heterogeneous rate constant, which depends on the relative values of the applied potential and the standard redox potential. However kinetics of the electron transfer is not the only factor which can control the overall redox reaction as discussed in the following section.

## (ii) Mass Transfer

As detailed previously, the faradaic current is affected by the electron transfer rate in the interfacial region and depends on the relative values of the applied potential and the standard redox potential. However, once the electrospecies at the electrode-solution interface have been reduced or oxidised, fresh redox molecules need to be transported from the bulk solution to the interfacial region in order to maintain the electrolysis. Consequently, the faradaic current also depends on the rate of mass transport between the bulk solution and the interfacial region. In fact, in many cases, the rate of mass transport is slower than the rate of electron transfer, and therefore it is often the case that the overall faradaic response is principally affected by the rate of mass transfer. Depending on its nature, mass transport can be divided into convection, migration and diffusion<sup>19, 20</sup>.

*Convection*

Convection is the random movement of molecules arising from natural or forced changes in the bulk solution. Natural convection, also known as free convection, is due to temperature differences, which affects the solution density. It is easily suppressed when working at constant temperature. Moreover, diffusion tends to eliminate the thermal gradient causing the movement of species. Forced convection occurs when the movement is induced by the application of external forces such as mechanical stirring, vibrations, pumping or fluid injection. Forced convection is non-existent in un-agitated solutions. Thus, the contribution of convection to the overall faradaic current is insignificant in static solutions at constant temperature.

*Migration*

Migration is the random movement of charged species under the influence of an electric field. In most electrochemical experiments, the contribution of migration to the overall faradaic current becomes negligible in presence of excess inert support electrolyte.

*Diffusion*

During electrochemical reactions, electroactive species at an electrode are consumed, creating depletion zones. As a result, redox molecules move randomly from regions of higher concentration (bulk solution), to regions of lower concentration (electrode-solution interface). In other words, diffusion is the random movement of molecules due to concentration gradients. This flux of species is defined as the number of moles passing through a certain position per unit time and area. Fick's first law shows that the flux of species (e.g., species O)  $J_{O,diffusion}$  is proportional to the concentration gradient  $\frac{\partial C_O(x)}{\partial x}$ , which for one-dimensional diffusion is expressed as:

$$J_{O,diffusion}(x) = -D_O \frac{\partial C_O(x)}{\partial x} \quad [1.29]$$

where  $D_O$  is the diffusion coefficient ( $\text{cm}^2 \cdot \text{s}^{-1}$ ) of species O. Generally this value can be found in the literature for a given pair of redox molecules. Alternatively, it can be determined experimentally using, e.g., cyclic voltammetry or double step voltammetry. For two or more dimensions, equation 1.29 is generalised as:

$$J_{O,diffusion}(x) = -D_O \nabla C_O(x) \quad [1.30]$$

Fick's second law predicts the change of the concentration of species over time, which for one-dimensional diffusion is given by:

$$\frac{\partial C_O(x,t)}{\partial t} = D_O \frac{\partial^2 C_O(x,t)}{\partial x^2} \quad [1.31]$$

For two or more dimensions, equation 1.31 becomes:

$$\frac{\partial C_O(x,t)}{\partial t} = D_O \nabla^2 C_O(x,t) \quad [1.32]$$

In the majority of electrochemical systems, the faradaic current is controlled by mass transport. Furthermore, diffusion is the most common form of mass transport as convection and migration are often negligible. Therefore, it is often the case that the faradaic current is governed by diffusional mass transport. As such, the current response for diffusion-only experiments depends on the flux at the electrode surface:

$$i = nFAJ_{O,diffusion}(x,t) \quad [1.33]$$

Equations 1.31 and 1.32 are crucial for the modelling of diffusional mass transport in electrochemical systems. The flux depends on the electrode material, size and geometry. This is further explained in Section 1.3.

### 1.1.5 Voltammetric Techniques to Study Electrode Reactions

Computer-controlled electrochemical instruments such as potentiostats provide voltammetric techniques to monitor the current generated by the application of a potential wave function to a working electrode for a range of redox species in solution. The current-potential curves obtained are known as voltammograms. The applied potential at which electronic processes occur provides qualitative information, whereas the current can be employed as a quantitative measure for specific redox molecules. A variety of techniques are available; they can be simple such as chronoamperometry and cyclic voltammetry where the current is recorded as a function of time, or more complicated such as square wave voltammetry and differential pulse voltammetry where a series of pulses are superimposed over a potential staircase and the current is sampled at specific time intervals to eliminate background current. The two voltammetric techniques widely employed in this work and described here are (i) cyclic voltammetry, and (ii) square wave voltammetry. Description of other techniques can be found in a range of publications<sup>12, 21</sup>.

#### (i) Cyclic Voltammetry

Cyclic voltammetry is one of the most widely used techniques to investigate an electrochemical system. The applied potential is swept linearly from an initial potential,

$E_{in}$ , to a final potential,  $E_{fin}$ , and reversed from that potential back to generally the initial one, see Figure 1.5. The linear sweep rate is known as scan rate and can vary from  $1 \text{ mV}\cdot\text{s}^{-1}$  up to thousands of  $\text{V}\cdot\text{s}^{-1}$ . The initial potential is set at a value where no redox reaction occurs and is swept negatively (or positively) past the standard potential of a redox couple,  $E^{o'}$ , i.e., towards the potential region where the electrochemical reaction of interest takes place. Depending on the redox species studied, the reduction reaction will occur on the forward scan and the oxidation reaction on the reversal scan, or vice-versa. The current is represented as a function of potential and peaks on both forward and backward scans need to be considered. The reversibility of the reaction can simply be verified by calculating the ratio between the cathodic and anodic peak currents; a result of 1 indicates a reversible reaction. Another important information is the difference between the forward and the reverse peak potentials  $\Delta E_p$  (V), which for a Nernstian reaction at  $25^\circ\text{C}$  should be equal to:

$$\Delta E_p = \frac{0.059}{n} \quad [1.34]$$

Other example of parameters that can be determined include estimation of the standard heterogeneous rate constant  $k_o$  and the diffusion coefficient of a redox couple  $D_i$ . These will be further explained throughout the thesis. The shape of the curve also gives information about the rate determining factor. Peak-shaped voltammograms arise from the fact that as potential moves past  $E^{o'}$ , surface concentration drops nearly to zero and mass transport to the surface reaches a maximum rate and then declines as the depletion effect sets in. By contrast, steady-state voltammograms are of particular interest as they require the rate of charge transfer at the electrode surface and the rate of mass transport to the electrode surface to be identical. During cyclic voltammetry measurements, the recorded current actually comprises both faradaic and charging currents. To extract faradaic information from the measured current response, perturbation caused by capacitance can be subtracted.

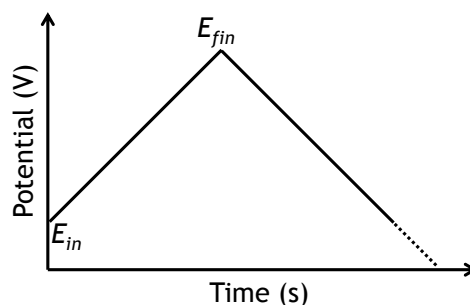


**Figure 1.5:** Schematic diagram of the potential wave form in cyclic voltammetry. The potential is swept from a potential  $E_{in}$  to a potential  $E_{fin}$ , and reversed back to  $E_{in}$  or a different potential (dashed line).

**(ii) Square Wave Voltammetry**

Square wave voltammetry is a widely used voltammetric technique employed to maximise faradaic to charging current ratio. The potential wave form can be viewed as a staircase, starting from a potential  $E_{in}$ , where no redox reactions take place, passing through the formal potential  $E^{\circ}$  of a redox species, and ending at a potential  $E_{fin}$ , once either a reduction or an oxidation reaction occurred. It is swept in a series of cycles consisting of two symmetrical pulses, one forward and the other reverse, as depicted in Figure 1.6. Each pulse is characterised by a pulse height (or amplitude),  $\Delta E_h$  and a pulse width,  $t$ . Each cycle is characterised by a frequency  $f$  and at the start of each cycle the potential shifts by an incremental potential,  $\Delta E_i$ , such that cycles successively superimposed onto each other. The scan rate  $v$  is equal to:

$$v = f \Delta E_i \quad [1.35]$$

The current is sampled at the end of each potential change, i.e., at the end of the forward pulse and at the end of the reverse pulse, in order to minimise the contribution of charging current. The difference between the forward and reverse currents is plotted against the potential, which forms a peak. In fact, the forward pulse amplifies the rate of a reduction (or oxidation) reaction and the reverse pulse reverses the process taking place. Moreover, the diffusion layer is not renewed at the beginning of each measurement cycles; the initial condition for each cycle is the complex diffusion layer that has evolved from prior pulses. Therefore, the current reaches a maximum around  $E^{\circ}$  and then decrease because the cumulative effect of electrolysis through many cycles causes a depletion of species O (or R). Consequently, the obtained peak-shape curve corresponds to either a reduction, or an oxidation, depending on the species studied.

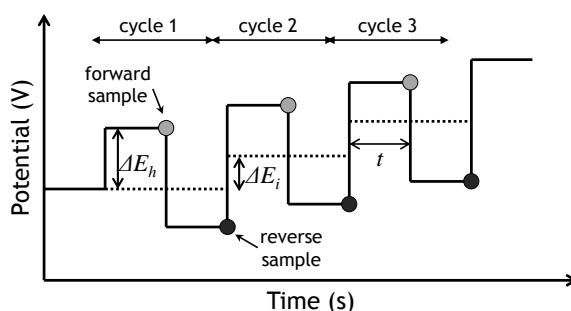


**Figure 1.6:** Schematic diagram of the potential wave form (bold lines) in square wave voltammetry. Each cycle comprises a forward pulse and a reverse pulse, which are characterised by a pulse height ( $\Delta E_h$ ), a pulse increment ( $\Delta E_i$ ) and a pulse width ( $t$ ). The dotted lines indicate where steps are superimposing one after another.

## 1.2 Electroanalysis at the Nanoscale

In recent years, research at the nanoscale has received increasing interest worldwide. Much of the interest is driven by the unique properties exhibited by nanoscale materials, which differ substantially from the properties of their bulk equivalent. Effectively, when compared to bulk materials, nanomaterials are often found to exhibit enhanced, e.g., electrical<sup>22</sup>, optical<sup>23, 24</sup>, chemical<sup>23, 25</sup> or thermal<sup>26</sup> properties. Consequently, due to their distinct and often enhanced properties, nanomaterials can provide many potential advantages over bulk materials when applied to sensing applications in areas including medicine<sup>27</sup>, electronics<sup>28</sup>, environment<sup>29</sup>, optics, biology<sup>27</sup> or physics<sup>30</sup>. By definition, sensors are devices that react to a physical, chemical or biological change in their local environment and convert that change into a measureable, quantifiable signal. Hence, nanosensors may enable the detection and quantification of many physical, chemical or biological phenomena occurring at the nanoscale, such as real-time measurement of a wide range of molecular interactions<sup>31, 32</sup>. To this end, in electrochemistry, currents generated by redox reactions taking place between an electrode and a species in solution are measured through a variety of different sensing techniques. As such, the electrode dimension is a crucial parameter to consider as enhanced electrochemical behaviour is expected with decreasing electrode dimension<sup>33</sup>. Nanoelectrodes and their advantages over micrometric electrodes are discussed in sections 1.2.1 and 1.2.2.

However, the exploration of the benefits arising from nanoscale electrodes has been restricted by the lack of practical and repeatable fabrication methodologies<sup>33</sup>. Nevertheless, a wide range of nanoelectrode types and material are discussed in the literature including carbon nanotubes<sup>34</sup>, gold nanoparticles<sup>35</sup>, copper nanobeads<sup>36</sup>, platinum nanowires<sup>37</sup> or germanium nanocrystals<sup>38</sup>. Within the scope of this thesis, particular emphasis is put on metal nanowires. In order to increase their potential use as functional elements in nanosensors, it is essential to efficiently synthesised reproducible, uniform, defect free and micrometric long nanowires. In this regard, developments in nanofabrication techniques, especially metal nanowires fabrication approaches, are discussed in section 1.2.3.

### 1.2.1 From Microelectrodes via Ultra-microelectrodes to Nanoelectrodes

Broadly speaking, microelectrodes are electrodes with a critical dimension on the order of 25  $\mu\text{m}$  or less, whereby critical dimension refers to the dimension which controls the electrochemical response<sup>33</sup>. Ultra-microelectrodes are electrodes presenting a small critical dimension on the order of tens of micrometres or less, down to submicrometer range. However, these rather broad descriptions are quiet misleading and since electrochemical reactions are interfacial reactions, mass transport is one of the key processes to consider for a more detailed definition. Effectively, compared to microelectrodes, ultra-microelectrodes display enhanced mass transport behaviour which stems from their small critical dimension. At microelectrodes, cyclic voltammograms are typically peak-shaped, especially for high scan rates, arising from the fact that mass transport occurs principally perpendicular to the electrode surface, i.e., planar diffusion. The peak currents are not geometry dependent and follow the Randles-Sevcik relationship<sup>12, 21</sup>:

$$i_p = (2.69 \times 10^5) n^{3/2} A D^{1/2} C^* \nu^{1/2} \quad [1.36]$$

where  $i_p$  is peak current (A),  $n$  is the number of electron transferred,  $A$  is electrode area ( $\text{cm}^2$ ),  $D$  is the diffusion coefficient ( $\text{cm}^2 \cdot \text{s}^{-1}$ ),  $C^*$  is bulk concentration of electroactive species, and  $\nu$  is scan rate ( $\text{V} \cdot \text{s}^{-1}$ ). By contrast, sigmoidal, quasi-steady-state or steady-state voltammograms can be achieved at ultramicroelectrodes, especially for low scan rates, as mass transport at ultra-microelectrodes takes on a hemispherical or hemicylindrical profile, i.e., radial diffusion, allowing enhanced mass transfer. In addition, limiting currents generated at ultra-microelectrodes are dependent on their geometry, which commonly are disc, band, hemispherical and spherical electrodes. Table 1.1 summarises these common ultra-microelectrode types showing their respective critical dimension and limiting current equation<sup>12</sup>.

Design	Dimension	Limiting current
Band 	l: length w: width	Quasi-steady state $i_l = \frac{nFC^*2\pi D}{\ln\left(\frac{64Dt}{w^2}\right)}$
Disk 	r: radius	Steady-state $i_l = 4nFDC^*r$
Hemisphere 		Steady-state $i_l = 2\pi nFDC^*r$
Sphere 		Steady-state $i_l = 4\pi nFDC^*r$

**Table 1.1:** Common ultra-microelectrode types and their associated limiting current.

Furthermore, the current densities at ultra-microelectrodes under conditions of radial diffusion are generally higher than that of microelectrodes in planar diffusion regime, thus ultra-microelectrodes are more sensitive. Note that variation in the experiment time scale also depends dramatically on the electrode critical size; the smaller the electrode size, the faster radial diffusion can be achieved. In other words, faradaic current can readily reach a time-independent limiting value under radial diffusion (see equations in table 1.1), which contrasts with the peak-shaped time-dependent faradaic current response for planar diffusion conditions (i.e., dependence on  $v^{1/2}$ , see equation 1.36). Other advantages of ultra-microelectrodes over other electrodes of micrometric dimensions include: lower background charging current and hence higher signal-to-noise ratio, the faradaic current can attain a time-independent limiting value at low to medium scan rates, enabling faster electroanalysis and improved kinetic measurement of electrochemical processes, lower detection limits, smaller ohmic drops of potential, lower solution resistance and can be used in small sample volumes.

These advantages make electrode miniaturisation an extremely valuable approach to electroanalysis as smaller electrode dimensions permit fabrication at higher densities enabling much greater-information gathering capability per device. However, single ultra-microelectrodes may exhibit faradaic currents that are too small or too difficult to measure. Therefore, arrays of these ultra-micro structures are required to obtain reasonable measurable currents; interactions between the individual electrodes within an array may for example permit regeneration of the electroactive species through redox cycling which amplifies the signal and make it easier to measure. But, limitations arise from the fact that ultra-microelectrodes within an array need to be sufficiently separated in order to avoid the whole array behaving like a larger electrode (microelectrode), and also not too space apart in order to prevent inefficient use of space<sup>19</sup>. An alternative option to improve electrodes electrochemical signal is to further reduce the critical dimension of electrodes, down to the nanoscale.

### 1.2.2 Nanoelectrodes

Nanoelectrodes are broadly defined as structures with a critical dimension in the range of 1 to 100 nm. However, a more precise definition takes into account the mass transport behaviour. As mentioned in the previous section, the mass-transport rate

increases as the electrode size decreases so that radial diffusion becomes dominant. That is why sigmoidal, quasi-steady-state or steady-state voltammograms can be readily achieved at ultra-microelectrodes. At nanoelectrodes, this can be observed to a much larger extent as radial diffusion can be achieved at even higher scan rates, which considerably lowers the electroanalysis time scale. Therefore compared to ultra-microelectrodes, nanoelectrodes exhibit significantly enhanced mass transport behaviour which results from their extremely small critical dimension. Consequently, the benefits which arise from ultra-microelectrodes can be expected to be at a greater extent at nanoelectrodes including: much higher current density and hence much higher sensitivity, the faradaic current can attain a relatively large time-independent limiting value even at high scan rates, much lower background current and hence much higher signal-to-noise ratio, enabling much faster electroanalysis and further improved kinetic measurement of electrochemical processes, much lower detection limits, negligible ohmic drops of potential, negligible solution resistance and can be used in significantly reduced sample volumes. Nanoelectrodes limiting currents are dependent on their geometry, which can be approximated using the equations in table 1.1 for disc, band, hemispherical and spherical electrodes.

Nanoelectrodes classification derives from the degree of quantum confinement within the structure, i.e., how many dimensions an electron is free to move within the structure. The basic classes of nanomaterials are as follows: two-dimensional (2D) structures, where an electron may move in two directions, e.g., thin films, one-dimensional (1D) nanostructure where an electron may only move in one direction, e.g., nanowires or nanotubes, and zero-dimensional (0D) nanostructures where an electron is completely confined, e.g., nanoparticles or quantum dots. Among these, the 1D-nanoelectrodes are highly desirable, as their geometric shape and high surface area impart high functionality.

### **1.2.3 Electrode Fabrication**

Description of microelectrodes and ultra-microelectrodes fabrication methods can be widely found in the literature<sup>33, 39, 40</sup>. For instance, electrodes can be fabricated by evaporating thin metal films onto glass substrates followed by deposition of an insulating layer on top for electrical isolation so that only film edges are exposed<sup>41</sup>,

sequential etching of microwire to a fine cone followed by insulation of all but the cone tip<sup>42-44</sup>, fabrication of disc electrodes by deposition of carbon in a capillary tube<sup>45, 46</sup>, and pulling of glass capillaries containing sealed microwires<sup>47</sup>. These techniques have made fabrication and integration of robust micro and ultra-micro structures achievable.

Consequently, advances in micro and ultra-micro fabrication techniques have led to tremendous research undertaken worldwide at the micro and ultra-micro scales. Furthermore, development of micro and ultra-micro fabrication techniques enabled the emergence of nanofabrication techniques, thereby increasing the interest of research at the nanoscale. Some nanoelectrodes fabrication approaches based on micro/ultra-micro techniques include: micropipette pulling technology<sup>48</sup>, partial insulation of an electrochemically sharpened metal wire or carbon fibre in photoresist<sup>49</sup>, Teflon®<sup>50</sup>, or glass<sup>43</sup>. Other innovative examples include: template-directed synthesis of deposited metals into sub-micron pores of home-made or commercial porous membranes<sup>51, 52</sup>, self-assembly of metallic nanoparticles<sup>53</sup>, nanowires or carbon microspheres decorated with nanoparticles at macroelectrodes<sup>54, 55</sup>. As a result, a wide variety of nanoelectrodes types are reported in the literature including: nanoband<sup>40</sup>, nanopore<sup>56</sup>, nanodisc<sup>57</sup>, nanowire<sup>58</sup>, nanoparticle<sup>59</sup>, nanocavity<sup>60</sup>, nanotube<sup>61</sup>; all either single or in array. Three key electrode materials employed are platinum, gold and carbon. Alternative materials such as conductive polymers and nanostructured inorganic materials have also been exploited as nanoelectrodes<sup>62, 63</sup>.

Although nanoelectrodes have been successfully fabricated in order to probe nanoscale electrochemical processes, major disadvantages associated with these electrodes arise such as the difficulty and length of time for fabrication, leaking of electrolyte through the seals, and the extremely small currents (10-100 pA) that may be achieved with them. Such small currents pose problems when the measured current is to be used as the analytical signal in an electroanalytical application. To this end, parallel nanoelectrode ensembles have been fabricated to allow high measurable currents (nA- $\mu$ A). For instance sparse arrays of vertically orientated multi-walled carbon nanotubes (MWCNTs) yielding  $\mu$ A currents have been synthesised by pressure enhanced vapour deposition techniques, encapsulated in a SiO<sub>2</sub> matrix and mechanically polished to expose the tips of the MWCNTs; these electrodes were used as biosensors<sup>64, 65</sup>.

The use of nanoelectrode arrays as a new generation of electroanalytical sensors has become very popular, particularly due to facile fabrication associated with them. However, a key limitation with nanoelectrodes ensembles is that individual nanoelectrode elements may not be diffusionally independent, i.e., diffusion layers surrounding each electrode may overlap heavily, thus nanoensembles electrochemically may behave as high surface area microelectrode<sup>19</sup>. At such electrodes the measured current is diffusive, with broad peaks that can reduce the sensitivity of measurements, and consequently yield poor limits of detection. To address this limitation, nanoelectrode arrays have been fabricated whereby individual nanoelectrodes are sufficiently spaced to render them diffusionally independent from their closest neighbours. For example, Arrigan *et al*, demonstrated steady state currents obtained at platinum nanopore electrodes and their arrays fabricated by focussed ion beam milling and lithography<sup>66</sup>.

Despite enormous progress, the controllable fabrication of structurally well-defined nanoelectrodes that exhibit electrochemical enhancements such as high speed steady-state measurements, ideal for sensing, has been restricted by the lack of effective fabrication methodologies of robust nanoelectrodes that combine analyte radial diffusion profiles with high measurable currents (nA- $\mu$ A). One potential solution is to employ ultra-long ( $\mu$ m to cm) metal nanowires which maintain properties of radial diffusion. In order to increase the prevalence of nanowires as functional elements in nanosensors, two key barriers must be surmounted: firstly, it is crucial to efficiently synthesise ultra-long uniform and defect free nanowires, secondly, it is essential to control the nanowire location on a substrate to permit subsequent registration, alignment and electrical-contacting with interconnection metallisation. To this end, there is no widely accepted general technique for fabrication of ultra-long metal nanowires, but fabrication approaches that could possibly satisfy both of these requirements include: (i) metal electrodeposition in porous templates (bottom-up approach), (ii) electron-beam lithography (top-down approach) and (iii) lithographically patterned nanowire electrodeposition (bottom-up and top down approach). In bottom-up approaches, fabricated nanowires should subsequently be assembled onto technology relevant substrates based on chemical and physical forces including: fluidic, capillary, magnetic, or electrostatic forces. Other examples of metal nanowire fabrication by bottom-up approaches are: vapour-liquid-solid growth of a metal<sup>67</sup> and colloidal dispersion<sup>68</sup>,

solution phase synthesis<sup>69</sup>. By contrast, in top-down approaches, a bulk material is reduced to get nanoscale elements such as in photolithography. Nanoskiving<sup>70</sup> and mechanical printing or stamping or molding techniques<sup>71</sup> combine both bottom-up and top-down approaches.

### (i) Metal Electrodeposition in Porous Templates

In this technique, one (or several) metal is electrochemically deposited into a porous template with pore dimensions close to the desired final nanowire size. In this regard, an ideal membrane would be inert and contain high density of long uniform, vertical and highly ordered nanochannels. Thanks to their chemical stability and versatility, thereby allowing great diversity in the types of materials that may be electrodeposited, anodic aluminium oxides (AAO) templates are well-used membranes. These can be produced by anodisation of high purity aluminium foils (> 99.9%) in weakly acidic media. By controlling the anodisation parameters and conditions, such as applied potential, electrolyte concentration, temperature and anodisation duration, the AAO nanochannels diameter, depth, thickness and inter-pore distances can be tuned, which allows for a large range of custom templates to be fabricated. Alternatively, such membranes may be purchased, albeit with a limited range of pore sizes, from companies such as Whatman Ltd. Polycarbonate membranes are another example of home-made or commercially available templates.

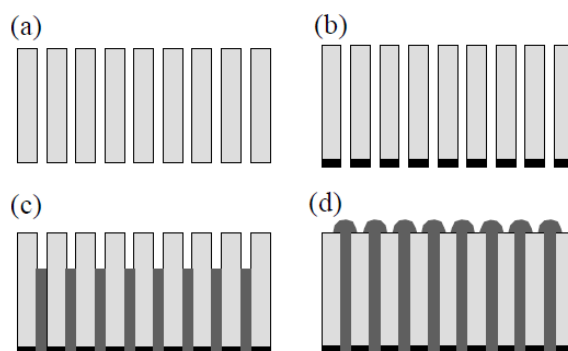


**Figure 1.7:** Electrodeposition of nanowires into a porous template. (a) a nanoporous membrane; (b) a seed layer of metal sputtered or evaporated onto one side of the membrane; (c) electrodeposition in progress - metal composition may be varied by appropriately changing the deposition solution; (d) completed nanowires still in template.

Figure 1.7 shows the steps of the metal electrodeposition templating process<sup>72</sup>. An initial metal layer is deposited by evaporation or sputtering onto one side of the membrane to form a conductive layer so that the membrane acts as a working electrode. The membrane is then placed in an appropriate solution and the metal of interest is

electrochemically deposited into the nanochannels. It is possible to obtain multi-layered nanowires by changing the deposition solution during the growth process. Following deposition, the membrane may be dissolved with an appropriate solvent, e.g., 3M sodium hydroxide solution, to liberate the nanowires.

Metal electrodeposition in porous templates is an attractive fabrication method of ultra-long nanowires because it provides high density of cylindrical nanowires with controlled diameter ranging from 10 up to 250 nm and length ranging from 5 to about 60  $\mu\text{m}$  depending on the membrane pore size and thickness, and is applicable to a large number of material systems, including noble metals, ferromagnetic materials, semimetals, etc. Although electrodeposited nanowires have been used for the detection of some molecules, their subsequent integration can be quite challenging.

## (ii) Electron Beam Lithography

One of the most flexible and widely used techniques for producing ultra-long metal nanowires is electron beam lithography. In this top-down technique, an electron sensitive resist (e.g., Polymethylmethacrylate) is applied on a substrate (e.g., silicon, quartz, fused silica), and a focused beam of high energy (typically  $> 30 \text{ kV}$ ) electrons is scanned in a programmed patterned fashion across the surface. When the electron beam hits the resist, it locally ionises atoms by breaking down chemical bonds and producing a cloud of secondary electrons. The resist is then developed by wet etching so that the desired pattern is revealed; in positive resists, exposed material is removed, while in negative resists, local cross-linking occurs as such that unexposed resist is removed. The resulting patterned resist layer serves as a stencil for metal deposition via evaporation or sputtering. Finally, following metallisation, the resist stencil and excess material on top of it are removed by a lift-off procedure, leaving fabricated metal structures on the surface.

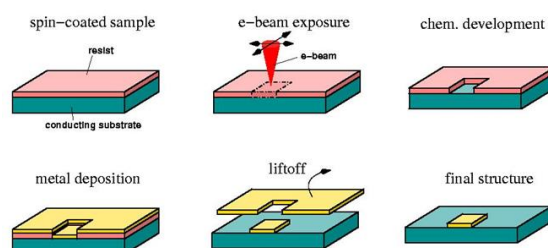


**Figure 1.8:** Process flow diagram for the formation of nanostructures using electron-beam lithography with a positive resist. Source: [nanooptics.uni-graz.at/ol/work/m\\_ebl.html](http://nanooptics.uni-graz.at/ol/work/m_ebl.html)

Figure 1.8 depicts the different electron beam and lift-off fabrication steps. The adhesion properties of the metal on the substrate are crucial to forming uniform and continuous metal structures. For example, titanium or nickel are commonly used as an adhesion layer for gold or platinum deposition on a variety of substrates.

Electron-beam lithography is capable of extremely high resolution (sub-10 nm) and allows for routine fabrication and integration of infinite structural configurations with highly reproducible dimensions. The key drawback of this technique is primarily its cost. While this technique is relatively expensive, its cost can be reduced so that it is competitive with other micrometric or nanoscale electrodes. Effectively, electron-beam lithography is a serial technique where several wafer can be processed at once, such that each nanostructure costs the same and the more the number of substrates processed at once, the lower this cost. In addition, electron-beam lithography masks are software based and can be easily modified to develop electrodes of different widths, shapes and types, for example electrode patterns can be altered to fabricate nanowire arrays or interdigitated fingers and maintain their compatibility with a single optical interconnection mask.

### **(iii) Lithographically Patterned Nanowire Electrodeposition**

Lithographically patterned nanowire electrodeposition is a relatively new and versatile technique for fabricating micrometric long metal nanowires using electrodeposition, combining a top-down and bottom-up approach through 7 different steps. An initial 5-100 nm thick metal layer, usually silver or nickel, is deposited onto, e.g., glass or oxidised silicon, by thermal vapour deposition (Step 1); the thickness of this film determines the nanowires height. This is followed by a spin-coated layer of photoresist (Step 2), which is then selectively patterned using a mask (Step 3). Following photoresist development, the exposed silver or nickel is removed by wet etching (Step 4). In Step 5, the trenched surface is immersed in a dilute metal plating solution which allows for the electrodeposition of a metal; the electrodeposition time depends on the metal and the desired nanowire width. The photoresist layer is removed by washing with acetone (Step 6). Finally, the patterned nickel or silver layer is removed using a second etch in the same solution as used in Step 4 (Step 7), leaving metal nanowire electrodes remaining on the glass substrate. The seven-step process flow for the

lithographically patterned nanowire electrodeposition method is shown in Figure 1.9 (a). A gold nanowire fabricated by this method is shown in Figure 1.9 (b).

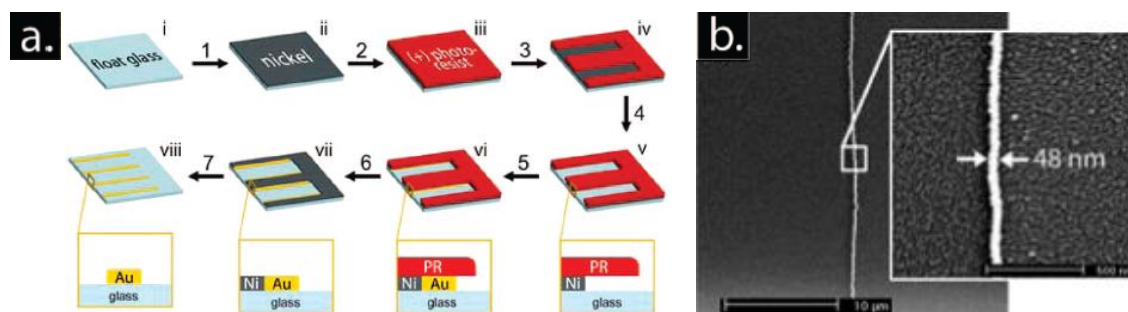


**Figure 1.9:** (a) Process flow diagram for the formation of gold nanowires using the seven-step lithographically patterned nanowire electrodeposition method<sup>73</sup>. (b) Low and high magnification SEM images of a single gold nanowire prepared by lithographically patterned nanowire electrodeposition<sup>73</sup>.

The fabricated nanowires have a rectangular cross-section shape with more or less controlled dimensions, which depending on the metal, solution composition, applied potential and electrodeposition time, typically vary as follows: 10 nm to hundreds of nanometres in width, 5 to 100 nm in height and 100  $\mu\text{m}$  to 1cm or more in length. However, these nanowires have a relatively low degree of reproducibility and are not uniform; imperfections arise from contamination during the fabrication process. Nevertheless, the lithographically patterned nanowire electrodeposition method permits nanowire registration, alignment and electrical-contacting with interconnection metallisation, making it a potential nanowire fabrication route for electrochemical-based applications. Some electrochemical characterisation of nanowires fabricated by the lithographically patterned nanowire electrodeposition has already been demonstrated in the literature by Penner *et al* and other groups have utilised this platform for direct electrochemical detection of dopamine<sup>73</sup>.

Thus, advances in nanofabrication approaches have hastened the development of functional nanosensing devices that demonstrate improved performances when compared to traditional larger devices. As a result, nanomaterials may be fabricated at the same length scales where many physical phenomena under test occur, e.g., of a similar size to the molecules of interest. A second key advantage of employing extremely small sized sensors is that it enables the fabrication of further miniaturised, ultra-sensitive, robust, reliable, low cost, easy to use devices for sensing applications.

## 1.3 Mass Transport Simulation Overview

Simulation of redox analyte concentration profiles is an essential tool to study and predict mass transport behaviour at an electrode-solution interface under the application of an external potential. It can be used at the design stage of electrodes or to give important insights of experimental results. As such, diffusional mass transport from the bulk solution to an electrode is mathematically described by Fick's second law, see equations 1.31 and 1.32. These are partial differential equations, i.e., equations that relate the change of an unknown function depending one or multiple variable(s). Here, the unknown is the concentration change with respect to time and position (i.e., distance from the electrode surface). Partial differential equations can be solved either by hand or by a relevant computer model using a numerical technique known as the finite element method. COMSOL Multiphysics® is a well-used versatile commercial software package for the solution of partial differential equations. In this regard, a succinct overview of the finite element method is given here, followed by general features of COMSOL Multiphysics® and important aspects of for the simulation of mass transport at an electrode-solution interface under the application of an external potential.

### 1.3.1 Finite Element Method

The finite element method is a numerical technique for approximate, yet reliable, solving of partial differential equations. It consists of defining the domain on which to solve the problem and dividing it into much smaller subdomains, called finite elements; the vertex of such elements are nodes and their ensemble is called a mesh.

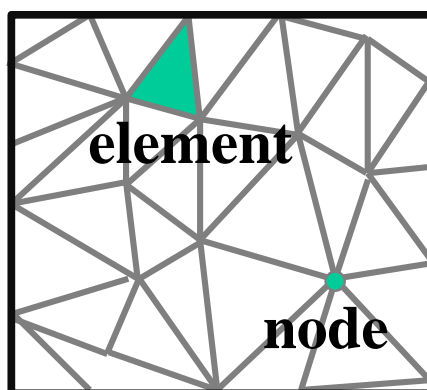


**Figure 1.10:** Schematic representation of a typical triangular mesh used in a two-dimensional domain.

Partial differential equations solutions are computed at nodes; solutions are interpolated, i.e., estimated using basis functions, whereby any point is described according to the number of parameters of the system that may vary independently (finite elements or degree of freedom). The finite elements geometry depends on that of the domain. Generally, in one-dimensional representation of the problem, finite elements are lines; in a two-dimensional situation they are triangles; and in a three dimensions they are tetrahedrons. In Figure 1.10, a schematic representation of a typical triangular mesh used in a two-dimensional problem representation is shown.

### **1.3.2 COMSOL Multiphysics<sup>®</sup>**

COMSOL Multiphysics<sup>®</sup> is one of the most widely used software package for the simulation of many real physical phenomena. It is a flexible and user-friendly modelling software for the solution of any physical process described with partial differential equations and thus is based on the finite element method. Figure 1.11 comprises screen-shot captures of COMSOL Multiphysics<sup>®</sup> software interface to summarise all the different steps for the building and then solving of a model. To start, the space domain dimension, the physical module and the study type need to be selected. Then, global and local parameters, variables and/or functions need to be entered. The next step consists of drawing the domain on which to solve the problem using various graphical tools, or for complicated geometries a CAD file can be imported. Then in the module of interest, e.g., transport of diluted species, set the partial differential equation describing the phenomenon under study and assign boundary conditions accordingly. In most cases, partial differential equations are in-built in the software and can be chosen from a wide range of different modules. However, it is possible to define an equation which is not already incorporated in the software. Once the domain and the equation are defined, it is necessary to create the mesh. It is important to refine the mesh until a good convergence is achieved (error less than 2%). In this regard, smaller elements are found in regions where abrupt change is expected, whereas larger elements are defined in region experiencing little or no change. For example, for the simulation of analyte concentration at an electrode-solution interface under the application of an external potential, the elements need to be considerably small near the electrode surface, while can be larger in bulk region. Finally, the solver parameters need to be adjusted in the study section prior to launching

the model computation. Once the model is solved, there is a wide range of options to display post-processing solution in the results section, e.g., one-dimensional to three-dimensional or plots.

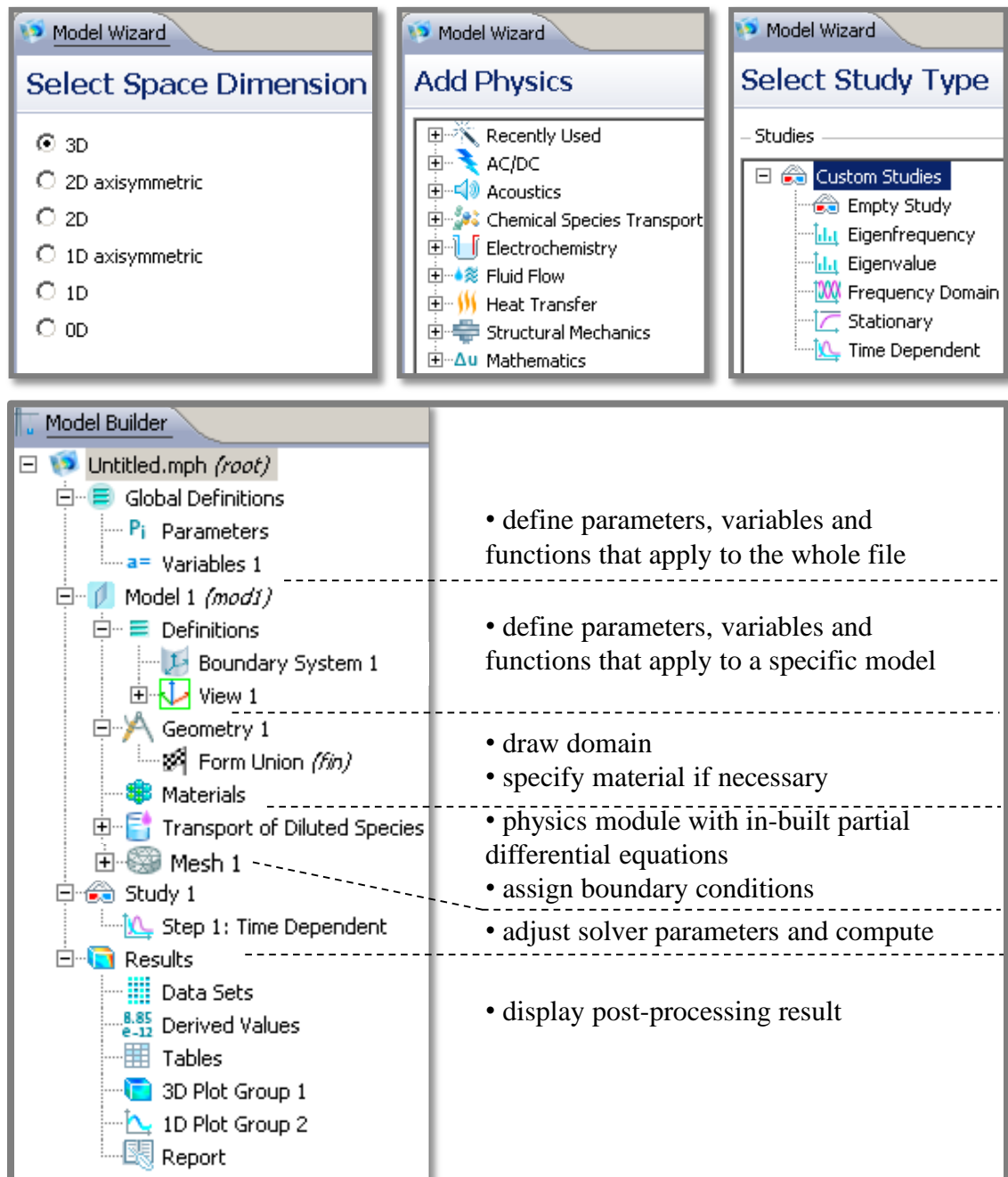


**Figure 1.11:** Screen-shot captures of COMSOL Multiphysics<sup>®</sup> 4.2 interface showing the different steps to build and solve a model.

### 1.3.3 Simulation of Mass Transport

Simulation of mass transport from the bulk solution to the electrode surface consists of solving the partial differential equations relating the change in concentration with

respect to time and position (i.e., Fick's second law)<sup>19, 20</sup>. At (i) single electrodes, simulations are principally used to provide important insight of analyte concentration profiles in conjunction with experimental results. However, at (ii) electrode arrays, simulations are primarily used to optimise electrode design prior to fabrication. To this end, (iii) the diffusion domain approach is used to represent electrodes. Here, only simulated results under diffusion-only conditions are discussed, as it is of particular interest for the work presented in the following chapters.

### **(i) Simulation at Single Electrodes**

Consider cyclic voltammetry in a redox solution, where change of the potential causes species to be either oxidised or reduced at the electrode surface. During electron transfer processes, electroactive species around an electrode are depleted to create a concentration gradient. Convection and migration effects are considered negligible such that the thickness of the depletion zone is limited by the rate of diffusion only. However, as seen in sections 1.2.2 and 1.2.3, the diffusion layer thickness,  $\delta$ , varies considerably with electrodes critical dimension,  $r$ , such that two general cases are considered: first, where the diffusion layer is small compared to the electrode critical dimension ( $\delta < r$ ), resulting in a diffusion-limited and time-dependent response, i.e., planar diffusion; and second, where it is large compared to the electrode critical dimension ( $\delta > r$ ), resulting in a steady-state and time-independent response, i.e., radial diffusion, see Figure 1.12. Hence planar diffusion is likely to occur at larger electrodes (e.g., microelectrodes), and radial diffusion is typical of much smaller electrodes (e.g., nanoelectrodes). Furthermore, in all cases, radial diffusion, planar diffusion and transition from radial to planar diffusion are dependent on the analysis time scale. The shorter the time scale, the smaller the growth of the diffusion layer, especially for larger electrodes, and thus the more likely planar diffusion dominates. Additionally, the electrode geometry can play an important role. For instance, disc, hemispherical and spherical electrodes will be more likely to exhibit radial diffusion, as opposed to band electrodes that will present planar diffusion, especially at the micrometre scale. Therefore, simulations in conjunction with experimental results provide a better understanding of the diffusional mass transport behaviour at single electrodes with respect to the electrode critical dimensions and geometry, and the analysis time.

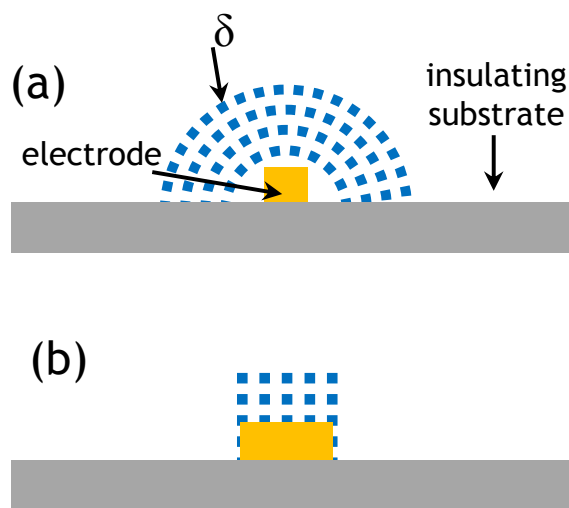


**Figure 1.12:** Schematic representation of (a) radial diffusion profile and (b) planar diffusion profile at single electrodes.

### (ii) Simulation at Electrode Arrays

At electrode arrays, mass transport is more complex as it is necessary to consider the distance between individual adjacent electrodes and the interaction between them. Therefore, the inter-electrode distance is a critical factor in the design of electrodes in array. Thus, simulations are used for the optimisation electrode array design prior to fabrication. Compton *et al* have pointed out four main regimes affecting diffusional mass transport to electrode arrays<sup>74-76</sup>, see Figure 1.13. These regimes are described by the relationship between the thickness of individual electrode diffusion layer,  $\delta$ , the electrode critical dimension,  $r$ , and the inter-electrode distance,  $d$ . For short analysis time, when the electrodes are well separated and individual diffusion layers are small compared to the electrode critical dimensions ( $\delta \ll r$ ), individual planar diffusion layers are observed, case (i), resulting in current tailing off. At high analysis time, for well separated electrodes, the diffusion layer thickness becomes comparable to the electrode critical dimension and no overlap between adjacent electrodes occurs ( $\delta = r < d$ ), thus individual radial diffusion layers are obtained, case (ii). However, at high analysis time for even smaller inter-electrode separations, overlapping of individual diffusion layers is likely to happen ( $r < \delta \leq d$ ), case (iii) in such way that the closer the electrodes, the greater the degree of overlap up until reaching complete overlap resulting in planar diffusion to the whole array ( $\delta \gg d$ ), case (iv). Electrode array designed and fabricated to work in regime (ii) are preferred for sweep voltammetry techniques as each electrode in the array behaves as an individual electrode, and the total measured current is that of

an individual electrode multiplied by the number of electrodes in the array. Under these conditions, the obtained voltammograms would be expected to be sigmoidal displaying steady-state currents. However, when regime (iii) or (iv) dominates the mass transport to the array, the measured current becomes significantly lower and tends to tail off, giving rise to peak-shaped responses. This reduction in signal would be observed because the electrode array behaves as a larger electrode of the same total area as that occupied by the entire array (electrodes and insulating area between them). By contrast, for pulsed voltammetry techniques, enhanced electrochemical behaviour is observed with electrode array designed and fabricated to work in regime (iii)<sup>77</sup>.

Broadly speaking, for most microelectrode and ultramicroelectrodes arrays, regimes (iii) and (iv) are more likely encountered because electrodes cannot be sufficiently spaced apart due to their micrometric size, whereas for nanoelectrode arrays, regime (ii) is easier to achieve because of the very small overall footprint the total array occupies. Note that the diffusion layer thickness depends dramatically on the diffusion coefficient as such that the higher the coefficient value, the earlier the diffusion layers will overlap.

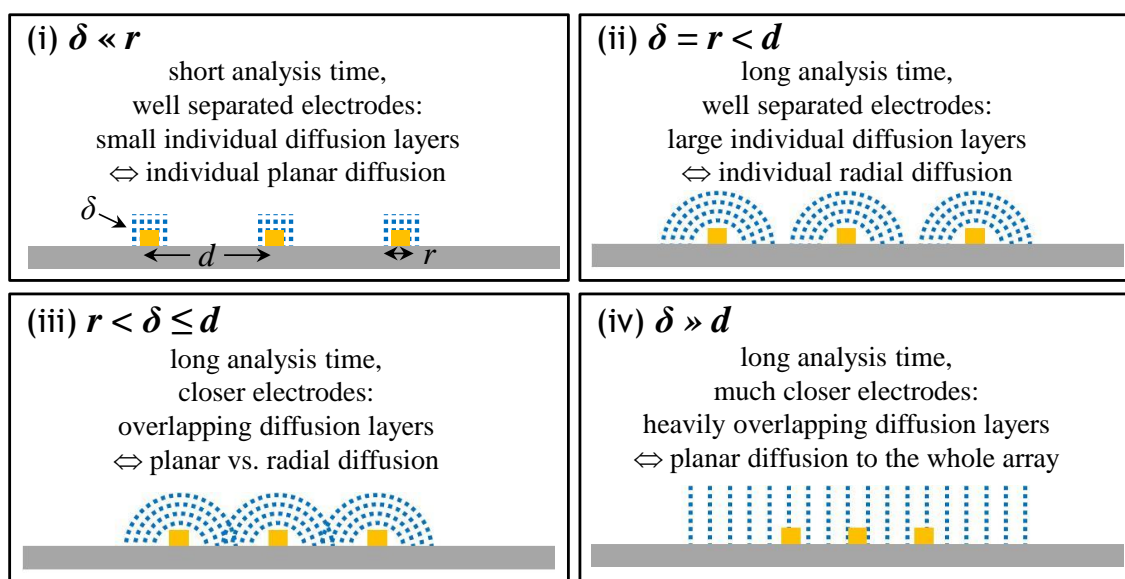


**Figure 1.13:** Schematic representation of the four different diffusion regimes that can occur at electrode arrays. (i)  $\delta \ll r$ , planar diffusion to each electrode, (ii)  $\delta = r < d$ , radial diffusion to each electrode, (iii)  $r < \delta \leq d$ , transition zone and (iv)  $\delta \gg d$ , planar diffusion to the entire array.

### (iii) Diffusion Domain Approach

Realistically, mass transport is a three-dimensional phenomenon, which is time consuming and complicated to solve. However, it is usually possible to approximate it

as a two-dimensional problem<sup>19, 76</sup>. This simplification is known as the diffusion domain approach, whereby the 3D shape of an electrode is divided into multiple, independent and highly symmetric 2D slices (unit cells). For instance, consider a homogeneously accessible microband electrode, which contribution of the edges to the total current is negligible compared to the contribution of the total surface. In this case, the diffusion is principally planar and only the diffusion normal to the electrode width can be considered, allowing the diffusional mass transport to the macroelectrode to be treated as a 2D or even as a 1D problem. However, at nanoelectrodes, the contributions of the edges to the total current cannot be neglected. In this case, the domain can be simplified from a 3D to a 2D problem, but not to a 1D problem. For instance, a homogeneously addressable rectangular nanoelectrode standing proud on an insulating surface, can be represented as a rectangle as seen in Figure 1.14.

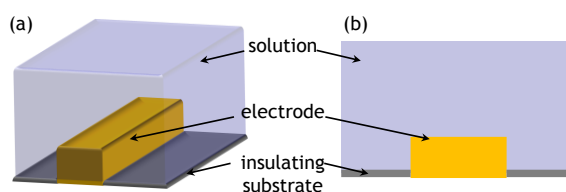


**Figure 1.14:** Schematic representation of (a) a three-dimensional and (b) a two-dimensional nanoelectrode domain.

## **1.4 Scope of Thesis**

The scope of this thesis is to explore top-down and bottom-up approaches for the fabrication and integration at technology relevant substrates of metal nanowire electrodes. The objective is to progressively fabricate and develop nanowire-based devices in order to explore electrochemically the benefits arising from their very small critical dimension compared to larger commonly used electrodes, towards sensing applications.

In Chapter 2, the fabrication of platinum/cobalt-platinum nanowires by template electrodeposition and associated difficulties and limitations with their subsequent integration at silicon/silicon dioxide substrates are discussed. Platinum nanowires comprising a cobalt-platinum tip with well controlled dimensions (25-40  $\mu\text{m}$  long and  $\sim 340$  nm in diameter) were fabricated. Electrodeposited nanowires were successfully assembled onto silicon/silicon dioxide chips using self-assembly approaches based on the magnetic interaction between nickel receptor sites contained on the chips and the nanowire cobalt-platinum tips. Assembled nanowires were easily located using binary alignment marks also patterned on the chips, in order to allow accurate overlay of contact electrodes. However, only the assembly and integration were very challenging such that only a very few attempts were successful. Nevertheless, contacted nanowires exhibited excellent electrical properties and preliminary electrochemical characterisation was carried out.

In Chapter 3, due to the challenge of integrating electrodeposited nanowires into functional devices, an alternative nanowire fabrication method was employed. Gold nanowire electrodes of reproducible critical dimensions (100 nm wide x 50 nm high and 45  $\mu\text{m}$  long) were fabricated onto silicon/silicon dioxide chips using electron-beam lithography and integrated into functioning devices by photolithography. A photoresist passivation layer was employed to insulate interconnection tracks from electrolytic solutions with a window selectively opened directly above the nanowire electrodes. Each chip was comprised of twelve separate electron beam fields containing single nanowires, a gold counter electrode, a platinum pseudo-reference electrode and peripheral contact pads that facilitated direct electrical probing and thereby eliminated the requirement for time consuming microelectronic packaging approaches. Subsequent

to device fabrication, nanowire electrodes were characterised structurally, electrically and electrochemically. The electrochemical performance exhibited by these nanowires was directly compared against the electrochemical performance of a single commercial gold microdisc electrode (6.25  $\mu\text{m}$  in radius).

In Chapter 4, arrays of three nanowires with reproducible dimensions (100 nm wide x 50 nm high and 45  $\mu\text{m}$  long) and with varying inter-electrode distances (5, 10, 15 or 20  $\mu\text{m}$ ) were fabricated at silicon/silicon dioxide chip substrates using the same hybrid electron beam – photolithography approach as in Chapter 3. The objective is to explore the diffusional mass transport with varying inter-electrode distances at fast scan rates using simulations and corresponding electrochemical experiments. Using cyclic voltammetry in ferrocene monocarboxylic acid, maximum signal was obtained when adjacent electrodes diffusion profiles are independent (i.e., separated by 15 or 20  $\mu\text{m}$ ). By contrast, using square wave voltammetry in ferrocene monocarboxylic acid, maximum signal was obtained when electrodes diffusion profiles overlap (i.e., separated by 5  $\mu\text{m}$ ).

In Chapter 5, single nanowire electrodes and arrays of two, three and four nanowire electrodes with reproducible dimensions (100 nm wide x 50 nm high and 45  $\mu\text{m}$  long) and an optimised inter-electrode distance (13  $\mu\text{m}$ ) were fabricated using the same hybrid fabrication technique as in Chapters 3 and 4. A simulation study combined with electrochemical characterisation of the nanowire arrays was performed to explore the diffusional process occurring at arrays with increasing number of nanowires.

In Chapter 6, the thesis concludes with a summary of the key results achieved in this work and thoughts on future work in this field.

## 1.5 References

1. Polk, B. J.; Stelzenmuller, A.; Mijares, G.; MacCrehan, W.; Gaitan, M., Ag/AgCl microelectrodes with improved stability for microfluidics. *Sensors and Actuators B: Chemical* **2006**, 114, 239-247.
2. Zhou, J.; Ren, K.; Zheng, Y.; Su, J.; Zhao, Y.; Ryan, D.; Wu, H., Fabrication of a microfluidic Ag/AgCl reference electrode and its application for portable and disposable electrochemical microchips. *Electrophoresis* **2010**, 31, 3083-3089.
3. Dawson, K.; Wahl, A.; Barry, S.; Barrett, C.; Sassiati, N.; Quinn, A. J.; O'Riordan, A., Fully integrated on-chip nano-electrochemical devices for electroanalytical applications. *Electrochimica Acta* **2014**, 115, 239-246.
4. Bond, A. M.; Lay, P. A., Cyclic voltammetry at microelectrodes in the absence of added electrolyte using a platinum quasi-reference electrode. *Journal of electroanalytical chemistry and interfacial electrochemistry* **1986**, 199, 285-295.
5. Ghilane, J.; Hapiot, P.; Bard, A. J., Metal/polypyrrole quasi-reference electrode for voltammetry in nonaqueous and aqueous solutions. *Analytical chemistry* **2006**, 78, 6868-6872.
6. Inzelt, G. Pseudo-reference Electrodes. In *Handbook of Reference Electrodes*; Springer: 2013, pp 331-332.
7. Marcus, R. A., Electron transfer reactions in chemistry. Theory and experiment. *Reviews of Modern Physics* **1993**, 65, 599-610.
8. Wang, X.; Tabakman, S. M.; Dai, H., Atomic layer deposition of metal oxides on pristine and functionalized graphene. *Journal of the American chemical Society* **2008**, 130, 8152-8153.
9. Barker, A. L.; Gonsalves, M.; Macpherson, J. V.; Slevin, C. J.; Unwin, P. R., Scanning electrochemical microscopy: beyond the solid/liquid interface. *Analytica chimica acta* **1999**, 385, 223-240.
10. Franaszczuk, K.; Herrero, E.; Zelenay, P.; Wieckowski, A.; Wang, J.; Masel, R., A comparison of electrochemical and gas-phase decomposition of methanol on platinum surfaces. *The Journal of Physical Chemistry* **1992**, 96, 8509-8516.
11. Zerby, S. E.; Ewing, A. G., Electrochemical monitoring of individual exocytotic events from the varicosities of differentiated PC12 cells. *Brain research* **1996**, 712, 1-10.
12. Bard, A. J.; Faulkner, L. R., *Electrochemical methods, fundamentals and applications*. **2001**.
13. Helmholtz, P., XLII.—On the modern development of Faraday's conception of electricity. *Journal of the Chemical Society, Transactions* **1881**, 39, 277-304.

14. Conway, B.; Bockris, J. M.; Ammar, I., The dielectric constant of the solution in the diffuse and Helmholtz double layers at a charged interface in aqueous solution. *Transactions of the Faraday Society* **1951**, 47, 756-766.
15. Torrie, G.; Valleau, J., Electrical double layers. 4. Limitations of the Gouy-Chapman theory. *The Journal of Physical Chemistry* **1982**, 86, 3251-3257.
16. Oldham, K. B., A Gouy–Chapman–Stern model of the double layer at a (metal)/(ionic liquid) interface. *Journal of Electroanalytical Chemistry* **2008**, 613, 131-138.
17. Henstridge, M. C.; Laborda, E.; Wang, Y.; Suwatchara, D.; Rees, N.; Molina, Á.; Martínez-Ortiz, F.; Compton, R. G., Giving physical insight into the Butler–Volmer model of electrode kinetics: Application of asymmetric Marcus–Hush theory to the study of the electroreductions of 2-methyl-2-nitropropane, cyclooctatetraene and europium (III) on mercury microelectrodes. *Journal of Electroanalytical Chemistry* **2012**, 672, 45-52.
18. Wang, J., In; John Wiley & Sons (New York): 2000.
19. Godino, N.; Borrise, X.; Munoz, F. X.; del Campo, F. J.; Compton, R. G., Mass transport to nanoelectrode arrays and limitations of the diffusion domain approach: theory and experiment. *The Journal of Physical Chemistry C* **2009**, 113, 11119-11125.
20. Molina, A.; Gonzalez, J.; Henstridge, M.; Compton, R., Voltammetry of Electrochemically Reversible Systems at Electrodes of Any Geometry: A General, Explicit Analytical Characterization. *The Journal of Physical Chemistry C* **2011**, 115, 4054-4062.
21. Zoski, C. G., *Handbook of electrochemistry*. Access Online via Elsevier: 2007.
22. Zhang, X.; Zhang, J.; Wang, R.; Liu, Z., Cationic surfactant directed polyaniline/CNT nanocables: synthesis, characterization, and enhanced electrical properties. *Carbon* **2004**, 42, 1455-1461.
23. Jain, P. K.; Huang, X.; El-Sayed, I. H.; El-Sayed, M. A., Noble Metals on the Nanoscale: Optical and Photothermal Properties and Some Applications in Imaging, Sensing, Biology, and Medicine. *Accounts of Chemical Research* **2008**, 41, 1578-1586.
24. Averitt, R. D.; Westcott, S. L.; Halas, N. J., Linear optical properties of gold nanoshells. *JOSA B* **1999**, 16, 1824-1832.
25. Rao, C.; Kulkarni, G.; Thomas, P. J.; Edwards, P. P., Size-dependent chemistry: Properties of nanocrystals. *Chemistry-a European Journal* **2002**, 8, 28-35.
26. Cahill, D. G.; Ford, W. K.; Goodson, K. E.; Mahan, G. D.; Majumdar, A.; Maris, H. J.; Merlin, R.; Phillpot, S. R., Nanoscale thermal transport. *Journal of Applied Physics* **2003**, 93, 793-818.

27. Salata, O. V., Applications of nanoparticles in biology and medicine. *Journal of nanobiotechnology* **2004**, 2, 3.
28. Snow, E.; Novak, J.; Lay, M.; Houser, E.; Perkins, F.; Campbell, P., Carbon nanotube networks: Nanomaterial for macroelectronic applications. *Journal of Vacuum Science & Technology B: Microelectronics and Nanometer Structures* **2004**, 22, 1990-1994.
29. Mauter, M. S.; Elimelech, M., Environmental applications of carbon-based nanomaterials. *Environmental Science & Technology* **2008**, 42, 5843-5859.
30. West, J. L.; Halas, N. J., Engineered nanomaterials for biophotonics applications: improving sensing, imaging, and therapeutics. *Annual Review of Biomedical Engineering* **2003**, 5, 285-292.
31. Cui, Y.; Wei, Q.; Park, H.; Lieber, C. M., Nanowire nanosensors for highly sensitive and selective detection of biological and chemical species. *Science* **2001**, 293, 1289-1292.
32. Patolsky, F.; Lieber, C. M., Nanowire nanosensors. *Materials Today* **2005**, 8, 20-28.
33. Arrigan, D. W., Nanoelectrodes, nanoelectrode arrays and their applications. *Analyst* **2004**, 129, 1157-1165.
34. Baughman, R. H.; Zakhidov, A. A.; de Heer, W. A., Carbon nanotubes--the route toward applications. *Science* **2002**, 297, 787-792.
35. Chen, S.; Wang, Z. L.; Ballato, J.; Foulger, S. H.; Carroll, D. L., Monopod, bipod, tripod, and tetrapod gold nanocrystals. *Journal of the American Chemical Society* **2003**, 125, 16186-16187.
36. Huang, H.; Yan, F.; Kek, Y.; Chew, C.; Xu, G.; Ji, W.; Oh, P.; Tang, S., Synthesis, characterization, and nonlinear optical properties of copper nanoparticles. *Langmuir* **1997**, 13, 172-175.
37. Song, Y.; Garcia, R. M.; Dorin, R. M.; Wang, H.; Qiu, Y.; Coker, E. N.; Steen, W. A.; Miller, J. E.; Shelnutt, J. A., Synthesis of platinum nanowire networks using a soft template. *Nano letters* **2007**, 7, 3650-3655.
38. Linehan, K.; Carolan, D.; Sé, D. Ó.; Doyle, H., Synthesis and Compositional Control of Size Monodisperse SixGe<sub>1-x</sub> Nanocrystals for Optoelectronic Applications. *MRS Online Proceedings Library* **2013**, 1551, mrss13-1551-r02-03.
39. Menon, V. P.; Martin, C. R., Fabrication and evaluation of nanoelectrode ensembles. *Analytical Chemistry* **1995**, 67, 1920-1928.
40. Lanyon, Y. H.; Arrigan, D. W., Recessed nanoband electrodes fabricated by focused ion beam milling. *Sensors and Actuators B: Chemical* **2007**, 121, 341-347.

41. Nagale, M. P.; Fritsch, I., Individually addressable, submicrometer band electrode arrays. 1. Fabrication from multilayered materials. *Analytical Chemistry* **1998**, 70, 2902-2907.
42. Chen, S.; Kucernak, A., The voltammetric response of nanometer-sized carbon electrodes. *The Journal of Physical Chemistry B* **2002**, 106, 9396-9404.
43. Conyers, J. L.; White, H. S., Electrochemical characterization of electrodes with submicrometer dimensions. *Analytical chemistry* **2000**, 72, 4441-4446.
44. Mirkin, M. V.; Fan, F.-R. F.; Bard, A. J., Scanning electrochemical microscopy part 13. Evaluation of the tip shapes of nanometer size microelectrodes. *Journal of Electroanalytical Chemistry* **1992**, 328, 47-62.
45. Wong, D. K.; Xu, L. Y., Voltammetric studies of carbon disk electrodes with submicrometer-sized structural diameters. *Analytical Chemistry* **1995**, 67, 4086-4090.
46. Liu, Y.; He, R.; Zhang, Q.; Chen, S., Theory of electrochemistry for nanometer-sized disk electrodes. *The Journal of Physical Chemistry C* **2010**, 114, 10812-10822.
47. Li, Y.; Bergman, D.; Zhang, B., Preparation and electrochemical response of 1–3 nm Pt disk electrodes. *Analytical chemistry* **2009**, 81, 5496-5502.
48. McCulloch, S.; Uttamchandani, D., A simple reproducible technique for producing sub-micrometre fibre-optic probes for near-field optical microscopy and chemical sensors. *Measurement Science and Technology* **1995**, 6, 1157.
49. Cox, J. T.; Zhang, B., Nanoelectrodes: Recent Advances and New Directions. *Annual Review of Analytical Chemistry* **2012**, 5, 253-272.
50. Liu, B.; Rolland, J. P.; DeSimone, J. M.; Bard, A. J., Fabrication of Ultramicroelectrodes Using A “Teflon-like” Coating Material. *Analytical chemistry* **2005**, 77, 3013-3017.
51. Mbindyo, J. K.; Mallouk, T. E.; Mattzela, J. B.; Kratochvilova, I.; Razavi, B.; Jackson, T. N.; Mayer, T. S., Template synthesis of metal nanowires containing monolayer molecular junctions. *Journal of the American Chemical Society* **2002**, 124, 4020-4026.
52. Brumlik, C. J.; Menon, V. P.; Martin, C. R., Template synthesis of metal microtubule ensembles utilizing chemical, electrochemical, and vacuum deposition techniques. *Journal of Materials Research* **1994**, 9, 1174-1183.
53. Sun, S., Recent advances in chemical synthesis, self-assembly, and applications of FePt nanoparticles. *Adv. Mater.* **2006**, 18, 393-403.
54. Brewster, M. M.; Zhou, X.; Lim, S. K.; Gradecak, S., Role of Au in the Growth and Nanoscale Optical Properties of ZnO Nanowires. *Journal of Physical Chemistry Letters* **2011**, 2, 586-591.

55. Chakraborty, S.; Raj, C. R., Carbon nanotube supported platinum nanoparticles for the voltammetric sensing of hydrazine. *Sensors and Actuators B: Chemical* **2010**, 147, 222-227.
56. Lovera, P.; Jones, D.; Corbett, B.; O'Riordan, A., Polarization tunable transmission through plasmonic arrays of elliptical nanopores. *Optics express* **2012**, 20, 25325-25332.
57. Maillard, M.; Huang, P.; Brus, L., Silver nanodisk growth by surface plasmon enhanced photoreduction of adsorbed [Ag<sup>+</sup>]. *Nano Letters* **2003**, 3, 1611-1615.
58. Dawson, K.; Wahl, A. I.; Murphy, R.; O'Riordan, A., Electroanalysis at Single Gold Nanowire Electrodes. *The Journal of Physical Chemistry C* **2012**, 116, 14665-14673.
59. Reboud, V.; Lévêque, G.; Striccoli, M.; Placido, T.; Panniello, A.; Curri, M.; Alducin, J.; Kehoe, T.; Kehagias, N.; Mecerreyes, D., Metallic nanoparticles enhanced the spontaneous emission of semiconductor nanocrystals embedded in nanoimprinted photonic crystals. *Nanoscale* **2013**, 5, 239-245.
60. Akahane, Y.; Asano, T.; Song, B.-S.; Noda, S., Fine-tuned high-Q photonic-crystal nanocavity. *Optics express* **2005**, 13, 1202-1214.
61. Keeley, G. P.; Lyons, M. E., The effects of thin layer diffusion at glassy carbon electrodes modified with porous films of single-walled carbon nanotubes. *Int. J. Electrochem. Sci* **2009**, 4, 794-809.
62. Martin, C. R., Template synthesis of electronically conductive polymer nanostructures. *Accounts of chemical research* **1995**, 28, 61-68.
63. Chen, C. L.; Rosi, N. L., Peptide-Based Methods for the Preparation of Nanostructured Inorganic Materials. *Angewandte Chemie International Edition* **2010**, 49, 1924-1942.
64. Sotiropoulou, S.; Chaniotakis, N. A., Carbon nanotube array-based biosensor. *Analytical and Bioanalytical Chemistry* **2003**, 375, 103-105.
65. Lin, Y.; Yantasee, W.; Wang, J., Carbon nanotubes (CNTs) for the development of electrochemical biosensors. *Front. Biosci* **2005**, 10, 582.
66. Lanyon, Y. H.; De Marzi, G.; Watson, Y. E.; Quinn, A. J.; Gleeson, J. P.; Redmond, G.; Arrigan, D. W., Fabrication of nanopore array electrodes by focused ion beam milling. *Analytical chemistry* **2007**, 79, 3048-3055.
67. Mårtensson, T.; Borgström, M.; Seifert, W.; Ohlsson, B.; Samuelson, L., Fabrication of individually seeded nanowire arrays by vapour-liquid-solid growth. *Nanotechnology* **2003**, 14, 1255.
68. Sun, Y.; Yin, Y.; Mayers, B. T.; Herricks, T.; Xia, Y., Uniform silver nanowires synthesis by reducing AgNO<sub>3</sub> with ethylene glycol in the presence of seeds and poly (vinyl pyrrolidone). *Chemistry of Materials* **2002**, 14, 4736-4745.

69. Qian, C.; Kim, F.; Ma, L.; Tsui, F.; Yang, P.; Liu, J., Solution-phase synthesis of single-crystalline iron phosphide nanorods/nanowires. *Journal of the American Chemical Society* **2004**, 126, 1195-1198.
70. Dawson, K.; Strutwolf, J. r.; Rodgers, K. P.; Herzog, G. g.; Arrigan, D. W.; Quinn, A. J.; O'Riordan, A., Single nanoskived nanowires for electrochemical applications. *Analytical chemistry* **2011**, 83, 5535-5540.
71. Gates, B. D.; Xu, Q.; Stewart, M.; Ryan, D.; Willson, C. G.; Whitesides, G. M., New approaches to nanofabrication: molding, printing, and other techniques. *Chemical reviews* **2005**, 105, 1171-1196.
72. Natelson, D., Fabrication of metal nanowires. *arXiv preprint cond-mat/0307600* **2003**.
73. Xiang, C.; Kung, S.-C.; Taggart, D. K.; Yang, F.; Thompson, M. A.; Guell, A. G.; Yang, Y.; Penner, R. M., Lithographically patterned nanowire electrodeposition: A method for patterning electrically continuous metal nanowires on dielectrics. *Acs Nano* **2008**, 2, 1939-1949.
74. Compton, R. G.; Wildgoose, G. G.; Rees, N. V.; Streeter, I.; Baron, R., Design, fabrication, characterisation and application of nanoelectrode arrays. *Chemical Physics Letters* **2008**, 459, 1-17.
75. Rees, N. V.; Compton, R. G., Voltammetry as a probe of displacement. *Chemical Communications* **2010**, 46, 4238-4248.
76. Davies, T. J.; Compton, R. G., The cyclic and linear sweep voltammetry of regular and random arrays of microdisc electrodes: Theory. *Journal of Electroanalytical Chemistry* **2005**, 585, 63-82.
77. Wahl, A.; Dawson, K.; MacHale, J.; Barry, S.; Quinn, A.; O'Riordan, A., Gold nanowire electrodes in array: Simulation study and experiments. *Faraday Discuss.* **2013**.

## *Chapter 2*

# **Fabrication, Assembly and Characterisation of Platinum/Cobalt-Platinum Two-Part Nanowires**



## 2.1 Introduction

In the last few decades, the development of miniaturised sensors based on electrochemical detection techniques has increased dramatically such that nanoelectrodes are the next step in electrode miniaturisation<sup>1-3</sup>. In this regard, as the critical dimension of an electrode enters the nano regime, radial analyte diffusion is expected to dominate, which would result in increased rates of mass transport, higher current densities and steady-state voltammograms even at high measurement rates<sup>2</sup>. In addition, the very small size of nanoelectrodes would require low sample volume and enable reduced double layer capacitance resulting in higher signal-to-noise ratios and enhanced sensitivity in a wide range of sensing applications<sup>4,5</sup>. For example, emerging devices that employ metal nanowire electrodes for direct, sensitive and rapid detection of biological and chemical species represent a new and powerful class of electrochemical sensors because of their excellent electrical and electrochemical properties<sup>6-8</sup>. However, only recent advances in nanofabrication techniques have enabled the fabrication of such devices<sup>9-11</sup>.

A reproducible, inexpensive, simple and versatile process for the synthesis of high yield of metal nanowires with well-defined geometry and dimensions is the template electrodeposition method<sup>12-14</sup>. In this approach, a metal, e.g., platinum, is electrochemically deposited and grown into a porous template with pore dimensions close to the desired final nanowire size, e.g., anodic aluminium oxide template. Nanowires may then be released in aqueous media by selective dissolution of the template. As well as the pore dimensions, electrodeposited nanowires dimension also depend on parameters and conditions such as applied potential, electrodeposition duration, electrolyte concentration, temperature. However, the manipulation of electrodeposited nanowires in a rational and controlled manner is very difficult as attractive forces between them can prevent their successful release or placement onto appropriate substrates<sup>15, 16</sup>. These attractive forces include electrostatic<sup>17</sup>, capillary<sup>18</sup> and Van der Waals forces<sup>19</sup>, which are insignificant at the macro scale, but as the component size decrease down to the nanoscale, they dominate over the gravitational forces required for components release<sup>20</sup>. Consequently, assembling and integrating

electrodeposited nanowires at technologically relevant substrates to fabricate sensor devices is very challenging.

In this Chapter, to address this limitation, we are exploring nanowires partially composed of a magnetic material to drive the assembly of the nanowires at predefined magnetic sites at silicon chip substrates. We employ the template electrodeposition technique to fabricate discrete platinum nanowires with a magnetic cobalt-platinum tip for potential use in electrochemical applications<sup>21, 22</sup>. A combination of scanning electron microscopy, optical microscopy, energy dispersive X-ray spectroscopy and X-ray diffraction is used for their structural and elemental characterisation. Several million highly uniform nanowires of length 25-40  $\mu\text{m}$  for platinum and about 1  $\mu\text{m}$  for cobalt-platinum were typically fabricated; 1  $\text{cm}^2$  of template can produce up to  $10^9$  nanowires. To demonstrate their potential use in electrochemical applications, we then investigated several self-assembly and robotic approaches to integrate electrodeposited nanowires onto silicon chips containing nickel receptor pads. Assembled nanowires were then contacted with overlaid micron scale gold structures and passivated with  $\sim 1$   $\mu\text{m}$  thick photoresist layer. A window in this layer was then selectively opened to allow contact between the nanowire and a solution of interest. Following fabrication and integration, nanowire devices were electrically characterised. Preliminary electrochemical measurements in ferrocene monocarboxylic acid solution were also carried out, but further investigations are required as misalignment of the opening in the passivation layer may have exposed binary markers which could have contributed to the measured signals. Work is now on-going to address the misalignment issue.

---

This work is in preparation for publication as ‘Fabrication, Assembly and Characterisation of Platinum/Cobalt-Platinum Segmented Nanowires at Technology Relevant Silicon Chip Substrates’ in *Journal of The Electrochemical Society*.

## 2.2 Experimental

### 2.2.1 Synthesis of Platinum Nanowires with a Cobalt-Platinum Tip

Platinum/Cobalt-Platinum (Pt/CoPt) nanowires were electrodeposited in porous anodised alumina oxide membranes (AAO, Anodisc 13; 200 nm nominal pore diameter, Whatman Ltd.). Gold was evaporated for 500 s using a gold sputter (Scancoat Six Edwards Sputter Coater) to form a conductive layer onto one side of the membrane. The membrane was then attached to the iron surface of a holder using an insulating Teflon cap. It was mounted facing upwards, i.e., the gold side in contact with the iron surface of the electrochemical cell, to form a working electrode.<sup>23</sup> A platinum wire acted as the counter electrode and a saturated silver/silver chloride electrode was used as the reference electrode (CH Instruments). Platinum was first electrodeposited by immersing an AAO working electrode, along with the counter and reference electrodes, into a solution of 2% w/w hexachloroplatinic acid ( $\text{H}_2\text{PtCl}_6$ ) acidified to pH 3 with a few drops of concentrated sulphuric acid ( $\text{H}_2\text{SO}_4$ ). A potential of -0.225 V was applied for about 330 minutes, followed by a thorough rinse of the electrodes with deionised water. Cobalt-Platinum was then electrodeposited by immersing the electrodes into a solution of 2% w/w cobalt (II) chloride ( $\text{CoCl}_2$ ) and 0.5% w/w platinum (IV) chloride ( $\text{PtCl}_4$ ) acidified to pH 3 with a few drops of concentrated sulphuric acid. A potential of -0.961 V was applied for 30 minutes, followed by a thorough rinse of the electrodes with deionised water. Following the two-step electrodeposition process, the Pt/CoPt nanowires were liberated by dissolving the AAO membrane in 1 mL of 3 M sodium hydroxide (NaOH) solution for about 24 hours. The nanowire material was extracted from the resulting mixture by five cycles of centrifugation (centrifuge 5415D, Eppendorf®; optimised parameters: 8000 rpm, 120 s), supernatant removal followed by re-dispersion in deionised water. The entire membrane was not completely dissolved; a portion was kept for further analysis. In order to facilitate elemental characterisation, pristine Pt and CoPt nanowires were also fabricated using either of the two electrodeposition steps. Figure 2.1 illustrates the Pt/CoPt nanowires synthesis followed by their liberation.

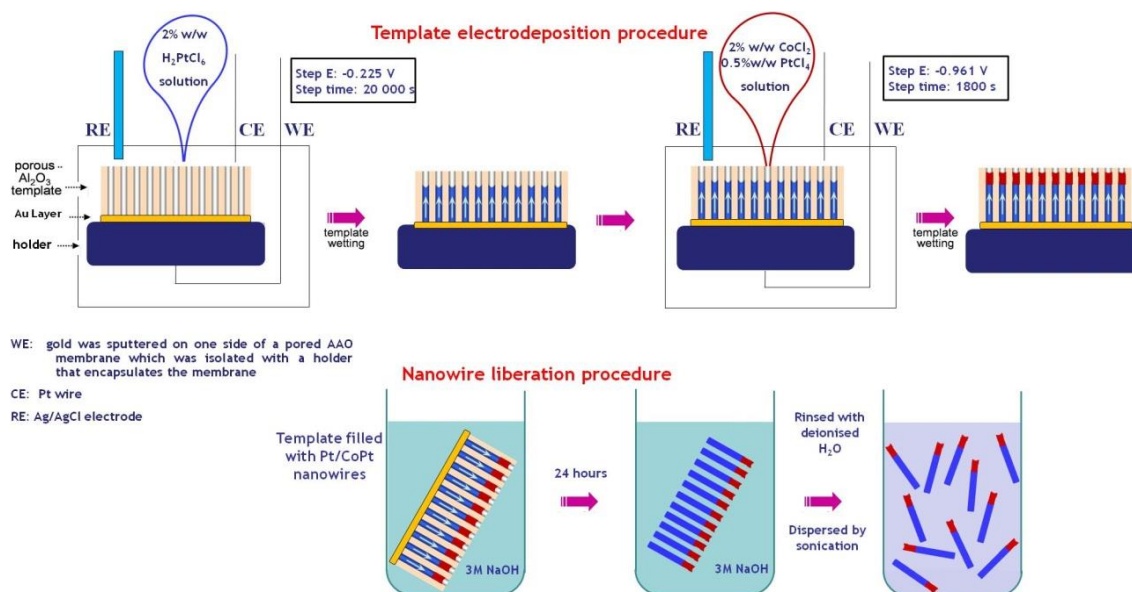


**Figure 2.1:** Schematic diagram of the synthesis of Pt/CoPt nanowires by template electrodeposition and their liberation procedure.

### 2.2.2 Structural Characterisation of Pt/CoPt Nanowires

Pt/CoPt nanowires were structurally characterised using optical microscopy and scanning electron microscopy. The sample preparation was simple;  $\mu\text{L}$  aliquots of nanowires in suspension were dispensed onto glass cover slips for optical analysis or onto highly doped silicon substrates for scanning electron microscopic inspection, followed by drying in an oven at  $40\text{ }^\circ\text{C}$  for about 20 minutes. Optical micrographs were acquired using a calibrated microscope (Axioskop II, Carl Zeiss Ltd.) equipped with a charge-coupled detector camera (CCD; DEI-750, Optronics). Scanning electron micrographs were acquired using a field emission scanning electron microscope (JSM-6700F, JEOL UK Ltd.) operating at beam voltages between 5 and 10 kV.

### 2.2.3 Elemental Characterisation of Pt/CoPt Nanowires

Pt/CoPt nanowires elemental composition was analysed using a combination of scanning electron microscopy, energy-dispersive X-ray spectroscopy and X-ray diffraction analysis. The sample preparation for scanning electron microscopic characterisation is the same as described above; additionally nanowires were dispersed on gold and silicon/silicon dioxide substrates. For energy-dispersive X-ray spectroscopy and X-ray dispersion analysis, pieces of membrane containing the Pt/CoPt

nanowires were stuck on a carbon pad; the side with gold was slightly polished to remove as much gold as possible and was stuck directly onto the pad.

#### 2.2.4 Pt/CoPt Nanowires Assembly, Integration and Packaging

Pt/CoPt nanowires were integrated onto 8.1 mm x 8.1 mm silicon receptor chips with ~90 nm of thermally grown oxide (Si/SiO<sub>2</sub>). Each chip was patterned with 16 individually labelled grids in a 4 x 4 array format and separated by 200 μm, as shown in Figure 2.2 (a). Each grid consists of 1024 binary mark identifiers in a 32 x 32 array format with a 45 μm pitch, as represented in Figures 2.2 (b) and (c). Each binary mark consists of 2 start bits and 10 bits defined by the presence (on) or absence (off) of a gold square respectively denoting 1 or 0, see Figure 2.2 (d). The first two bits, labelled ‘S, S’ in Figure 2.2 (d) are always present (on). All the alignment marks differ from each other by switching on and off the 10 specific bits in the binary code (i.e.  $2^{10} = 1024$ ). In this manner each of the 1024 binary alignment marks have a distinct and unique shape. These binary markers were designed by Dr Aidan J. Quinn (Nanotechnology Group, Tyndall National Institute). Each binary mark was patterned by optical lithography, metal evaporation (Ti/Au, 10/200 nm) and lift-off techniques. Following their deposition, 5 to 10 nickel pads (2 x 3 μm) were accurately deposited between 2 consecutive binary marks by optical lithography, metal evaporation (Ti/Ni, 10/100 nm) and lift-off techniques. The process was done on a wafer level; wafers were diced into chips at the end of the fabrication process.

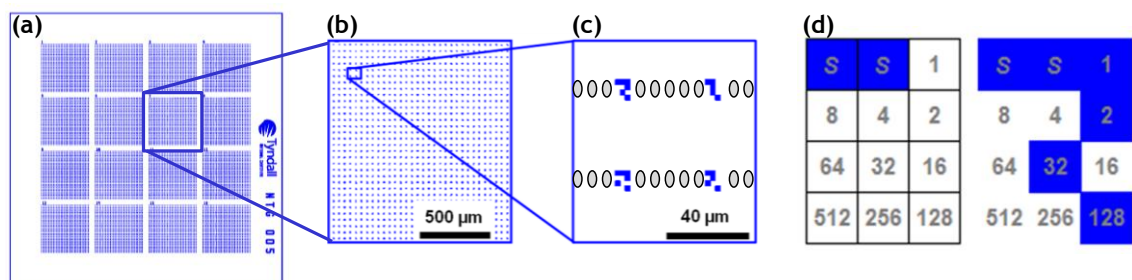


**Figure 2.2:** Schematic representations of (a) Si/SiO<sub>2</sub> chip design containing 16 individual grids in a 4 x 4 array format, (b) one grid consisting of 1024 binary mark identifiers in a 32 x 32 array format, (c) target area consisting of binary marks and nickel pads. (d) Each binary alignment mark consists of 2 start bits and 10 bits defined by the presence (on) or absence (off) of a gold pixel (lithographically patterned in that bit) denoting 1 or 0 respectively.

Several robotic and self-assembly approaches were investigated, based on the magnetic attraction between nickel pads and the cobalt-platinum tip of nanowires, which are further discussed in the subsections 2.3.4. and 2.3.5. In these approaches, liberated Pt/CoPt nanowires were deposited onto clean Si/SiO<sub>2</sub> chips containing gold binary marks and nickel pads, as illustrated in Figure 2.3 (a). Si/SiO<sub>2</sub> chips were cleaned by sequential immersion for 10 minutes in acetone (bath 1), trichloroethylene, acetone (bath 2), isopropyl alcohol and deionised water, followed by drying with a filtered stream of nitrogen. The objective is to employ binary identifiers to easily identify the position of an assembled Pt/CoPt nanowire for accurate overlay of contact electrodes along with gold counter and reference electrodes, see Figure 2.3 (b). To this end, optical lithography, metal evaporation (Ti/Au, 10/200 nm) and lift-off techniques were used. A  $\sim 1 \mu\text{m}$  thick photoresist passivation layer was spin coated onto the die. A window in this layer was then selectively opened using lithography to only expose the underlying Pt nanowire, as well as gold counter and pseudo-reference electrodes. Control devices were fabricated by depositing the contacting architecture and passivation onto a die without a nanowire.

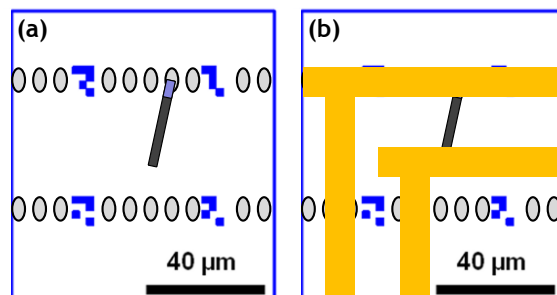


**Figure 2.3:** Overview of the assembly and electrical interconnection of individual nanowires on Si/SiO<sub>2</sub> chips. Schematic representations of (a) Pt/CoPt nanowire assembled on a nickel pad, (b) overlaid gold contact electrodes.

### 2.2.5 Electrical Characterisation of Pt/CoPt Nanowire Electrodes

Electrical measurements were performed using a probe station (PML-8000, Wentworth Laboratories, U.K.). Two manual linear motion probes (PVX 500, Wentworth Labs Ltd) were placed onto two overlaid gold pads, which contained an electrodeposited Pt/CoPt nanowire between them. To undertake electrical characterisation, a parameter analyser (HP4156a, Agilent Technologies, U.K.) with a voltage resolution  $< 100 \mu\text{V}$  and a current resolution  $< 100 \text{ fA}$  was programmed using Agilent VEE Pro 6.0 software. For these current-voltage measurements, the source electrode was grounded,

a bias sweep up to  $\pm 10$  mV was applied to the drain electrode, and the current through the nanowire was measured.

### **2.2.6 Electrochemical Characterisation**

A handheld potentiostat (pocketSTAT, Ivium) was employed for all electrochemical studies. Experiments were carried out in a three-electrode electrochemical cell employing single Pt/CoPt nanowire working electrodes, with on-chip gold counter and pseudo-reference electrodes. Three manual linear motion probes (PVX 500, Wentworth Labs Ltd) were used to connect the three electrodes to the handheld potentiostat. All equipment was placed in a faraday cage. Cyclic voltammetry measurements were carried out in 1 mM ferrocene monocarboxylic acid in 10 mM phosphate buffered saline solutions at pH 7.4 and deaerated with nitrogen gas prior to electrochemical analysis.

### **2.2.7 Chemicals and Glassware**

Unless otherwise stated, all chemicals were purchased from Sigma-Aldrich and were used without further purification. Stock solutions were prepared on a monthly basis but the pH was checked before each set of experiments. All solutions were prepared with deionised water of resistivity 18.2 M $\Omega$ .cm (Millipore Q).

## 2.3 Results and Discussion

### 2.3.1 Morphological Analysis of Commercial Anodic Alumina Oxide Templates

In this work, commercial porous anodic alumina oxide (AAO) templates with an average 60  $\mu\text{m}$  thickness were used to grow Pt, CoPt and Pt/CoPt nanowires. These membranes were manufactured electrochemically using high purity aluminium sheets, and are characterised by highly ordered, straight, parallel channels with an average 200 nm pore diameter and a density of about  $10^9$  pores. $\text{cm}^{-2}$ . Figure 2.4 (a) shows a top-view scanning electron micrograph of an AAO membrane, which reveals a honeycomb structure of close-packed and uniform pores. A cross-sectional scanning electron micrograph of an AAO template showing the uniform and straight cylindrical shape of pores is presented in Figure 2.4 (b).

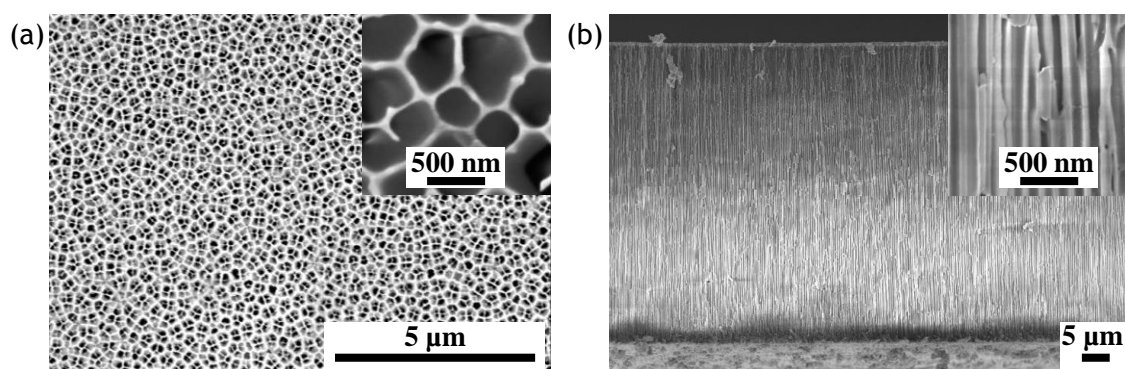


**Figure 2.4:** (a) Top-view and (b) cross-sectional view scanning electron micrographs of a commercial Anodic Alumina Oxide template.

### 2.3.2 Structural Characterisation

Following fabrication, analysis using a scanning electron microscope was undertaken to characterise the electrodeposited Pt/CoPt nanowires dimensions. Figure 2.5 (a) is a top view and figure 2.5 (b) is a cross-sectional image of the electrodeposited nanowire arrays. Both figures show high yields of uniform, cylindrical, straight and parallel nanowires consistent with the shape of the nominal pores contained in the alumina membranes. Statistical analysis yielded an average diameter of  $340 \pm 21$  nm. Their length can be controlled in the range from 1  $\mu\text{m}$  to about 40  $\mu\text{m}$  according to the deposition time. Although high yields were obtained, characterisation of dense mats as well as single nanowires was possible by adequate dilution in the dispersing solvent,

deionised water. Figure 2.5 (c) shows typical nanowires of  $\sim 25 \mu\text{m}$  in length. While high yields of nanowires of desired shape and size were synthesised, it is crucial to confirm their elemental composition, since the objective is to fabricate platinum nanowires composed of a magnetic cobalt-platinum portion. Nanowires composed of a magnetic material should facilitate their assembly and integration on substrates containing predefined magnetic sites.

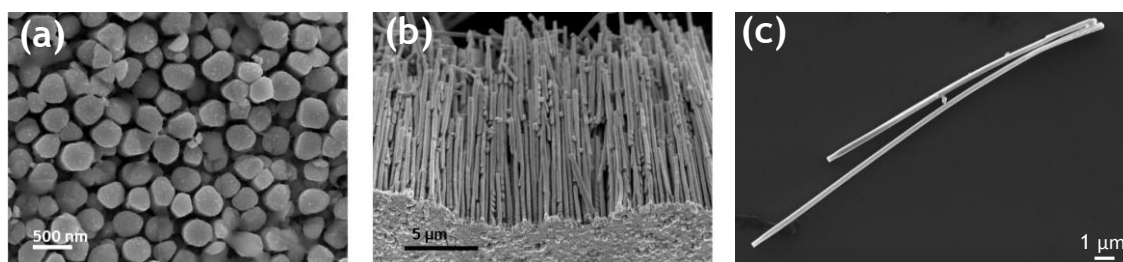


**Figure 2.5:** Scanning electron micrographs of (a) top view, (b) side view of highly ordered Pt/CoPt nanowires of  $\sim 340 \text{ nm}$  in diameter, and (c) single nanowires of  $\sim 25 \mu\text{m}$  in length.

### 2.3.3 Elemental Characterisation

A scanning electron microscope was employed to highlight the nanowires compositional difference. Figures 2.6 (a) and (b) are scanning electron micrographs of the same sample, using the secondary electron and backscattered electron detectors, respectively. The interface between phases is even more obvious using the backscattered electron detector in high resolution on an isolated single nanowire, as shown in Figures 2.6 (c) and (d). It can be seen that the nanowires are made of two different materials; one of about 25 to 40  $\mu\text{m}$  long (light material) and the other of about 0.5-1  $\mu\text{m}$  long (dark material). Moreover, the diameter of the small CoPt extremity appears slightly smaller than the overall nanowire diameter, implying that CoPt did not completely fill the anodic alumina oxide template pores. A possible reason for that would be the magnetic repulsion between adjacent CoPt nanowires during their growth. Although there is an obvious difference in composition using the backscattered electron detector, scanning electron microscopy does not allow for the determination of element composition of the nanowires. Thus further analysis is required to confirm whether or not the nanowires are made of platinum with a platinum-cobalt alloy tip.

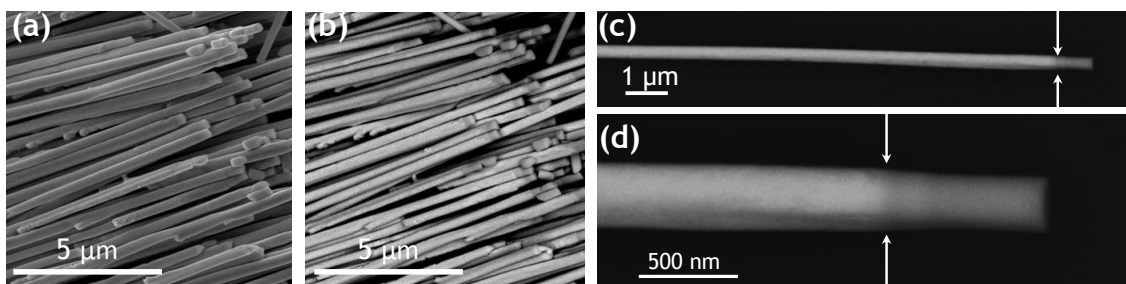


**Figure 2.6:** Scanning electron micrographs of typical Pt/CoPt nanowires array using (a) a secondary electron detector and (b) a backscattered electron detector. (c) Scanning electron micrograph of a single Pt/CoPt nanowire using a backscattered electrode detector, the arrows show the interface between the Pt and CoPt regions. (d) Higher magnification of the interface shown in (c).

To this end, energy-dispersive X-ray spectroscopy was employed as a qualitative method to identify elemental composition. Analysis was carried out on pristine CoPt nanowires fabricated using one of the two electrodeposition steps required for the synthesis of multilayer Pt/CoPt nanowires. The presence of both cobalt and platinum were observed in spectra of CoPt nanowires, as shown in Figure 2.7. Peaks denoting oxygen, aluminium, phosphorous and carbon were observed, probably due to residual amounts of the dissolved alumina template and the carbon-coated copper sample grids. This was confirmed by energy-dispersive X-rays spectra of an empty AAO template on a carbon-coated copper grid (see appendix A.2).

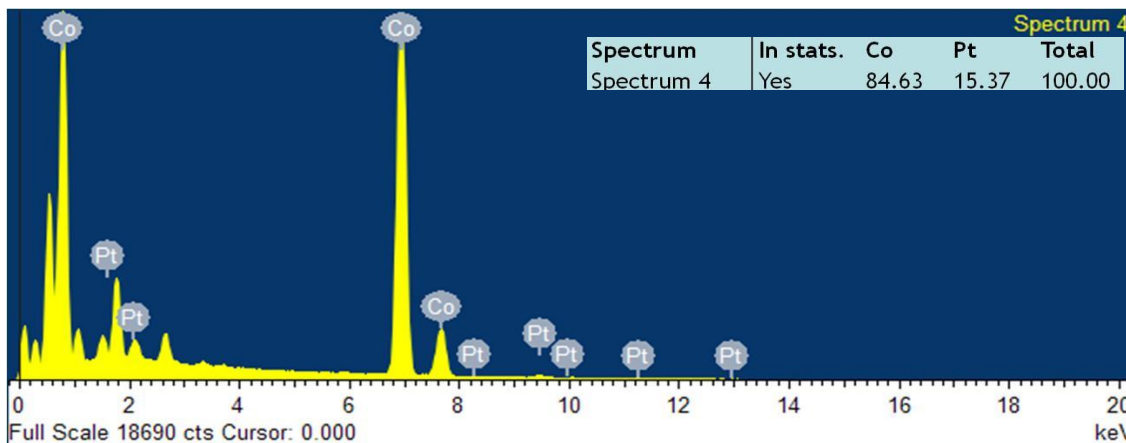


**Figure 2.7:** Energy-dispersive X-ray spectrum taken on CoPt nanowires:  $\text{Co}_{0.85}\text{Pt}_{0.15}$

Furthermore, X-ray diffraction was performed to determine the crystal phase of the nanowires. Nanowire samples were typically radiated by a continuous monochromatic beam of Cu  $K_{\alpha}$  X-rays, with an incoming wavelength,  $\lambda$ , equal to 1.54056 Å. The detector was rotated over an angle range from 10 to 90° with an increment of 0.0167°,

and the intensity was measured (in counts) for 15 s per step. X-ray diffraction patterns of as deposited CoPt nanowires typically exhibited four peaks, as shown in Figure 2.8. Two of these peaks, at  $2\theta = 41.5^\circ$  and  $2\theta = 47.2^\circ$ , could be indexed as the (101) and (110) reflections of the tetragonal phase ( $L1_0$ ) of CoPt, respectively<sup>24</sup>. The remaining two peaks at  $2\theta = 38.2^\circ$  and  $2\theta = 44.5^\circ$ , could be indexed as the (111) and (200) reflection peaks of cubic gold<sup>24</sup>, which would be due to the presence of the underlying conductive gold layer. Peak positions of the main peaks reported for the bulk phases of CoPt,  $\text{CoPt}_3$ , Au, Pt and Co are shown for comparison.

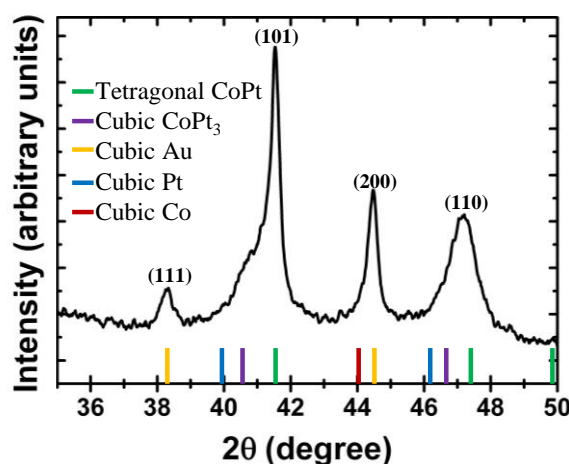


**Figure 2.8:** X-Ray Diffraction spectrum of CoPt nanowires

### 2.3.4 Robotic Assembly Approaches

Following their fabrication and liberation, the objective is to assemble Pt/CoPt nanowires onto Si/SiO<sub>2</sub> chip substrates comprising nickel receptor sites. In the robotic approach, the idea is to mechanically pick individual Pt/CoPt nanowires and to place them onto the nickel receptors, as the interaction between CoPt and nickel should be stronger than the interaction between the nanowires and the picking tools. The instrument used was a Tescan Mira scanning electron microscope with in-built metallic Piezzo grippers and micro needles.

#### (i) Piezzo Grippers

Piezo grippers were initially used to lift-up and move the nanowires towards the nickel receptor sites. They are made of two joint micrometric arms which can be activated either independently or together using nanomanipulators. It is crucial to align both arms in order to be able to pick and place the nanowires correctly. However, this was very

challenging and consequently was time consuming. Figure 2.9 (a) shows non-aligned arms at the start of the manipulation. Figures 2.9 (b) and (c) respectively are pictures of arms of a piezo gripper that are finally aligned in a closed position (touching each other) and in an open position (apart from each other). Moreover, piezo grippers tips were found to be too large compared to the nanowires dimensions as can be clearly seen in Figure 2.9 (d).

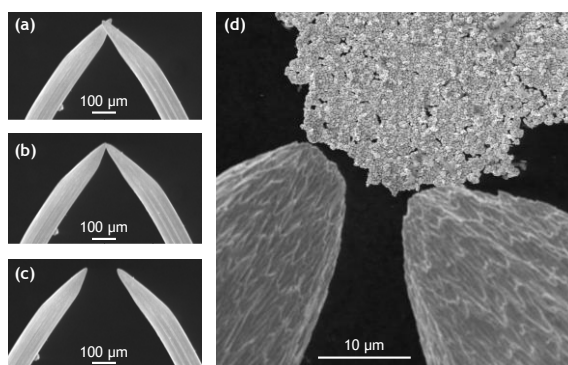


**Figure 2.9:** Scanning electron micrographs of the arms of a Piezo gripper in (a) a non-aligned position, (b) in a closed and aligned position, (c) in an open and aligned position and (d) next to a nanowire sample.

### (ii) Two Independent Micro Needles

Following the unsuccessful attempt of using Piezo grippers, picking with two independent micro needles was tried. The needles are mounted on two separate nanomanipulators to allow individual control of their movement. This method enabled the gripping of a bunch of nanowires quite easily but not single nanowires, as it can be seen in Figure 2.10 (a), thereby demonstrating the difficulty in manipulating individual nanowires in a controlled and rational manner because attractive forces (mainly electrostatic and Van der Waals forces, as under vacuum condition there are no capillary forces) dominate over gravitational forces<sup>25</sup>. Moreover, releasing the nanowires onto a Si/SiO<sub>2</sub> chip failed every time, as seen in figure 2.10 (b); nanowires broke when released, thereby damaging the chip surface. This was due to the dominance of attractive forces but also because of the limited manipulation options of the nanomanipulators. Effectively, although the individual control of the needles is an advantage, it becomes a problem when nanowires are stuck between them. In such case care must be taken to move the needles in the same direction and at the same time without losing the nanowires, which at the nano and micro scale is very difficult.

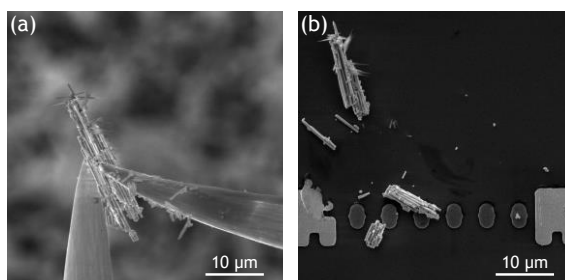


**Figure 2.10:** Scanning electron micrographs of (a) a bunch of nanowires stuck between two independent micro needles and (b) broken nanowires released on a silicon/silicon dioxide chip.

### (iii) Single Micro Needle

Another alternative was to use a single micro needle as the movement restrictions encountered with two needles do not apply. This approach allowed a better picking and placing of nanowires, see Figures 2.11 (a) and (b). Unfortunately, it is a highly unstable random process where success requires nanowires to be balanced on the needle. Moreover, once a nanowire was successfully dropped onto the chip, it was necessary to use the needle to correctly place the deposited nanowire onto a nickel pad, as seen in Figures 2.11 (c) to (f).

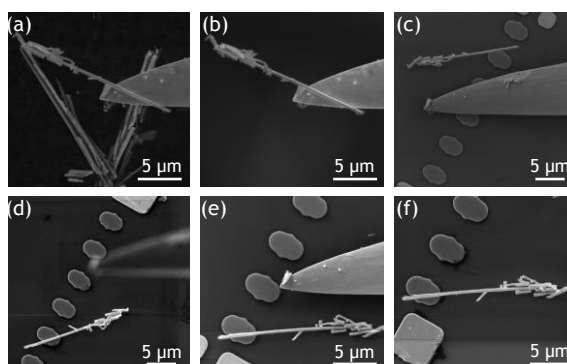


**Figure 2.11:** Scanning electron micrographs of (a) nanowire stuck on a micro needle, (b) nanowire released on a silicon/silicon dioxide chip, (c) to (e) use of the same micro needle to correctly place the deposited nanowire onto a nickel pad.

In the end not only were there issues due to the dominance of attractive forces over gravitational forces and difficulty in sample handling, but the robotic assembly technique requires trained people, is very time consuming and only a very few attempts were successful. Thus, unfortunately, the robotic assembly approach is not suitable for the assembly of the Pt/CoPt nanowires onto Si/SiO<sub>2</sub> chips comprising nickel receptors. Alternatively, several self-assembly procedures were explored.

### 2.3.5 Self-Assembly Approaches

#### (i) Flow Assembly

The first self-assembly trials consisted in slightly tilting Si/SiO<sub>2</sub> chips while allowing a stream of nanowires suspended in deionised water to flow either in parallel or perpendicular to the nickel pads, see Figure 2.12 (a), followed by drying the samples in the air for up to 3 hours or in the oven at 40 °C for about 20 minutes. A lint free tissue was placed under the chip to collect the residual flow of solution. This procedure required a large volume of solution and resulted in very little or no nanowires adhering onto the surface, thus it was abandoned.

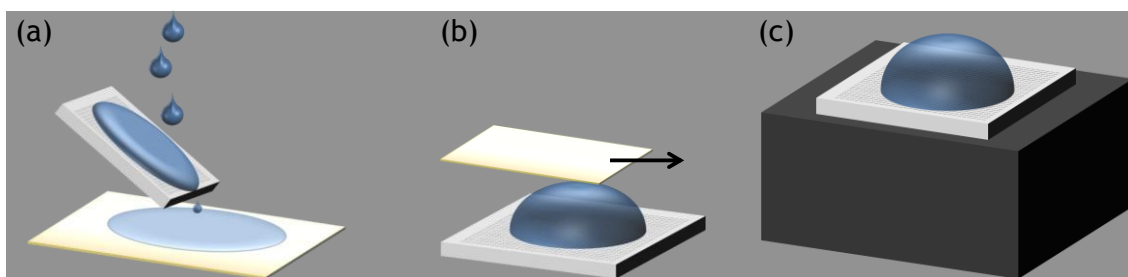


**Figure 2.12:** Schematic representations of self-assembly approaches: (a) flow assembly, (b) capillary assembly and (c) magnetic assembly.

#### (ii) Capillary Assembly

Another approach consisted in dropping 50-60  $\mu$ L of Pt/CoPt nanowires suspended in deionised water onto Si/SiO<sub>2</sub> chips that were lying horizontally on a clean surface, see Figure 2.12 (b). The suspended nanowires were allowed to settle for 10 minutes before the drop was carefully and effectively removed with a lint-free tissue. Alternatively, the drop was removed using a micropipette or a glass slide, or even allowed to dry for about 24 hours, but these were found to be ineffective techniques as nanowires were sticking together or little or no nanowires were sticking onto the chip. Following the drop removal, chips were either left to dry at room temperature for up to 3 hours or were dried in the oven at 40 °C for about 20 minutes. Drying in the oven was found to be more effective as it was faster and chips were less likely to be soiled by airborne contaminants. Optical analysis showed high yield of isolated Pt/CoPt nanowires that were attached by the tip onto nickel pads with little nanowires attached elsewhere on chips. All assembled nanowires were aligned in the same direction, but this direction changed from chip to chip, implying that the nanowire direction of alignment was governed by capillary forces. The “dropping/lint-free drop removal/oven drying” method was found to be an effective method. Analysis using the scanning electron

microscope with the backscattered detector was used to assess the statistical validity of the CoPt and nickel magnetic attraction, see Figures 2.13 (a) and (b). It was found that in about 58% of the cases (35 nanowires out of 60 samples), CoPt nanowire tips were stuck on nickel receptors.

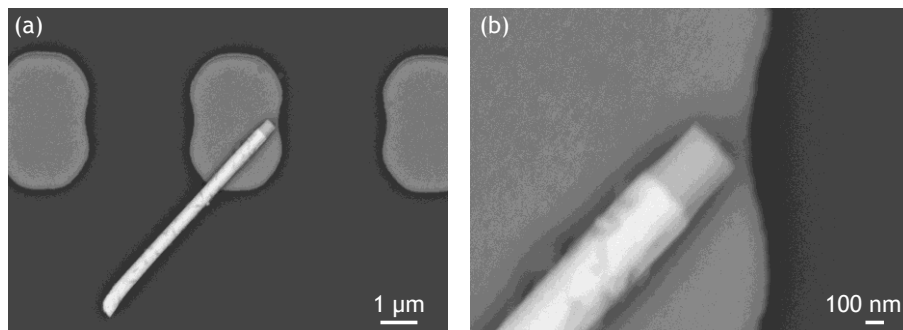


**Figure 2.13:** Scanning electron micrographs of (a) a single Pt/CoPt nanowire stuck on a nickel pad contained on a silicon/silicon dioxide chip and (b) at a higher magnification. A backscattered electron detector was used to distinguish the different materials.

### (iii) Magnetic Assembly

A vial containing uniformly suspended Pt/CoPt nanowires in water was placed adjacent to a neodymium (NdFeB, grade N52) cube magnet (product code BX0X0X0; K&J Magnetics, Inc.). NdFeB magnets are by far the strongest type of permanent magnet commercially available with a residual flux density up to 1.48 T. As can be seen in Figure 2.14 (a) and (b), the nanowires responded to the presence of the local magnetic field by accumulating in the region of the vial that was next to the magnet. Pristine CoPt nanowires that were treated in the same way also responded to the presence of the external applied field. Furthermore, pristine nanowires were also attracted toward the external magnetic field, thereby showing the paramagnetic property of platinum<sup>26</sup>. This demonstrates the magnetic feasibility of self-assembling Pt/CoPt nanowires by the application of an external magnetic field.

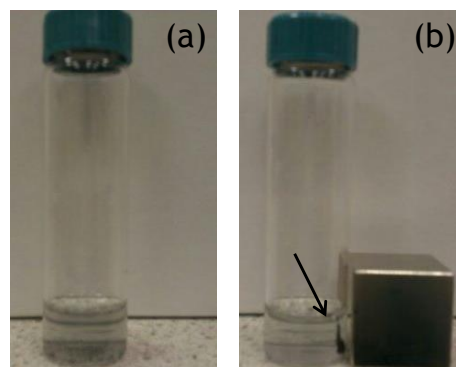


**Figure 2.14:** (a) and (b) Pictures showing the response of a suspension of Pt/CoPt nanowires suspended in water to an external magnetic field applied by a NdFeB cube magnet.

The “dropping/lint-free drop removal/oven drying” self-assembly approach was then repeated with Si/SiO<sub>2</sub> chips lying horizontally on a clean magnet surface, see Figure 2.12 (c). Chips were positioned onto the magnetic cube and care was taken to ensure chips were correctly aligned on it. Optical characterisation confirmed high yield of well isolated Pt/CoPt nanowires that were all stuck on nickel sites. All assembled nanowires were aligned in the same direction. Analysis using the scanning electron microscope with the backscattered detector showed no improvement in the percentage of CoPt nanowire tips adhering on nickel pads. This is probably due to the paramagnetic properties of platinum.

### 2.3.6 Pt/CoPt Nanowire Device Integration

Self-assembled Pt/CoPt nanowires were easily located on Si/SiO<sub>2</sub> chips thanks to the grid number and the binary alignment markers; see Figure 2.15 (a). This enabled accurate overlay of electrical contact electrodes using optical lithography, gold evaporation and lift-off techniques, see Figure 2.15 (b). However, in this example and like in most cases, the window in the passivation layer was not opened properly as it was often misaligned or too large.

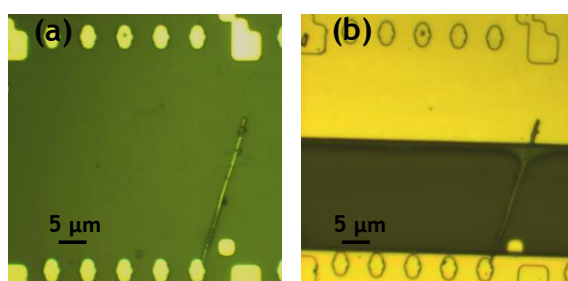


**Figure 2.15:** Optical micrographs at 100x magnification of (a) a well isolated ~30 μm long Pt/CoPt nanowire on a silicon/silicon dioxide chip and (b) the same Pt/CoPt nanowire electrically contacted by lithographic patterning, metal deposition and lift-off techniques, and passivated using resist. A 20 μm wide window (dark green) was opened in this layer to enable contact between the nanowire and electrolyte solution.

In other cases, the nanowires were contacted only on one side or broken or moved from the position they were initially attached or completely removed or there was a bunch of nanowires stuck together, as shown in Figures 2.16 (a) to (d). For instance, nanowires may not sustain the fact that photoresist was spun on at about 4000 rpm prior to metal evaporation, or may detach when the chips were transported. The yield of individually contacted nanowires was less than 20%; the majority of samples were discarded.

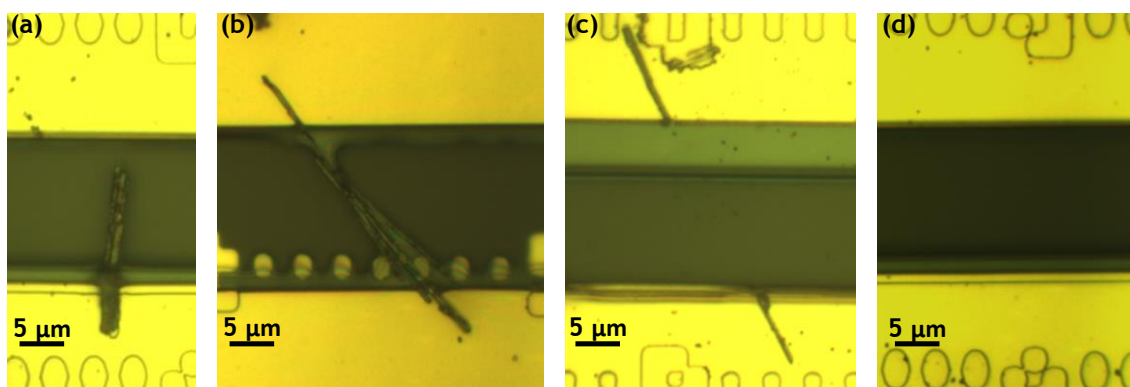


**Figure 2.16:** Optical micrographs at 100x magnification showing  $\sim 30 \mu\text{m}$  long Pt/CoPt nanowires on a silicon/silicon dioxide chip electrically contacted by lithographic patterning, metal deposition and lift-off techniques. (a) Nanowire is contacted on one side only, (b) a bunch of nanowires, (c) broken nanowire and (d) no nanowire. The opening in the resist layer (dark green) is misaligned in all cases.

This highlights the difficulty in integrating electrodeposited nanowires onto Si/SiO<sub>2</sub> chips. Moreover, samples were dirty as no cleaning procedure was used prior to the deposition of contact electrodes to avoid possible removal or damage of the self-assembled nanowires. In additional attempts, following nanowires assembly and localisation, chips were argon plasma cleaned for 30 seconds prior to contact electrodes deposition and the subsequent passivation step. This improved the yield of contacted nanowires to about 60%. However, the passivation layer was often misaligned or too large.

### 2.3.7 Electrical Characterisation of Pt/CoPt Nanowire Electrodes

To assess the functionality of the very few successful self-assembled and contacted Pt/CoPt nanowire devices, electrical characterisation using standard two point current-voltage measurements was performed in the voltage range of -10 mV to +10 mV. This low voltage range was employed in order to prevent potential damage occurring to a nanowire from electro-migration effects. The successfully contacted nanowire (depicted in Figure 2.15) exhibited very low resistance (227  $\Omega$ ), confirming good electrical contact by the overlaid gold interconnections, see Figure 2.17. Control electrical measurements were obtained in the absence of nanowires, yielding very high resistances ( $\sim 10 \text{ G}\Omega$ ) typical of an open circuit. This confirms that the underlying silicon oxide layer functioned as an effective insulating layer preventing electrical

coupling with the substrate beneath and that the observed electrical characteristics were exclusively generated by the contacted nanowire electrode.

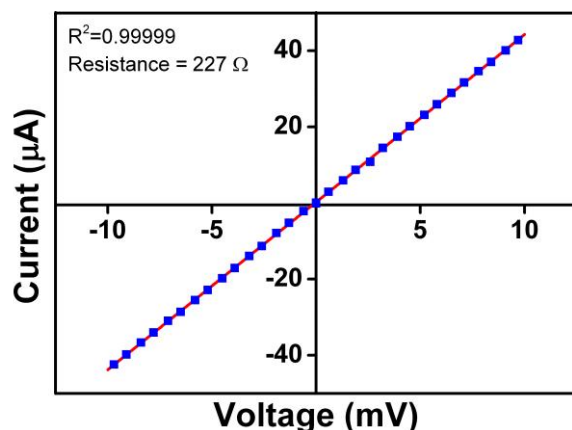


**Figure 2.17:** Two-point current-voltage characteristic measured for a fully integrated platinum/cobalt-platinum nanowire exhibiting ohmic behaviour and low resistance ( $227 \Omega$ ).

### 2.3.8 Electrochemical Characterisation

Prior to electrochemical experiments, contacted nanowires were cleaned by serial immersion for 10 minutes in acetone (bath 1), trichloroethylene, acetone (bath 2), isopropyl alcohol and deionised water, followed by drying in a stream of filtered nitrogen. In a faraday cage, chips were placed in the centre of a stage and a microscope was used to connect three probes to the electrodes, as shown in Figure 2.18 (a). The chip design overview is shown in Figure 2.18 (b); the platinum nanowire electrode is related to the two square pads on the left and a probe can be contacted to either of them for electrochemical measurements, the other two square pads are related to the gold counter and gold pseudo-reference electrodes. The three probes were then connected to a handheld potentiostat. Figures 2.18 (c) and (d) are high magnification optical images of a platinum nanowire working electrode.

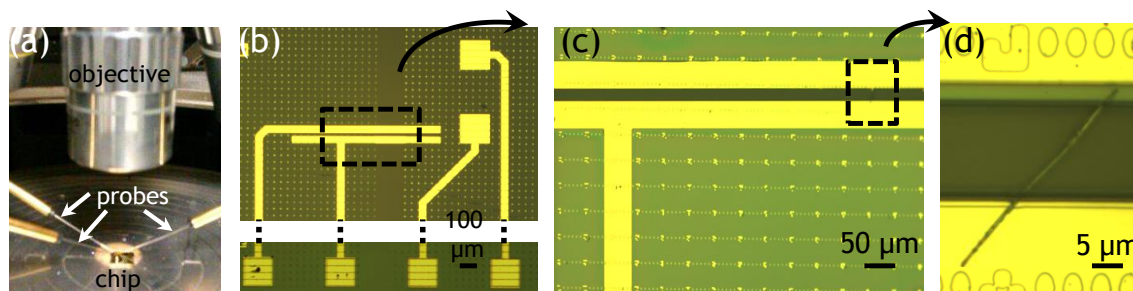


**Figure 2.18:** (a) Picture of the experimental set-up. (b) Optical micrographs at 2.5x magnification showing the chip design overview. (c) and (d) Optical micrographs respectively at 10x and 100 x magnification showing the platinum nanowire working electrode.

Two platinum nanowire electrodes were electrochemically characterised. Cyclic voltammograms acquired at these nanowire devices in 1 mM FcCOOH in 10 mM PBS at scan rates ranging from 5 to 100  $\text{mV}\cdot\text{s}^{-1}$  exhibited quasi-steady state behaviour. Due to the small critical dimension of the nanowires, mass transport is highly effective and becomes comparable to or larger than the rate of electron transfer from the FcCOOH to the electrode surface. As shown in Figure 2.19 (a) and (b), the magnitude of the measured current was on the order of  $\sim 12\text{-}20$  nA for one of them and  $\sim 7\text{-}10$  nA for the second one. This variation may be attributed to differences in nanowire dimensions as each nanowire electrodes were fabricated and integrated individually. Optical micrographs of the tested nanowire devices are shown in the inset of both figures, and respectively are the same as in Figures 2.15 and 2.18 (d). It is clear that for the first nanowire, the opening in the passivation layer also partially exposed binary markers and thus they may have also contributed to the measured signal, which could also explain the higher current measured.

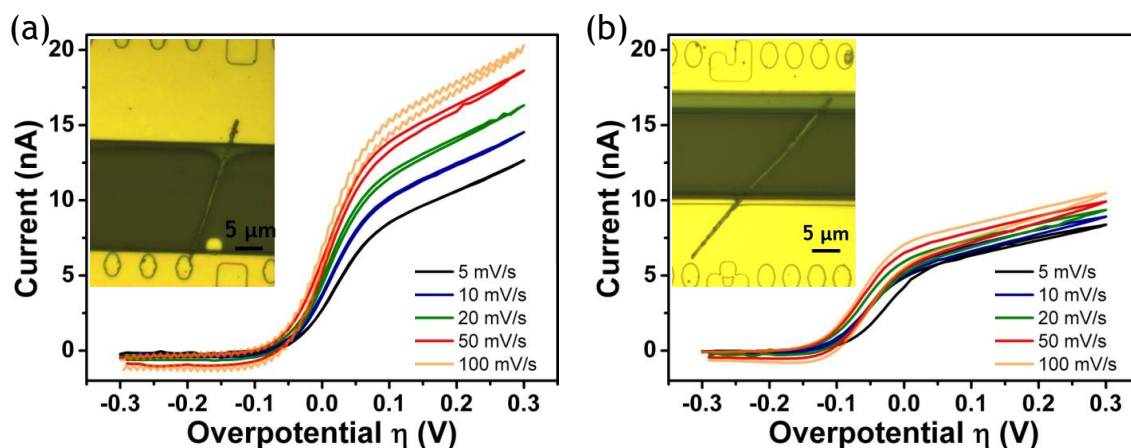


**Figure 2.19:** (a) Cyclic voltammograms obtained at a nanowire electrode in 1mM FcCOOH in PBS at 5, 10, 20, 50 and 100  $\text{mV}\ \text{s}^{-1}$ . Inset: optical micrograph at 100x magnification of the platinum nanowire working electrodes used.

The results obtained above are preliminary electrochemical measurements. While they show the potential of Pt/CoPt nanowire for electrochemical applications, further investigations are required. Misalignment of the opening in the passivation layer may have exposed binary markers which could have contributed to the measured signals. Work is now on-going to improve the alignment of the opening in the passivation window.

## 2.4 Summary and Conclusion

In this Chapter, a straight forward fabrication of high yields of uniform platinum nanowires with a cobalt-platinum tip by template electrodeposition is presented. Structural characterisation using a scanning electron microscope revealed that these nanowires have a diameter of about 340 nm. Their length can be controlled according to the deposition time; nanowires of length  $\sim 25\text{-}40\ \mu\text{m}$  for Pt and  $\sim 0.5\text{-}1\ \mu\text{m}$  for CoPt were typically fabricated. Energy dispersive X-ray spectroscopy and X-ray diffraction analysis confirmed the elemental composition.

Several robotic and self-assembly approaches at silicon/silicon dioxide chip substrates were investigated. Robotic assembly approaches were abandoned due to the inappropriate size and shape of the picking tools compared to the nanowires dimensions, and their limited mobility (movement control). Self-assembly experiments were proven more successful. Integration and packaging of these nanowires at silicon/silicon dioxide chip substrates for use as nanoelectrodes in electrochemical applications was very challenging, resulting in a poor yield. Assembled and integrated Pt/CoPt nanowires exhibited excellent electrical properties. Pt/CoPt nanowire devices exhibited quasi steady-state cyclic voltammograms in ferrocene monocarboxylic acid solution for scan rate up to  $100\ \text{mV s}^{-1}$ . However, further investigations are required as misalignment of the opening in the passivation layer may have exposed binary markers which could have contributed to the measured signals. Work is now on-going to address the misalignment issue. Upon optimisation of the fabrication procedure, it is expected that experimental errors will be reduced in order to permit the realisation of novel nanowire-based electrochemical devices.

## 2.5 References

1. Koehne, J. E.; Chen, H.; Cassell, A. M.; Ye, Q.; Han, J.; Meyyappan, M.; Li, J., Miniaturized multiplex label-free electronic chip for rapid nucleic acid analysis based on carbon nanotube nanoelectrode arrays. *Clinical chemistry* **2004**, 50, 1886-1893.
2. Arrigan, D. W., Nanoelectrodes, nanoelectrode arrays and their applications. *Analyst* **2004**, 129, 1157-1165.
3. Sablon, K., Nanoelectrodes for molecular devices: a controllable fabrication. *Nanoscale Research Letters* **2008**, 3, 268-270.
4. Conyers, J. L.; White, H. S., Electrochemical characterization of electrodes with submicrometer dimensions. *Analytical chemistry* **2000**, 72, 4441-4446.
5. Shao, Y.; Mirkin, M. V.; Fish, G.; Kokotov, S.; Palanker, D.; Lewis, A., Nanometer-sized electrochemical sensors. *Analytical Chemistry* **1997**, 69, 1627-1634.
6. Forrer, P.; Schlottig, F.; Siegenthaler, H.; Textor, M., Electrochemical preparation and surface properties of gold nanowire arrays formed by the template technique. *Journal of Applied Electrochemistry* **2000**, 30, 533-541.
7. Yang, M.; Qu, F.; Lu, Y.; He, Y.; Shen, G.; Yu, R., Platinum nanowire nanoelectrode array for the fabrication of biosensors. *Biomaterials* **2006**, 27, 5944-5950.
8. Keating, C. D.; Natan, M. J., Striped metal nanowires as building blocks and optical tags. *Adv. Mater.* **2003**, 15, 451-454.
9. He, X.; Antonelli, D., Recent advances in synthesis and applications of transition metal containing mesoporous molecular sieves. *Angewandte Chemie International Edition* **2002**, 41, 214-229.
10. Peters, R. D.; Yang, X. M.; Wang, Q.; de Pablo, J. J.; Nealey, P. F., Combining advanced lithographic techniques and self-assembly of thin films of diblock copolymers to produce templates for nanofabrication. *Journal of Vacuum Science & Technology B: Microelectronics and Nanometer Structures* **2000**, 18, 3530-3534.
11. Watt, F.; Bettiol, A.; Van Kan, J.; Teo, E.; Breese, M., Ion beam lithography and nanofabrication: a review. *International Journal of Nanoscience* **2005**, 4, 269-286.
12. Saedi, A.; Ghorbani, M., Electrodeposition of Ni-Fe-Co alloy nanowire in modified AAO template. *Materials Chemistry and Physics* **2005**, 91, 417-423.
13. Yin, A.; Li, J.; Jian, W.; Bennett, A.; Xu, J., Fabrication of highly ordered metallic nanowire arrays by electrodeposition. *Applied Physics Letters* **2001**, 79, 1039-1041.
14. Huczko, A., Template-based synthesis of nanomaterials. *Applied Physics A* **2000**, 70, 365-376.
15. Yin, Y.; Lu, Y.; Gates, B.; Xia, Y., Template-assisted self-assembly: a practical route to complex aggregates of monodispersed colloids with well-defined sizes, shapes, and structures. *Journal of the American Chemical Society* **2001**, 123, 8718-8729.

16. Hill, J. J.; Haller, K.; Gelfand, B.; Ziegler, K. J., Eliminating capillary coalescence of nanowire arrays with applied electric fields. *ACS applied materials & interfaces* **2010**, 2, 1992-1998.
17. Wang, Z.; Gao, R.; Poncharal, P.; De Heer, W.; Dai, Z.; Pan, Z., Mechanical and electrostatic properties of carbon nanotubes and nanowires. *Materials Science and Engineering: C* **2001**, 16, 3-10.
18. Rabinovich, Y. I.; Adler, J. J.; Esayanur, M. S.; Ata, A.; Singh, R. K.; Moudgil, B. M., Capillary forces between surfaces with nanoscale roughness. *Advances in colloid and interface science* **2002**, 96, 213-230.
19. Israelachvili, J.; Tabor, D., The measurement of van der Waals dispersion forces in the range 1.5 to 130 nm. *Proceedings of the Royal Society of London. A. Mathematical and Physical Sciences* **1972**, 331, 19-38.
20. Fearing, R. S. Survey of sticking effects for micro parts handling. In *Intelligent Robots and Systems 95. Human Robot Interaction and Cooperative Robots*, Proceedings. 1995 IEEE/RSJ International Conference on, 1995; IEEE: 1995; Vol. 2; pp 212-217.
21. Su, Y.-K.; Qin, D.-H.; Zhang, H.-L.; Li, H.; Li, H.-L., Microstructure and magnetic properties of bamboo-like CoPt/Pt multilayered nanowire arrays. *Chemical physics letters* **2004**, 388, 406-410.
22. Dahmane, Y.; Cagnon, L.; Voiron, J.; Pairis, S.; Bacia, M.; Ortega, L.; Benbrahim, N.; Kadri, A., Magnetic and structural properties of electrodeposited CoPt and FePt nanowires in nanoporous alumina templates. *Journal of Physics D: Applied Physics* **2006**, 39, 4523.
23. Marzi, G. D.; Iacopino, D.; Quinn, A. J.; Redmond, G., Probing intrinsic transport properties of single metal nanowires: Direct-write contact formation using a focused ion beam. *Journal of Applied Physics* **2004**, 96, 3458-3462.
24. Byrne, F. N.; Monzon, L.; Stamenov, P.; Venkatesan, M.; Coey, J., Influence of an Au capping layer on the magnetic properties of CoPt nanowires. *Applied Physics Letters* **2011**, 98, 252507-252507-3.
25. Xia, Y. N.; Yang, P. D.; Sun, Y. G.; Wu, Y. Y.; Mayers, B.; Gates, B.; Yin, Y. D.; Kim, F.; Yan, Y. Q., One-dimensional nanostructures: Synthesis, characterization, and applications. *Adv. Mater.* **2003**, 15, 353-389.
26. Rev, P. M., The Magnetic Properties of Platinum Metals and Alloys. *Platinum Metals Rev* **1964**, 8.

*Chapter 3*

**Electroanalysis at Ultra-micro and Nanoscale  
Electrodes: A Comparative Study**



### 3.1 Introduction

As described in the previous Chapters, metal nanowire electrodes represent a new and emerging powerful class of sensing elements<sup>1-3</sup>. Effectively, compared to ultra-microelectrodes, enhanced mass transport behaviour is expected to be achieved at a greater extent when employing nanoelectrodes, i.e., electrodes with a critical dimension in the 1-100 nm range or more precisely in the same order as the thickness of the diffusion layer forming during electrochemical measurements<sup>4-6</sup>. Although, metal nanowire electrodes have been applied to the detection of a variety of analytes, a key challenge is the lack of effective methodologies for the fabrication of robust, reproducible, well isolated, micrometre long nanowires that can be coupled with facile integration methods in order to be able to assess their electrochemical performance towards the preparation of functional sensing devices.

In the previous Chapter, we demonstrated a low-cost approach for the fabrication of ultra-long platinum nanowires by template electrodeposition, but their subsequent integration into a functional electrochemical sensor platform was very difficult. While the assembly and integration of electrodeposited nanowires was challenging, a very few successful attempts were achieved such that nanowires exhibited excellent electrical characteristics. However, only preliminary electrochemical measurements were achieved, but uncontrollable variations in the fabrication and integration processes resulted in variations from nanowire to nanowire. Thus, in order to benchmark and further understand nanowires electrochemical capabilities versus a commercial ultra-microelectrode, we selected electron-beam lithography as a comparative fabrication approach. This approach delivers on-chip nanowires with reproducible well defined geometries that are easily contactable with overlaid contact electrodes (using standard micron-scale photolithography techniques)<sup>7-10</sup>. Electron-beam lithography also permit the fabrication of multiple individual nanowire electrodes on a single chip and many chips can be prepared in parallel, thus enabling inter and intra chip comparison of the electrochemical properties of these electrodes to be undertaken<sup>11, 12</sup>.

In this Chapter, we fabricate discrete gold nanowires that employing electron-beam lithography, metal deposition and lift-off techniques at silicon substrates. Nanowire

electrodes dimensions were characterised using scanning electron microscopy, atomic force microscopy and optical microscopy. The electrical functionality of the nanowire devices was probed by standard two-point current voltage measurements. To directly compare these nanowire electrodes to state-of-the-art gold commercial ultra-microelectrodes (6.25  $\mu\text{m}$  in radius), the model redox mediator ferrocenemonocarboxylic acid was selected for electrochemical characterisation *via* cyclic voltammetry. Modified forms of the Cottrell equation were initially employed to estimate expected currents and these values compared against experimental results under steady-state conditions<sup>13-15</sup>. To explore the effects of varying analysis times on these electrodes, analyte diffusion profiles at ultra-microdisc and nanowire electrodes were simulated for a variety of scan rates (50, 500 and 5000  $\text{mV}\cdot\text{s}^{-1}$ ). To confirm our simulations, the corresponding experimental measurements using commercial gold ultra-microdisc electrodes and gold nanowire electrodes were undertaken. For nanowire electrodes, scan rates up to 20  $\text{V}\cdot\text{s}^{-1}$  were applied and recorded cyclic voltammograms maintained steady-state conditions. Therefore, significant enhancements in analysis times (up to 300 fold increase) were observed at nanowire electrodes; analysis time as low as 30-50 ms can be achieved compared to 10-15 s at ultra-microdisc electrodes for a given potential interval. Nanowire electrodes also exhibited a tenfold improvement in current densities when compared to ultra-microdisc electrodes. However, large charging currents were observed at nanowires due to the high electric fields associated with metal interconnection tracks, rather than from the nanowire itself.

---

This work has been published in full as ‘Electroanalysis at Ultra-micro and Nanoscale Electrodes: A Comparative Study’, *Journal of The Electrochemical Society*, **2013**

## 3.2 Experimental

### 3.2.1 Nanowire Electrode Design

As electron-beam lithography is a serial fabrication technique, fabrication of entire wafers of nanowire devices and associated micron-scale interconnection using electron-beam lithography would be very time consuming and cost prohibitive. In this regard, a hybrid process was chosen as a method of device fabrication, whereby only the nanowire structures were defined by electron-beam lithography and photolithography was employed to fabricate overlaid interconnection tracks. Electron-beam fields dimensions were selected so as to be maximum  $80\ \mu\text{m} \times 80\ \mu\text{m}$  to avoid problems with non-uniformity and stitching effects during electron-beam lithography patterning. Figure 3.1 shows the design of a single nanowire contained per die with a nominal width of 100 nm. Nanowire electrodes were designed with micron scale termini to facilitate good overlap and electrical connection to the overlaid interconnection tracks. The entire layout of electrically contacted nanowire electrodes, complete with interconnection tracks and bond pads, is displayed in Figure 3.2 (a) and (b).

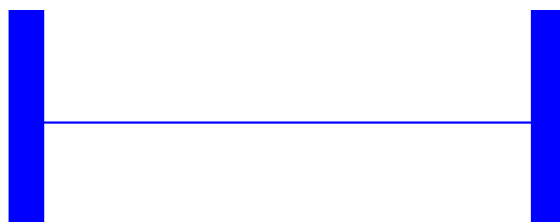
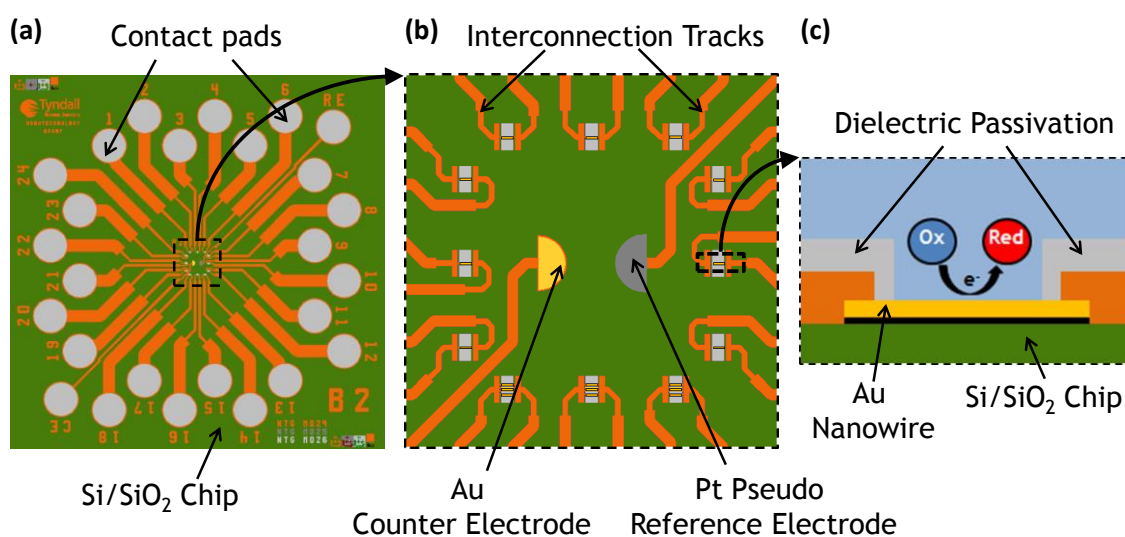


**Figure 3.1:** Schematic representations of a 100 nm wide nanowire electrode comprising micron scale termini to facilitate good overlap and electrical connection with overlaid interconnection tracks (not to scale).

### 3.2.2 Nanowire Fabrication

Gold nanowire electrodes were fabricated using a hybrid electron-beam/photolithography process on four inch wafer silicon substrates bearing a  $\sim 300\ \text{nm}$  layer of thermally grown silicon dioxide ( $\text{Si}/\text{SiO}_2$ ). In this approach, nanowires and alignment marks were patterned in resist (ZEP 520 Nippon Zeon) by direct electron beam writing (JBX-6000FS, JEOL UK Ltd., optimised parameters: beam voltage 50k V, beam current 100 pA and beam dose  $120\ \mu\text{C}\cdot\text{cm}^{-2}$ ). Following resist development, gold layers (Ti/Au 5/50 nm) were blanket deposited by metal evaporation (Temescal FC-2000 E-beam evaporator) and removed from un-patterned areas using standard lift-

off techniques to yield stacked metallic (Ti/Au) nanowire structures. Using the electron beam written alignment marks, interconnection tracks were then overlaid onto nanowires termini by photolithography, metal evaporation (Ti/Au 10/90 nm) and lift-off techniques. Two central half-disk gold electrodes ( $\sim 1.6 \times 10^{-4} \text{ cm}^2$ ) and peripheral round electrical contact pads ( $\sim 1.5 \text{ mm}$  in diameter) were also deposited as part of this optical lithography step. A further metal deposition (Ti/Pt 10/90 nm) step was then performed onto one half-disk electrode. In this manner, the central half-disk electrodes may be employed as gold counter and platinum pseudo-reference electrodes, respectively.



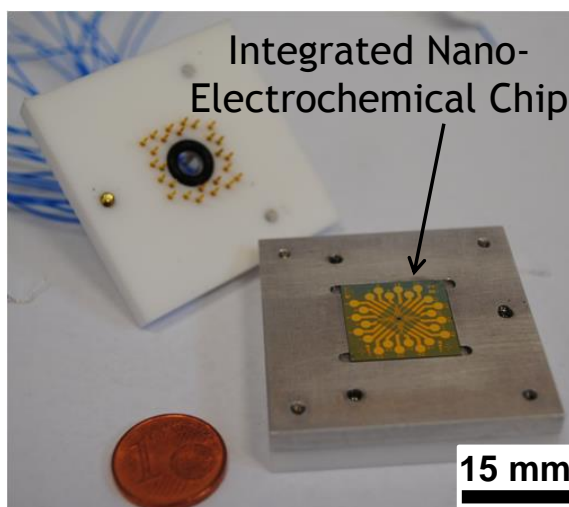
**Figure 3.2:** (a) Schematic representation of the chip design for the novel nanowire based nano-electrochemical chip comprising of micron scale interconnection tracks connecting peripheral probe contact pads, with nanowire, counter and reference electrodes located in the chip centre. Chips are insulated with a silicon nitride passivation layer. (b) A plan view of the central chip region containing twelve individually addressable nanowire working electrodes, a gold on-chip counter electrode and a platinum on-chip pseudo-reference electrode. (c) A cross-sectional representation of an interconnected nanowire electrode on a Si/SiO<sub>2</sub> chip, micron scale interconnection tracks and passivation overlayer. An opening in the passivation layer directly over the nanowire permits electrochemical interactions occur exclusively at the nanowire.

Figure 3.2 (a) is a schematic representation overview of the chip design. To prevent unwanted electrochemical reactions occurring between metal interconnection tracks and electrochemically active species, a silicon nitride passivation layer ( $\sim 500 \text{ nm}$  thick) was then deposited by plasma-enhanced chemical vapour deposition onto the wafer surface. Photolithography and dry etching were then employed to selectively open windows ( $\sim 45 \times 100 \mu\text{m}$ ) in the passivation layer directly above the gold nanowire working electrodes to allow exclusive contact between them and an electrolytic solution.

Openings were also maintained above the counter and reference electrodes along with peripheral contact pads. Following fabrication, wafers were diced into 16 x 16 mm chips. Each chip contained twelve individually contacted gold nanowire working electrodes, an integrated gold counter electrode and a platinum pseudo-reference electrode, as seen in the schematic representation in Figure 3.2 (b). Openings in the passivation layer directly over nanowires permits electrochemical interactions to occur exclusively at the nanowire as seen in Figure 3.2 (c).

### 3.2.3 Nanowire Electrochemical Cell Set-up

To allow both single and multiplexed electrochemical analysis, and to complete device packaging, chips were assembled onto a home-built cell with a sample volume of about 150  $\mu\text{L}$ , comprising spring loaded probes to electrically contact the working, counter and reference electrodes to the potentiostat through the on-chip peripheral pads. The cell is made of two parts, see Figure 3.3.



**Figure 3.3:** Image of a fully fabricated chip mounted into the bottom aluminium tray of the home-built cell. The upper part of the cell is pictured in the top left of the image, showing the spring loaded probes utilised to make electrical connection to the round peripheral contact pads on the chip.

The bottom part consists of an aluminium tray with a central square recessed and designed so as to be only  $\sim 0.1$  mm larger than the chip dimensions to ensure that the chip would sit into and remain securely placed during measurements. The top part is a polytetrafluoroethylene cap comprising apertures to mount spring loaded probes (Series S Duraseal: S-00-J-1.3-G-DS-36-1, Connector Solutions Ltd., U.K) and a sample

reservoir. When fully constructed, a chip is contained between the bottom and top parts, which are held together using three screws. The sample reservoir is made water-tight using an O-Ring (James Walker Ltd.). The inner diameter of the O-ring was ~4.5 mm, large enough to ensure that all electrodes on the chip had equivalent access to the analyte without impeding diffusion processes. The original cell was designed by Dr. Nicolas Sassiati (Nanotechnology Group, Tyndall National Institute) and was modified to incorporate extra electrical contact sites.

### 3.2.4 Nanowire Structural and Electrical Characterisation

As before, structural characterisation was undertaken using a calibrated microscope (Axioskop II, Carl Zeiss Ltd.) equipped with a charge-coupled detector camera (CCD; DEI-750, Optronics), and a scanning electron microscope (JSM-6700F, JEOL UK Ltd.) operating at beam voltages between 5 and 10 kV, and electrical characterisation was performed using a probe station (Model 6200, Micromanipulator Probe Station) in combination with a source meter (Keithley 2400) using a dedicated programmed using LabVIEW™ V8.0 program. For these current-voltage measurements, the source electrode was grounded, a bias sweep up to  $\pm 10$  mV was applied to the drain electrode, and the current through the nanowire was measured, as previously described. The topography of fabricated nanowires on Si/SiO<sub>2</sub> chips was investigated using a calibrated atomic force microscope (Dimension 3100, Veeco Instruments Inc.) in tapping mode with commercial tapping mode probes (MP-11100, Veeco Instruments Inc; typical radius of curvature ~ 10 nm and front/side cone angles of 15°/ 17.5°, respectively).

### 3.2.5 Electroanalysis at Nanowire Electrodes

All electrochemical studies were performed using a CHI660A Electrochemical Analyser and Faraday Cage CHI200B (CH Instruments). All experiments were carried out in a three-electrode cell configuration using gold single nanowire working electrodes with on-chip gold counter and on-chip platinum pseudo reference electrodes. All electrochemical measurements were conducted in a home-made cell, with a typical sample volume of about 150  $\mu$ L. Prior to electrochemical experiments, electrodes were cleaned by sequential immersion of chips for 10 minutes in acetone (bath 1),

trichloroethylene, acetone (bath 2), and iso-propyl alcohol, followed by a thorough rinse with deionised water and dried in a stream of filtered nitrogen. Cyclic voltammetry was undertaken in the voltage range of -0.15 to 0.45 V for a variety of scan rates (20 to 20,000  $\text{mV}\cdot\text{s}^{-1}$ ) in 1 mM ferrocene monocarboxylic acid in 10 mM phosphate buffered saline solutions at pH 7.4. Solutions were deaerated with nitrogen gas prior to electrochemical analysis.

### 3.2.6 Electroanalysis at Ultra-microdisc Electrodes

As for nanowire electrodes, all electrochemical studies were performed using a CHI660A Electrochemical Analyser and Faraday Cage CHI200B (CH Instruments). All experiments were carried out in a three-electrode cell configuration employing gold ultra-microdisc working electrodes of radius 6.25  $\mu\text{m}$ , a platinum wire counter electrode and a saturated silver/silver chloride electrode (Ag/AgCl, sat KCl) reference electrode (CH Instruments). All electrochemical measurements were conducted in a beaker with a sample volume of about 20 mL. A home-made polytetrafluoroethylene cap comprising three openings was used to hold the electrodes appropriately in place. Cyclic voltammetry was undertaken in the voltage range of 0 to 0.6 V for a variety of scan rates (20 to 5,000  $\text{mV}\cdot\text{s}^{-1}$ ) in 1 mM ferrocene monocarboxylic acid in 10 mM phosphate buffered saline solutions at pH 7.4 and deaerated with nitrogen gas prior to electrochemical analysis. Before each experiment, gold ultra-microdisc electrode surfaces were polished for two by ten minute intervals with alumina powder (first with 3  $\mu\text{m}$  then with 1  $\mu\text{m}$ ) in water suspension on Microcloth polishing pads. Between these two polishing steps and prior to being placed in the cell, electrodes were washed with deionised water. Prior to use, platinum counter electrodes were cleaned by fully immersing the wire in concentrated nitric acid for 1 to 2 hours, and thoroughly rinsed with deionised water afterwards. The reference electrodes consisted of an AgCl coated silver wire immersed in a glass capillary containing a saturated solution of silver chloride and potassium chloride (AgCl/KCl) with a permeable frit at the bottom. The saturated AgCl/KCl solution level in the reference electrode capillary was regularly monitored and topped up from a stock solution when needed, so that its level did not drop below the level of the wire. When not in use, Ag/AgCl sat. KCl electrodes were stored in ~4.5 M KCl solution at room temperature, in the dark. The open circuit potential (OCP) was also measured prior to measurements to ensure the reference

electrode was operating correctly; the electrode was replaced or reconditioned when the OCP was  $\geq 5$  mV.

### 3.2.7 Finite-Element Simulation

Analyte concentration profiles for the oxidation of a redox molecule at single ultra-microdisc and single nanowire electrodes were simulated using the ‘transport of diluted species’ modelling platform in the ‘chemical species transport’ module comprised in the commercial finite element software package Comsol Multiphysics® 4.1. (Comsol, SE). These simulations were based on the single electron oxidation process of ferrocene monocarboxylic acid in solution at the surface of an electrode of interest, corresponding to:



Simulations focused on assessing the effect of electrodes dimension on diffusional mass transport of an analyte during a potential sweep technique, such as cyclic voltammetry, with respect to the applied scan rate. As electrochemical experiments were undertaken in presence of excess supporting electrolyte, in static un-agitated environments, at constant temperature and over short time periods, mass transport effects arising from migration and convection were assumed to be negligible. Thus emphasis was placed on diffusional mass transport alone, and only Fick’s second law of diffusion in two dimensions was considered<sup>16, 17</sup>:

$$\frac{\partial C_i}{\partial t} = D_i \left( \frac{\partial^2 C_i}{\partial x^2} + \frac{\partial^2 C_i}{\partial y^2} \right) \quad [3.2]$$

where  $C_i$  and  $D_i$  represent the concentration and diffusion coefficient of the redox species in solution, respectively. In these models, the redox analyte concentration was 1 mM ferrocene monocarboxylic acid (FcCOOH) in 10 mM phosphate buffered saline solutions; its associated diffusion coefficient was determined experimentally, see subsection 3.3.3. Assuming a simple reversible charge transfer process, in equation 3.1, where both species O and R are present in solution, the relative diffusion coefficients may have slight variances but for simulation purposes they were assumed to have equal values, *i.e.* ( $D_O = D_R$ ). The concentration of FcCOOH (species R) at an electrode of interest for a given time interval using a potential sweep method may be expressed by the following Nernstian boundary conditions<sup>16, 18</sup>:

$$\text{at } t = 0: C_R(t) = C_R^* \quad [3.3]$$

$$\text{at } t > 0: C_R(t) = \frac{C_R^*}{1 + \exp\left[\frac{nF}{RT}(E^0 - E(t))\right]} \quad [3.4]$$

where  $t$  is time (s),  $C_R^*$  and  $C_R(t)$  are concentration ( $\text{mol.m}^{-3}$ ) of the reductant species R in the bulk and at the electrode surface with respect to time, respectively,  $n$  is the number of electrons exchanged,  $F$  is Faraday's constant,  $R$  is the gas constant,  $T$  is temperature (K),  $E^0$  is the formal potential of the redox couple (V).  $E(t)$  is the applied forward potential in V defined as:

$$E(t) = E_{\text{int}} + vt \quad [3.5]$$

where  $E_{\text{int}}$  is the initial voltage (V) of the potential sweep,  $v$  is the scan rate ( $\text{V.s}^{-1}$ ),  $t$  is time (s). From experimental results, values of 0.317 V (vs Ag/AgCl, sat KCl) and 0.155 V (vs Pt) were used for  $E^0$  at an ultra-microdisc and at a nanowire, respectively. Simulations were carried out in a potential window from 0 to 0.6 V (vs Ag/AgCl, sat KCl) at an ultra-microdisc and -0.15 to 0.45 V (vs Pt) at a nanowire for scan rates of 50, 500 and 5000  $\text{mV.s}^{-1}$ . Models were built using a simplified two dimensional model known as the diffusion domain approach, consisting of a representative cross sectional plane through an electrode. To ensure accuracy of the simulations, the domain area was selected so as to be large enough to ensure bulk-like conditions at the boundaries remain unaffected by the electrochemistry occurring at the electrodes. Simulations were allowed to iteratively resolve until a convergence error less than 2% was achieved. Simulations were carried out to provide a better insight of the mass transport behaviour.

### 3.2.8 Chemicals and Glassware

Unless otherwise stated, all chemicals were purchased from Sigma-Aldrich and were used as received. All solutions were freshly prepared on a weekly basis with deionised water of resistivity 18.2  $\text{M}\Omega.\text{cm}$  (Millipore Q).

### 3.3 Results and Discussion

#### 3.3.1 Electrodes Structural Characterisation

Figure 3.4 (a) shows a commercial gold ultra-microdisc electrode. With a declared radius of approximately  $6.25\ \mu\text{m}$ , the active surface area available for electrochemical analysis was estimated to be about  $1.23 \times 10^{-6}\ \text{cm}^2$ .

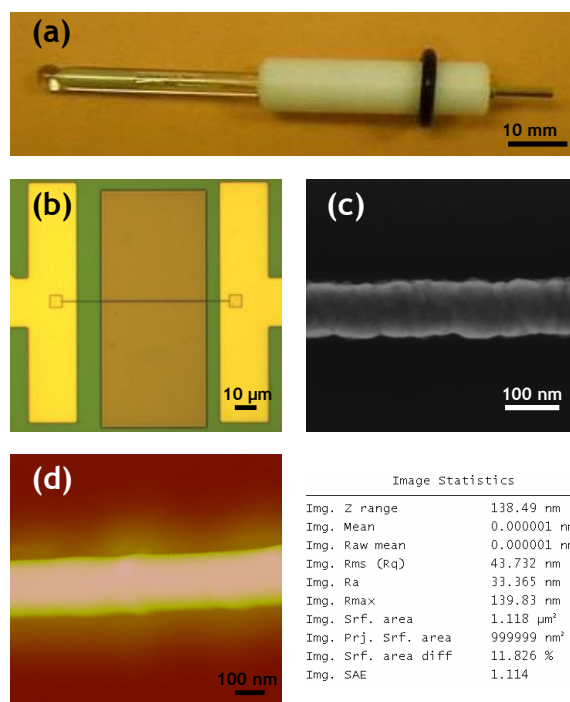


**Figure 3.4:** (a) Picture of a commercial  $6.25\ \mu\text{m}$  radius gold ultra-microdisc electrode. (b) Optical micrograph of a fully integrated and passivated nanowire. The darker rectangle in the middle corresponds to the trench selectively opened in the photoresist directly above the nanowire to allow contact with an electrolyte solution. (c) Scanning electron micrograph of a portion of an exposed protruding nanowire. (d) Typical atomic force micrograph of a single nanowire with surface area data included.

Nanowires were fabricated using a hybrid electron-beam lithography and photolithography process at silicon/silicon dioxide wafer substrates, see experimental subsection 3.2.2. Following their fabrication, nanowire electrodes were structurally characterised using a combination of optical, scanning electron and atomic force microscopies. Figure 3.4 (b) shows an optical micrograph of a fully fabricated and electrically contacted single nanowire electrode. The nanowires were passivated with an insulating silicon nitride overlayer to prevent unwanted electrochemical reactions occurring between metal interconnection tracks and electrochemically active species. To allow direct contact only between a nanowire and electrolytic solution, a window

(central dark rectangle in the optical micrograph) was selectively opened in the passivation layer, directly above the nanowire electrodes. The width of the window defined the exposed electrode length, typically  $\sim 45 \mu\text{m}$ . The gold square at the electrodes termini were defined during the first metallisation step in order to ensure good contact with overlaid interconnection tracks. Visual inspection using scanning electron microscopy clearly showed that the silicon nitride layer was fully removed from the entire target window region, see Figure 3.4 (c). Excellent alignment of the electron-beam lithography and optical patterned layers was observed in all cases, thus suggesting that nanowires are well electrically contacted. A statistical analysis using scanning electron micrographs at multiple locations across different individual nanowires ( $n = 340$ ) yielded average width of  $98 \pm 5 \text{ nm}$ , as previously reported<sup>19</sup> (within experimental error), indicating the high reproducibility of the fabrication process and confirmed that proximity effects did not arise during the electron beam lithography process and consequently nanowire broadening did not occur. Furthermore, following the selective removal of the silicon nitride overlayer, topographical analysis was also undertaken by Dr Karen Dawson (Nanotechnology Group, Tyndall National Institute) using atomic force microscopy, confirming that no residual silicon nitride remained on the nanowire surface, see Figure 3.4 (d). Nanowire heights were observed to be typically  $50.6 \pm 0.8 \text{ nm}$  and the roughness factor,  $\rho$ , was determined to be  $1.5 \pm 0.2$ . This yielded a calculated nanowire geometric active surface area of  $9 \times 10^{-8} \text{ cm}^2$  and an average actual surface area of  $\sim 1.35 \times 10^{-7} \text{ cm}^2$  available for electrochemical analysis.

### 3.3.2 Nanowire Electrical Characterisation

Standard two-point current-voltage measurements in air were undertaken as a quality control check to ensure that all nanowire electrodes were fully functional prior to electroanalysis. This was performed by contacting the two contact pads related to a nanowire device to two individual measuring probes. A voltage bias of  $\pm 10 \text{ mV}$  was selected to avoid undesired electro-migration effects which may damage the electrodes. All functioning devices display ohmic linear and very reproducible responses confirming excellent registration between the nanowires and the overlaid micron-scale interconnection tracks, see Figure 3.5. Fully packaged nanowires across multiple chips exhibited low resistance ( $1442 \pm 184 \Omega$ ,  $n = 31$ ) as shown in the inset of Figure 3.4.

Control electrical measurements were obtained in the absence of electrodes, yielding very high resistances ( $\sim 10\text{ G}\Omega$ ) typical of an open circuit. This confirms that the underlying silicon oxide layer functioned as an effective insulating layer preventing electrical coupling with the substrate beneath and that the observed electrical characteristics were exclusively generated by the nanowire electrodes and associated on-chip metal interconnection tracks. Devices that exhibit high resistances or open circuit behaviour were discarded.

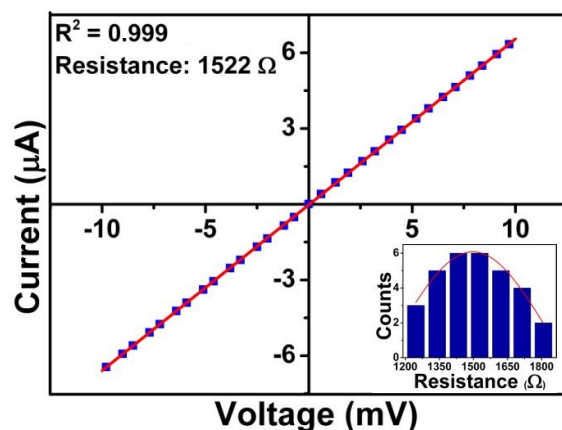


**Figure 3.5:** Typical ohmic response observed for a two-point current-voltage measurement obtained from a fully integrated and packaged nanowire electrode, with a resistance of  $1522\ \Omega$ . Inset: distribution of resistances measured for several packaged single nanowire electrodes; red line is a Gaussian fit to the data.

Functioning gold nanowires fabricated by electron-beam lithography exhibited higher resistances than platinum nanowires fabricated in Chapter 2 using the template electrodeposition fabrication technique. This may be principally attributed to the smaller cross-sectional area of the gold nanowires ( $100\text{ nm} \times 50\text{ nm}$ ) compared to the platinum nanowires ( $340\text{ nm}$  in diameter).

### 3.3.3 Experimental Estimation of the Diffusion Coefficient

#### *Cyclic Voltammetry*

As discussed in the introduction Chapter (subsection 1.2.2), cyclic voltammograms are typically peak-shaped at macro and micro electrodes, and peak currents follow the Randles-Sevcik relationship (see equation 1.36), which can be used for the determination of diffusion coefficients. Therefore, to determine the diffusion coefficient associated with  $1\text{ mM}$  ferrocene monocarboxylic acid in  $10\text{ mM}$  phosphate

buffer saline solution, cyclic voltammograms were recorded at single commercial gold macrodisc electrodes (1 mm in radius). Before each experiment, the electrode surfaces were polished for 2 by ten minute intervals with alumina-water slurries (first with 3  $\mu\text{m}$  then with 1  $\mu\text{m}$ ) on Microcloth polishing pads. Between these two polishing steps and prior to being placed in the cell, the electrode was thoroughly rinsed with deionised water. Subsequent cyclic voltammetry experiments were conducted in 0.1 M sulphuric acid in the potential range -0.2 to 1.6 V (vs. Ag/AgCl, sat KCl) at a scan rate of 100  $\text{mV}\cdot\text{s}^{-1}$ . Characteristic gold oxide formation and reduction peaks confirmed electrode functionality, while reproducible reduction peaks current achieved within a few successive cycles indicated that the electrode was clean (see appendix A.2). Following electrode cleaning, cyclic voltammograms in 1 mM FcCOOH in 10 mM PBS were conducted in the potential window of 0.0 to 0.6 V (vs. Ag/AgCl, sat KCl) at scan rates ranging from 5 to 5000  $\text{mV}\cdot\text{s}^{-1}$ , see Figure 3.6. These measurements were repeated in triplicate. It was found that the peak currents increased linearly with the square root of increasing scan rates as depicted in the inset of Figure 3.6. From this linear relationship and equation 1.36, we obtained an average diffusion coefficient of  $5.4 \times 10^{-6} \text{ cm}^2\cdot\text{s}^{-1}$  for  $C^* = 1.03 \times 10^{-6} \text{ mol}\cdot\text{cm}^{-3}$  and  $A = 3.14 \times 10^{-2} \text{ cm}^2$  (geometric area). This coefficient was used in all simulations and theoretical estimations involving 1 mM FcCOOH in 10 mM PBS solution. Although we did not thermostat our experiments, the temperature in the laboratory is controlled. At the time we undertook the measurements, the temperature was around  $20 \text{ }^\circ\text{C} \pm 2 \text{ }^\circ\text{C}$ .

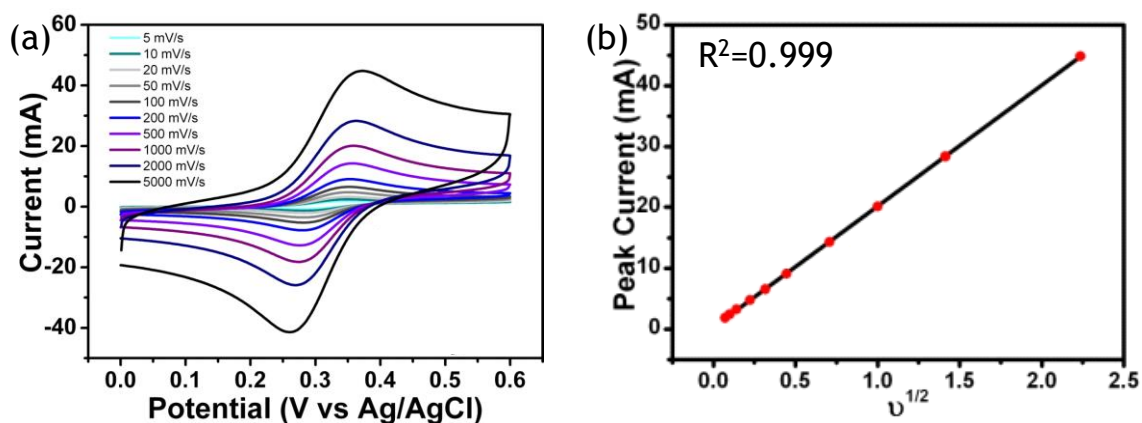


**Figure 3.6:** (a) Typical cyclic voltammograms in 1 mM FcCOOH in 10 mM PBS at scan rates ranging from 5 to 5000  $\text{mV}\cdot\text{s}^{-1}$  measured at a 1 mm radius gold macrodisc electrode. (b) Linear relationship between the peak current and the square root of scan rate.

### Chronoamperometry

Alternatively, the diffusion coefficient was estimated using chronoamperometry at gold microdisc electrode (6.25  $\mu\text{m}$  in radius) immersed in a 1 mM FcCOOH in 10 mM PBS solution. The potential and time parameters were set as follows:  $E_1 = 0$  V,  $E_2 = 0.6$  V and  $E_3 = 0$  V (all vs Ag/AgCl, sat KCl),  $t_1 = t_2 = 10$  s with a sampling interval of 10 ms. The potential were chosen so that there is no redox reaction occurring at  $E_1$ , then FcCOOH is oxidised at  $E_2$  such that its concentration drops nearly to zero at the electrode surface (diffusion controlled oxidation), and then this process is reversed when the potential is jumped back to  $E_1$  (diffusion controlled reduction);  $E_2$  is chosen so that it is greater than the standard potential  $E^{0'}$  of FcCOOH redox couple. Chronoamperometry measurements were repeated three times. Before each experiment, the ultra-microdisc electrode was cleaned as described in subsection 3.2.6.

Under steady-state condition, the current at an ultra-microdisc electrode can be defined by the equation<sup>20</sup>:

$$i_{ss(\text{ultra-microdisc})} = 4nFD_R C_R^* r \quad [3.6]$$

where  $i_{ss(\text{ultra-microdisc})}$  is the steady-state current (A),  $n$  is the number of electrons in the reaction,  $D_R$  is the diffusion coefficient of 1 mM FcCOOH in 10 mM PBS,  $C_R^*$  is the bulk concentration of FcCOOH, and  $r$  is the radius of the ultra-microdisc electrode. Furthermore, the diffusion limiting current at an ultra-microdisc electrode can be described by the equation<sup>20</sup>:

$$i(t) = \frac{\pi^{1/2} n F D^{1/2} C_R^* r^2}{t^{1/2}} + 4nD_R C_R^* r \quad [3.7]$$

where  $t$  is time (s) and all other parameters take their usual definition. By normalising this equation with respect to the steady-state current, we obtain:

$$\frac{i(t)}{i_{ss(\text{ultra-microdisc})}} = \frac{\pi^{1/2}}{4(D_R t)^{1/2}} r + 1 \quad [3.8]$$

According to equation 3.8, it is clear that the ratio of the measured current over steady-state current is proportional to the inverse of square root of time. This linear relationship is characterised by its intercept  $A$  and its slope  $S$ :

$$S = \frac{\pi^{1/2}}{4D_R^{1/2}} r \quad [3.9]$$

The diffusion coefficient can then be deduced from the ratio of the intercept and the slope, which rearranged yields:

$$D_R = \frac{\pi r^2 A^2}{16S^2} \quad [3.10]$$

All the above equations are valid for diffusion-only condition and thus may not apply for the entire experimental time span. At the start of a chronoamperometry measurement (very short time region), convection perturbation is usually negligible at an ultra-microdisc electrode but errors in the measured current may arise from contributions from double layer charging currents. Towards the end of a chronoamperogram (long time region), convection may influence the signal. Therefore, data points from the short and long time regions of a chronoamperogram may be omitted and only points from the intermediate region may be considered for linear fitting purpose.

A typical chronoamperogram recorded at an ultra-microdisc electrode of radius  $6.25\ \mu\text{m}$  is shown in Figure 3.7 (a), with a steady-state of  $1.31 \pm 0.09\ \text{nA}$ . The experimental current was normalised with respect to the experimental steady-state current and plotted against the inverse of the square root of time; only data points corresponding to the intermediate region have been plotted to avoid errors related to double layer charging currents and convection contributions. As seen in Figure 3.7 (b), a linear relationship was obtained. From the expressions of obtained lines and equation 3.10, an average diffusion coefficient of approximately  $4.8 \times 10^{-6}\ \text{cm}^2$  was deduced, which is in reasonable agreement with the value obtained previously using cyclic voltammetry.

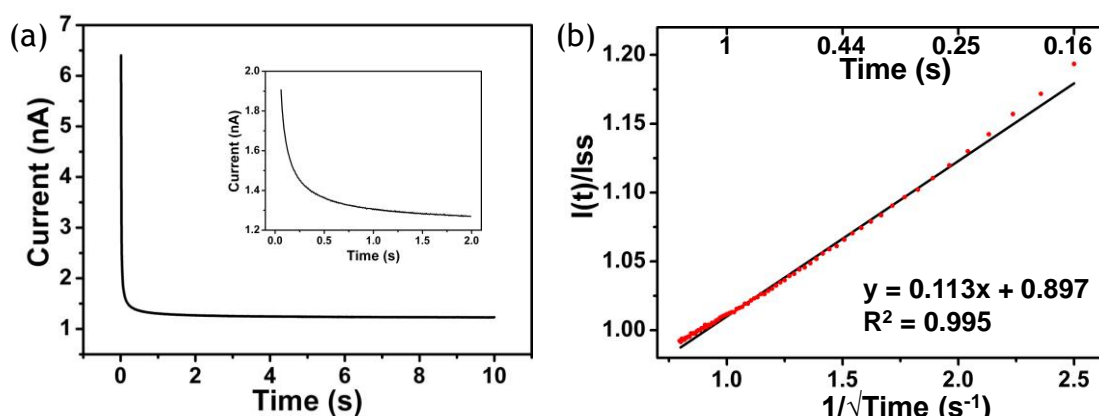


**Figure 3.7:** (a) Typical chronoamperogram in 1 mM FcCOOH in 10 mM PBS measured at a  $6.25\ \mu\text{m}$  radius gold ultra-microdisc electrode. (b) Linear relationship between the current normalised with the respect to the steady-state current and the inverse square root of time for an intermediate time region.

### 3.3.4 Electrochemical Signal Enhancement at the Nanoscale

During a potential sweep experiment such as cyclic voltammetry, oxidation (or reduction) of ferrocene monocarboxylic acid at an electrode surface generates a concentration gradient resulting in diffusional mass transport around the electrode surface. As mentioned in section 1.2.2, at an ultra-microdisc electrode, for long analysis time scales (low to medium scan rates, i.e.,  $\leq 100 \text{ mV}\cdot\text{s}^{-1}$ ), the cyclic voltammograms corresponding to the involved electron transfer process are expected to be sigmoidal, reaching a time-independent steady-state current value that can be theoretically obtained using equation 3.6. This yields a theoretical value of 1.30 nA, which normalised to the ultra-microdisc area is equal to  $\sim 11 \text{ A}\cdot\text{m}^{-2}$ . For short analysis time scales (medium to fast scan rates, i.e.,  $> 100 \text{ mV}\cdot\text{s}^{-1}$ ), the shape of the voltammograms are however expected to change from a sigmoidal to peak shaped, see equation 3.7. This arises from a change in the diffusional mass transport to the ultra-microdisc electrode with respect to the analysis time scale due to the critical dimension of the ultra-microdisc electrode being larger than the formed diffusion layer.

By contrast, at a nanowire electrode, cyclic voltammograms should be sigmoidal and reaching steady-state currents, even at fast scan rates, as the diffusional mass transport is assumed to be highly effective thanks to the very small critical dimensions of the nanowires. However, at present, there is no agreed analytical equation to determine the expected steady-state currents at a nanowire, since these electrodes have a three dimensional geometry and sharp edges. For this reason, analytical solutions based on similar geometries such as hemicylinders or bands have been proposed. In this regard, the magnitude of the steady-state currents at nanowire electrodes may be estimated using the equation applying to band electrodes approaching steady-state conditions<sup>14, 15</sup>:

$$i_{ss(band)} = \frac{2\pi nFLD_R C_R^*}{\ln\left(\frac{64D_R t}{w^2}\right)} \quad [3.11]$$

where  $i_{ss(band)}$  is the steady-state current (A),  $L$  is the length of the band electrode (45  $\mu\text{m}$ ),  $t$  is time (equal to  $RT/Fv$ , where  $R$  is the gas constant,  $T$  is temperature,  $v$  is the scan rate),  $w$  is electrode width (100 nm) and all other parameters take their usual meaning. Solving this equation for a nanowire electrode yielded an approximated steady-state current of 1.08 nA at a scan rate of  $100 \text{ mV}\cdot\text{s}^{-1}$ , which in terms of current density is equal to  $\sim 120 \text{ A}\cdot\text{m}^{-2}$ . Consequently, the steady-state currents for  $100 \text{ mV}\cdot\text{s}^{-1}$

are expected to be more or less the same value for both the ultra-microdisc and the nanowire electrodes. Nonetheless, the current density at a nanowire electrode is theoretically expected to be about 11 times higher than that at an ultra-microdisc electrode.

To confirm this, the corresponding experiments were carried out. At  $100 \text{ mV}\cdot\text{s}^{-1}$ , the steady-state current measured at an ultra-microdisc ( $\sim 1.4 \text{ nA}$ ) was slightly higher than that recorded at a nanowire ( $\sim 1.0 \text{ nA}$ ), which in both cases correlate well with the estimated values above. Furthermore, in term of current density, the signal at the nanowire ( $\sim 112 \text{ A/m}^2$ ) was about 10 times higher than that observed at the ultra-microdisc ( $\sim 11 \text{ A/m}^2$ ), see Figure 3.8, which is again in good agreement with the estimated values. Thus, nanowire electrodes present higher current density, higher signal-to-noise ratio, and higher sensitivity arising from enhanced mass transfer efficiency, which are critical for a wide range of applications.

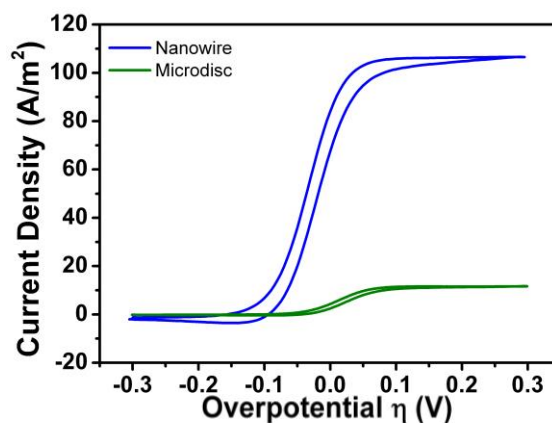


**Figure 3.8:** Typical cyclic voltammograms in 1 mM FcCOOH in 10 mM PBS at a scan rate of  $100 \text{ mV}\cdot\text{s}^{-1}$  measured at an ultra-microdisc (green line) and at a single nanowire (blue line), expressed in current density vs overpotential  $\eta$ .

### 3.3.5 Rapid Analysis at the Nanoscale

#### *Simulations*

Compared to ultra-microdiscs, enhanced mass transport should be observed at the nanowire electrodes, enabling faster analysis. To provide a better insight of the diffusional mass transport behaviour at both ultra-microdisc and nanowire electrodes with respect to analysis times, analyte concentration profiles simulations of a single electron oxidation process of 1 mM FcCOOH in 10 mM PBS solution were undertaken

for cyclic voltammograms at 50, 500 and 5000  $\text{mV}\cdot\text{s}^{-1}$ . Models were built using a simplified two dimensional model known as the diffusion domain approach, consisting of a representative cross sectional plane through an electrode as shown Figures 3.9 (a) and (c). In this manner, an ultra-microdisc was represented by a 12.5  $\mu\text{m}$  line (diameter) while a nanowire was outlined by a 50 nm x 100 nm rectangle (height x width) located centrally at the bottom of a much larger space domain. To ensure accuracy of the simulations, the domain area was selected so as to be large enough to ensure bulk-like conditions at the boundaries remain unaffected by the electrochemistry occurring at the electrodes. Figure 3.9 (b) and (d) depict the two-dimensional geometry of the model employed with boundary conditions for flux = 0 and for concentration of the reductive species R in the bulk and at the electrode surface with respect to time, respectively  $C_R^*$  and  $C_R(t)$ . During simulations the mesh was refined to reduce convergence error and simulations were allowed to iteratively resolve until an error less than 2% was achieved.

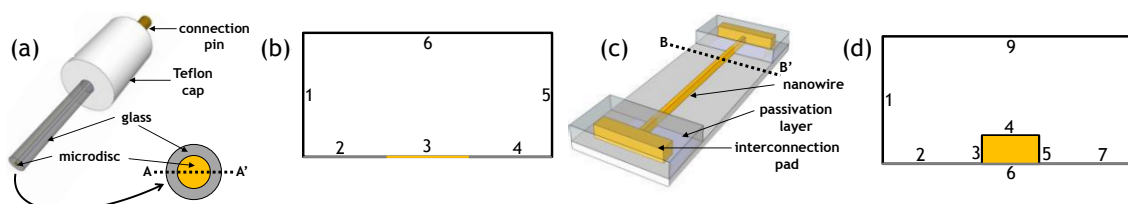


**Figure 3.9.** (a) Schematic diagram of an ultra-microdisc electrode. (b) 2D representation of an ultra-microdisc electrode (AA' section), used for simulation of diffusion. Boundaries 1, 5 & 6 define the bulk concentration,  $C^*$ . Boundaries 2 & 4 correspond to flux = 0. Boundary 3 is the concentration present at the electrode surface with respect to the time step of the electrolysis. (c) Schematic diagram of a nanowire electrode. (d) 2D representation of a nanowire electrode (BB' section), used for simulation of diffusion. Boundaries 1, 8 & 9 define the bulk concentration,  $C^*$ . Boundaries 2 & 7 correspond to flux = 0. No conditions are applicable at boundary 6. Boundaries 3, 4 & 5 are the concentration present at the electrode surface with respect to the time step of the electrolysis.

Simulated concentration profiles of 1 mM FcCOOH in 10 mM PBS at the ultra-microdisc electrode surface under cyclic voltammetric conditions at 50, 500 and 5000  $\text{mV}\cdot\text{s}^{-1}$  scan rates are presented in Figures 3.10 (a), (b) and (c), respectively. It can be seen that the shape of the simulated concentration profiles varies with the applied scan rate, indicative of a change in the mass transport behaviour to an ultra-microdisc. At 50  $\text{mV}\cdot\text{s}^{-1}$ , the diffusion layer thickness appears uniform and larger than the electrode diameter, suggesting analyte mass transport behaviour is dominated by radial diffusion. Hence, analyte consumption and its subsequent replenishment are expected, thus

enabling time-independent steady-state responses at long analysis times (low scan rates). At  $500 \text{ mV.s}^{-1}$ , the inner diffusion layers become planar, suggesting a change in the diffusional mass transport behaviour from radial to planar, also known as a transition zone. This would experimentally be confirmed by the appearance of slightly peak shaped cyclic voltammograms for intermediate analysis time scales. At  $5000 \text{ mV.s}^{-1}$ , the extent of the diffusion layer is of similar dimension as the electrode diameter, strongly suggesting that planar diffusion dominates at the electrode surface, corresponding to the analyte being consumed faster than it is replenished. This clearly indicates that ultra-microdisc electrodes would exhibit steady-state currents at high analysis time (low scan rates) but diffusion limited peak currents at short analysis times (high scan rates).

By comparison, Figures 3.10 (d), (e) and (f) show 2D concentration profiles of  $1 \text{ mM}$  FcCOOH in  $10 \text{ mM}$  PBS occurring at a single nanowire electrode at  $50 \text{ mV.s}^{-1}$ ,  $500 \text{ mV.s}^{-1}$  and  $5000 \text{ mV.s}^{-1}$  scan rates, respectively. For all potential scan rates, it is clear that the diffusion layer thickness is uniform and much larger than the nanowire electrode width. This strongly suggests that analyte mass transport behaviour is dominated by radial diffusion for all analysis times. Therefore, the rate of analyte replenishment is sufficiently fast to maintain sufficient analyte at the electrode surface to yield time-independent steady-state responses – not diffusion limited. It is important to note that these results are contingent on the ability to obtain highly reproducible nanowire electrodes.

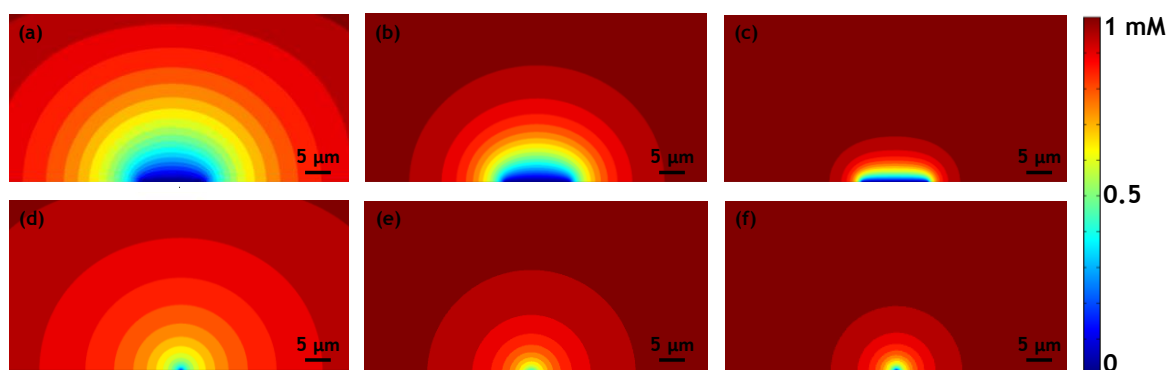


**Figure 3.10.** Simulated FcCOOH concentration profiles at a plane perpendicular to a single ultra-microdisc electrode, at scan rates of (a)  $50 \text{ mV.s}^{-1}$ , (b)  $500 \text{ mV.s}^{-1}$  and (c)  $5000 \text{ mV.s}^{-1}$ .  $C_R = 1 \text{ mM}$ ,  $D_R = 5.4 \times 10^{-6} \text{ cm}^2.\text{s}^{-1}$ ,  $E^o = 0.317 \text{ V}$ ,  $T = 298.15 \text{ K}$ . (d), (e) and (f) respectively are the equivalent FcCOOH concentrations profiles at a single nanowire electrode with  $E^o = 0.155 \text{ V}$ .

### Experimental Validation

Cyclic voltammetry experiments corresponding to the simulations presented in Figure 3.10 were performed. Typical cyclic voltammograms acquired at a gold ultra-microdisc electrode in 1 mM FcCOOH in 10 mM PBS at 50, 500 and 5000  $\text{mV}\cdot\text{s}^{-1}$  are presented in Figure 3.11 (a). At 50  $\text{mV}\cdot\text{s}^{-1}$ , the measured voltammogram was sigmoidal and reached steady-state currents indicating that at low analysis times the rate of analyte replenishment is sufficient. This confirmed that analyte mass transport is dominated by radial diffusion. Moreover, the magnitude of the steady-state current was found to be highly reproducible for measurements from three separate ultra-microdisc electrodes ( $n=15$ ),  $1.37 \pm 0.11$  nA, which is in strong agreement with the value determined using equation 3.6. At 500  $\text{mV}\cdot\text{s}^{-1}$ , the voltammogram shows small diffusive peaks in the forward and reverse scans indicating a change in mass transport from radial to planar diffusion. At 5000  $\text{mV}\cdot\text{s}^{-1}$ , ultra-microdiscs exhibit definite peak shaped current responses, pointing out that the analyte mass transport is completely dominated by planar diffusion. The magnitude of the peak currents were again found to be highly reproducible for measurements from three separate ultra-microdisc electrodes ( $n=15$ ), e.g.,  $1.66 \pm 0.14$  nA at 500  $\text{mV}\cdot\text{s}^{-1}$  and  $3.29 \pm 0.22$  nA at 5000  $\text{mV}\cdot\text{s}^{-1}$ . It is therefore clear that changes in the signal shape, from sigmoidal to peak shaped with decreasing analysis times, are indicative of changes in the diffusional mass transport behaviour at the ultra-microdisc electrode due to the relatively large critical dimension of the ultra-microdisc electrode compared to the thickness of the diffusion layer. All experimental results are in excellent agreement with the simulated concentration profiles obtained at an ultra-microdisc electrode.

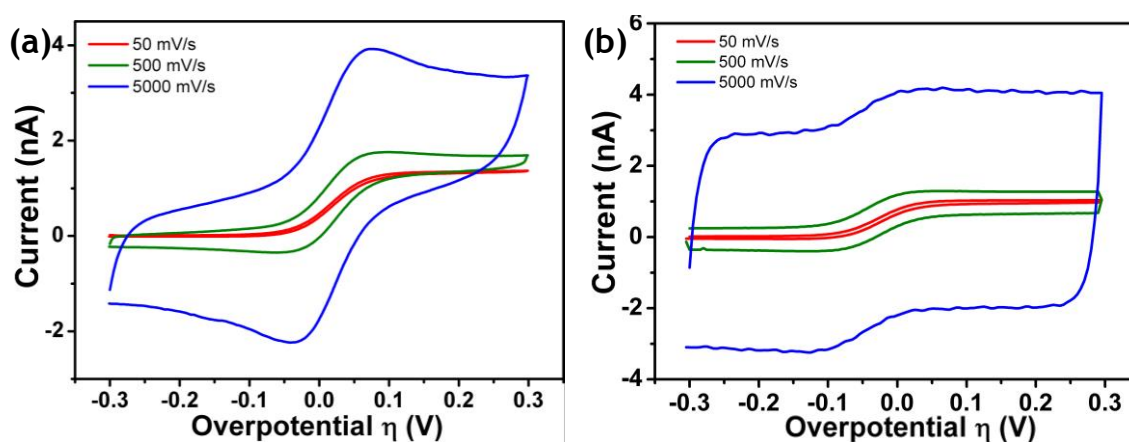


**Figure 3.11.** (a) Typical cyclic voltammograms obtained at an ultra-microdisc electrode in 1 mM FcCOOH in 10 mM PBS at 50, 500 and 5000  $\text{mV}\cdot\text{s}^{-1}$  scan rates, vs. overpotential  $\eta$ . (b) Equivalent cyclic voltammograms at a single nanowire electrode, vs. overpotential  $\eta$ .

Equivalent cyclic voltammograms obtained at nanowire electrodes are shown in Figure 3.11 (b). No significant changes in the shape of the signal were observed; all cyclic voltammograms were sigmoidal, exhibiting highly reproducible steady-state currents, as expected for the oxidation of a simple redox mediator such as FcCOOH at a nanoelectrode. This strongly suggests that the analyte mass transport behaviour to a nanowire electrode is radial and does not change regardless of the analysis time due to the very small critical dimension of the nanowire electrode. These data agree with the simulated concentration profiles, and suggest that the currents reach a time-independent steady state value. Cyclic voltammetry in 10 mM PBS solution (data not shown) only confirmed that the observed faradaic responses were exclusively due to the nanowire electrode, i.e., the photoresist layer sufficiently insulated the interconnection tracks from the electrolytic solution.

However, the measured steady-state currents were found to increase linearly with increasing scan rate, as seen in Figure 3.12. This is due to charging capacitive currents arising from the high electric fields associated with the metal interconnection tracks, rather than from the nanowire itself. Effectively, in collaboration with Mr Andrea Pescaglioni and Dr Karen Dawson (Nanotechnology group at Tyndall National Institute), we have shown that the passivation layer ( $\sim 500$  nm SiN<sub>x</sub>) permitted interfacial capacitance above the insulated interconnection tracks, which contributed dramatically to the experimentally measured current<sup>21</sup>. The average experimental value is  $0.65 \pm 0.16$  nF.

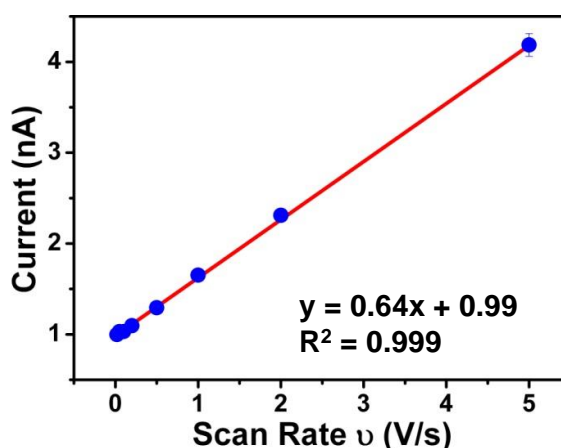


**Figure 3.12:** Measured steady-state current versus scan rate at a nanowire electrode.

Nevertheless, all background subtracted cyclic voltammograms displayed a steady-state current in the order of  $1.15 \pm 0.22$  nA ( $n=15$  for all scan rates), demonstrating that the

current reached a highly reproducible time-independent steady state current regardless of the analysis time, as shown in Figure 3.13.

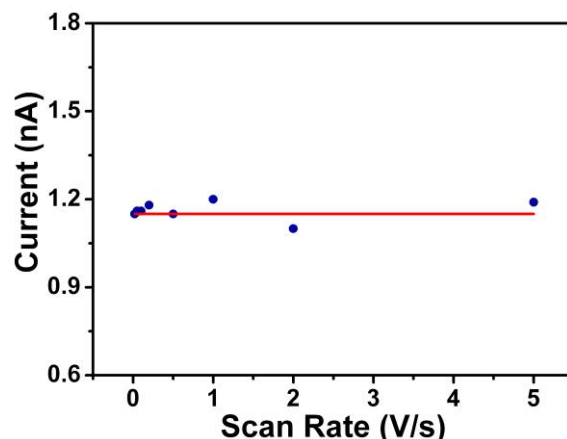


**Figure 3.13:** Background subtracted steady-state current versus scan rate at a nanowire electrode.

In other words, the linear dependence between the measured current,  $i_{measured}$ , and the applied potential scan rate,  $v$ , can be expressed as follows:

$$i_{measured} = C_{dl}v + i_{ss(nanowire)} \quad [3.12]$$

where  $C_{dl}$  is the overall (i.e. nanowire plus interconnects) capacitance,  $v$  is scan rate ( $\text{V}\cdot\text{s}^{-1}$ ) and  $i_{ss(nanowire)}$  is the nanowire steady-state current. Therefore, the capacitance corresponds to the slope of the line depicted in Figure 3.12, which in this case is 0.64 nF. This value is in very good agreement with the average value and with that published by Dr Karen Dawson (Nanotechnology group at Tyndall National Institute)<sup>19</sup>. The intercept of the line is  $i_{ss(nanowire)}$ ; in this case it is equal to 0.99 nA which is in very good agreement with the average value. The theoretical expression for  $i_{ss(nanowire)}$  has yet to be determined as it is not available in the literature for this electrode dimension and geometry. This suggests that the equation applying to band electrodes (equation 3.11) does not apply for protruding nanowire electrodes but can be used as an approximation.

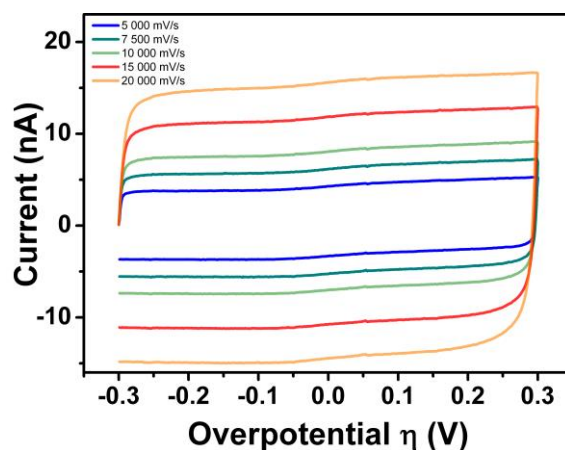


**Figure 3.14.** Typical cyclic voltammograms obtained at a gold nanowire electrode in 1 mM FcCOOH in 10 mM PBS at 5, 7.5, 10, 15 and 20  $\text{V}\cdot\text{s}^{-1}$  scan rates, vs. overpotential  $\eta$ .

Furthermore, cyclic voltammograms were recorded for scan rates up to  $20,000 \text{ mV}\cdot\text{s}^{-1}$ , before the faradaic signals were swamped by the capacitive charging currents, as depicted in Figure 3.14. These currents were also found to increase linearly with increasing scan rate. Consequently, nanowire electrodes allow for the employment of significantly high analysis rates when compared to ultra-microdisc electrodes, e.g.,  $20,000 \text{ mV}\cdot\text{s}^{-1}$  compared to  $100 \text{ mV}\cdot\text{s}^{-1}$  for ultra-microdisc electrodes, while maintaining time-independent steady-state currents. To put this in context, a cyclic sweep at  $100 \text{ mV}\cdot\text{s}^{-1}$  takes approximately 10-15 s (depending on the potential window). At  $20,000 \text{ mV}\cdot\text{s}^{-1}$ , this reduces analysis times down to 50-60 ms (up to a 300 fold decrease) without the loss of the steady-state and time-independent current behaviour. Thus rapid signal acquisition which is critical for sensing applications is possible with electron-beam lithography fabricated nanowires. Work is now on-going to block or eliminate the capacitive currents associated with the interconnection tracks by the inclusion of an on-chip faradaic shield in order to permit even faster analysis.

### 3.4 Summary and Conclusion

In this Chapter, a theoretical and experimental comparative study of the mass transport behaviour at commercial gold ultra-microdisc electrodes (6.25  $\mu\text{m}$  in radius) and at gold nanowire electrodes fabricated by a hybrid electron-beam/photolithography process (100 nm wide x 50 nm high x 45  $\mu\text{m}$  long) is presented. To this end, the effects of scan rates on FcCOOH diffusion at both ultra-microdisc and nanowire electrodes were simulated and the corresponding measurements were carried out. Cyclic voltammograms at ultra-microdisc electrode exhibited highly reproducible time-independent steady-state voltammograms at low scan rates, indicative of fast mass transport, while at high scan rates highly reproducible diffusion limited peak current responses were recorded. By contrast, cyclic voltammograms at nanowire electrodes displayed highly reproducible time-independent steady-state currents at scan rates up to 20,000  $\text{V}\cdot\text{s}^{-1}$ , indicative of an enhanced radial diffusion mass transport. The enhanced mass transport efficiency at nanowire electrodes contributed to improved signal-to-noise ratio, improved sensitivity, a tenfold improvement in current density and up to a 300 fold decrease in analysis time while maintaining steady-state conditions. Further work is now on-going to block or eliminate the capacitive currents associated with the interconnection tracks to permit even higher scan rates.

Furthermore, although its wide-spread take-up may be restrained by its relatively high cost, the high yield of well-defined reproducible devices and fast fabrication turnaround make electron-beam lithography an interesting platform to develop prototypes of nanowire based sensing platforms. In this regard, the research described in the following Chapters focuses on exploring the capabilities of individual gold nanowire electrodes and gold nanowire electrode arrays fabricated using electron-beam lithography and contacted using optical lithography.

### 3.5 References

1. Kolmakov, A.; Zhang, Y.; Cheng, G.; Moskovits, M., Detection of CO and O<sub>2</sub> using tin oxide nanowire sensors. *Adv. Mater.* **2003**, 15, 997-1000.
2. Wan, Q.; Li, Q.; Chen, Y.; Wang, T.; He, X.; Li, J.; Lin, C., Fabrication and ethanol sensing characteristics of ZnO nanowire gas sensors. *Applied Physics Letters* **2004**, 84, 3654-3656.
3. Walter, E.; Penner, R.; Liu, H.; Ng, K.; Zach, M.; Favier, F., Sensors from electrodeposited metal nanowires. *Surface and interface analysis* **2002**, 34, 409-412.
4. Arrigan, D. W., Nanoelectrodes, nanoelectrode arrays and their applications. *Analyst* **2004**, 129, 1157-1165.
5. Aoki, K., Theory of ultramicroelectrodes. *Electroanalysis* **1993**, 5, 627-639.
6. Zoski, C. G., *Handbook of electrochemistry*. Access Online via Elsevier: 2007.
7. Contreras, A. M.; Grunes, J.; Yan, X.-M.; Liddle, A.; Somorjai, G., Fabrication of platinum nanoparticles and nanowires by electron beam lithography (EBL) and nanoimprint lithography (NIL): comparison of ethylene hydrogenation kinetics. *Catalysis letters* **2005**, 100, 115-124.
8. Pease, R., Electron beam lithography. *Contemporary Physics* **1981**, 22, 265-290.
9. Vieu, C.; Carcenac, F.; Pepin, A.; Chen, Y.; Mejias, M.; Lebib, A.; Manin-Ferlazzo, L.; Couraud, L.; Launois, H., Electron beam lithography: resolution limits and applications. *Applied Surface Science* **2000**, 164, 111-117.
10. Hu, W.; Sarveswaran, K.; Lieberman, M.; Bernstein, G. H., High-resolution electron beam lithography and DNA nano-patterning for molecular QCA. *Nanotechnology, IEEE Transactions on* **2005**, 4, 312-316.
11. Tseng, A. A.; Chen, K.; Chen, C. D.; Ma, K. J., Electron beam lithography in nanoscale fabrication: recent development. *Electronics Packaging Manufacturing, IEEE Transactions on* **2003**, 26, 141-149.
12. Liu, K.; Avouris, P.; Bucchignano, J.; Martel, R.; Sun, S.; Michl, J., Simple fabrication scheme for sub-10 nm electrode gaps using electron-beam lithography. *Applied physics letters* **2002**, 80, 865-867.
13. Ching, S.; Dudek, R.; Tabet, E., Cyclic voltammetry with ultramicroelectrodes. *Journal of chemical education* **1994**, 71, 602.
14. Berduque, A.; Lanyon, Y. H.; Beni, V.; Herzog, G.; Watson, Y. E.; Rodgers, K.; Stam, F.; Alderman, J.; Arrigan, D. W., Voltammetric characterisation of silicon-based microelectrode arrays and their application to mercury-free stripping voltammetry of copper ions. *Talanta* **2007**, 71, 1022-1030.

15. Lanyon, Y. H.; Arrigan, D. W., Recessed nanoband electrodes fabricated by focused ion beam milling. *Sensors and Actuators B: Chemical* **2007**, 121, 341-347.
16. Molina, A.; Gonzalez, J.; Henstridge, M.; Compton, R., Voltammetry of Electrochemically Reversible Systems at Electrodes of Any Geometry: A General, Explicit Analytical Characterization. *The Journal of Physical Chemistry C* **2011**, 115, 4054-4062.
17. Godino, N.; Borrisse, X.; Munoz, F. X.; del Campo, F. J.; Compton, R. G., Mass transport to nanoelectrode arrays and limitations of the diffusion domain approach: theory and experiment. *The Journal of Physical Chemistry C* **2009**, 113, 11119-11125.
18. Guerrette, J. P.; Percival, S. J.; Zhang, B., Voltammetric behavior of gold nanotrench electrodes. *Langmuir* **2011**, 27, 12218-12225.
19. Dawson, K.; Wahl, A. I.; Murphy, R.; O'Riordan, A., Electroanalysis at Single Gold Nanowire Electrodes. *The Journal of Physical Chemistry C* **2012**, 116, 14665-14673.
20. Denuault, G.; Mirkin, M. V.; Bard, A. J., Direct determination of diffusion coefficients by chronoamperometry at microdisk electrodes. *Journal of electroanalytical chemistry and interfacial electrochemistry* **1991**, 308, 27-38.
21. Dawson, K.; Wahl, A.; Pescaglioni, A.; Iacopino, D.; O'Riordan, A., Gold Nanowire Electrode Arrays: Investigations of Non-Faradaic Behavior. *Journal of The Electrochemical Society* **2014**, 161, B3049-B3054.

*Chapter 4*

**Electroanalysis at Gold Nanowires Arrays:  
Simulation Study and Electrochemical Experiments**



## 4.1 Introduction

Recent developments in fabrication of robust and reproducible nanoelectrodes have opened the door to a new and exciting area of electrochemistry<sup>1, 2</sup>. Typically, these electrodes demonstrate enhanced performance, when compared to microelectrodes and ultra-microelectrodes, due to improved mass transport occurring at the nanoscale<sup>3, 4</sup>. As has been discussed in the previous chapters, the enhanced mass transport comes predominantly from radial diffusion at the nanoscale, thereby offering the potential for improvements in analytical and sensor applications in terms of faster and more sensitive electroanalysis, improved kinetic measurements of electrochemical processes, and significantly reduced sample volumes.

Additionally, the use of very small electrodes would permit high densities of sensors to be fabricated in a much smaller footprint at key substrates, such as on silicon chips, thus enabling much greater information-gathering capability per device. To date, although a significant portion of studies employing nanoscale electrodes on silicon chips have been undertaken using nanodiscs, nanopores or short inlaid nanobands<sup>5</sup>, large arrays of these nanostructures are required to obtain reasonable measurable currents, i.e., in the nanoampere regime. By contrast, high aspect ratio nanostructures such as nanowires and nanobands have not been reported extensively in the literature<sup>6-9</sup>. This reflects the difficulty in both fabrication and integration of nanowire electrodes as functional sensing elements in devices. Nevertheless, we and others have reported some approaches employing nanowires electrodes<sup>3, 10-12</sup>. In Chapter 3, individual gold nanowire electrodes, fabricated on silicon chips by electron-beam lithography and contacted using photolithography, exhibited relatively large currents (nA) due to their micrometric length (typically > 40  $\mu\text{m}$ ), but they also benefit from radial diffusion profiles arising from their nanometre scale critical dimension. As such, these electrodes exhibit steady-state voltammograms indicative of fast analyte mass transport to the electrode even at very high scan rates (20,000  $\text{mV}\cdot\text{s}^{-1}$ ). These advances in nanofabrication techniques pioneered by the micro/nano-electronic industry including: electron beam, nanoimprint and phase-shift lithographies, have made fabrication and integration of robust and reproducible nanowire electrodes routinely achievable at

reasonable economic cost.

Furthermore, nanowire array electrodes offer the potential for even more enhancements in electroanalysis including: increased signal-to-noise ratio and increased sensitivity while also allowing quantitative detection at much lower concentrations. However, to achieve this goal, a full understanding of the diffusion profiles existing at nanowire arrays is required. During electron transfer processes, electroactive species around the electrode are depleted creating depletion zones known as Nernst diffusion layers,  $\delta$ , which thickness varies considerably with the electrode dimensions and geometry. In sweep voltammetry, a diffusion-limited and time-dependent response (planar diffusion) generally occurs with larger electrodes (e.g. microelectrodes), while an ideal steady-state and time-independent response (radial diffusion) would be typical of much smaller electrodes (e.g. ultra-microelectrodes)<sup>3, 13</sup>.

At present, there is no analytical equation to describe diffusion to an electrode geometry where an electrode has sharp edges and protrudes from a planar substrate, i.e., a nanowire. For this reason, analytical solutions based on similar geometries such as hemicylinders or nanobands have been proposed and adopted to estimate voltammetric/mass transport behaviour at nanowire electrodes<sup>14</sup>. In this regard, the thickness of a Nernst diffusion layer,  $\delta$ , at a hemicylindrical electrode approaching steady-state conditions can be estimated via the following equation:

$$\delta = r_0 \left( \frac{2(D_0 t)^{1/2}}{r_0} \right) \quad [4.1]$$

where  $D_0$ , is the diffusion coefficient of the electroactive species,  $t$  is time and  $r_0$  is the electrode radius. For a nanowire  $r_0 = w/4$  where,  $w$  is the width of the electrode. In this manner diffusion independence is theoretically maintained by ensuring that the separation between neighbouring electrodes,  $s$ , is greater than twice the diffusion thickness ( $s > 2\delta$ ). However, we and others have recently shown that this is not the case at the nanoscale and significantly larger separations are required to maintain diffusional independence between neighbouring electrodes and this separation is significantly affected by the applied scan-rate<sup>15, 16</sup>.

In this Chapter, we undertook finite element analysis of diffusion profiles existing at arrays of nanowire electrodes with Comsol Multiphysics® and explored the effects of altering inter-electrode separations on diffusional independence for a range of scan

rates. Although a range of scan rates were modelled, we are particularly interested in very high scan rates ( $5,000 \text{ mV.s}^{-1}$ ) since this allows rapid (sub 1 second) data capture required for, e.g., biomedical, environmental and pharmaceutical diagnostic applications. To confirm our simulations experimentally, nanowire electrode arrays were fabricated and fully integrated on silicon chips using the same approach as in Chapter 3, i.e., electron-beam lithography, metal evaporation and lift-off techniques. These devices include twelve separate electron-beam fields containing arrays of three nanowire electrodes separated by 5, 10, 15 or 20  $\mu\text{m}$ , an on-chip gold counter electrode, an on-chip platinum pseudo-reference electrode and peripheral contact pads to facilitate direct electrical and electrochemical probing. Individual nanowire electrode dimensions were characterised using a combination of optical, scanning electron and atomic force microscopies. Electrochemical characterisation of the nanowire arrays was undertaken to explore the diffusional process occurring at arrays with increasing inter-electrode separation. We show that arrays that are diffusionally independent demonstrate superior electrochemical performance when employing sweep voltammetric techniques compared to arrays with overlapping diffusion profiles. By contrast, arrays with diffusionally overlapping profiles exhibit enhanced performance when employing step voltammetric techniques. However, large charging currents were observed at nanowire due to the high electric fields associated with metal interconnection tracks, rather than from the nanowire itself.

---

This work has been published in full as ‘Electroanalysis at Gold Nanowires Arrays: Simulation Study and Electrochemical Experiments’ *Faraday Discussions*, 164, 377 **2013**

## 4.2 Experimental

### 4.2.1 Finite-Element Simulations

Same as previously, see subsection 3.2.7, concentration profiles for the oxidation of FcCOOH at electrode arrays containing three nanowires were simulated using the ‘transport of diluted species’ modelling platform in the ‘chemical species transport’ module comprised in the commercial finite element software package Comsol Multiphysics<sup>®</sup> 4.1. (Comsol, SE). The objective of these simulations is to assess the distance required between adjacent nanowires to allow independent diffusional mass transport to each nanowire electrodes, at high scan rates using cyclic voltammetry. Simulations were carried out prior to electrode fabrication.

### 4.2.2 Nanowire Electrode Array Design, Fabrication and Cell Set-up

Electron-beam lithography masks are software based so that patterns can be easily altered. Therefore, nanowire electrode arrays were fabricated using the same chip layout and fabrication approach as for the individual nanowire electrodes employed in Chapter 3, see subsections 3.2.1 to 3.2.3. To this end, the only difference consisted in changing the mask design such that, instead of individual nanowire electrodes, arrays of three nanowire electrodes separated by 5, 10, 15 or 20  $\mu\text{m}$  were patterned into the twelve different central 80  $\mu\text{m}$  x 80  $\mu\text{m}$  electron-beam fields of each silicon chip. Same as previously, a hybrid process was employed, whereby only the nanowire structures were defined by electron-beam lithography and photolithography was employed to fabricate overlaid interconnection tracks, as well as an on-chip gold counter electrode, an on-chip platinum pseudo-reference electrode and peripheral contact pads; a passivation layer selectively insulated these structures. Following fabrication, wafers were diced into 16 x 16 mm chips, which were then mounted in the same electrochemical cell set-up employed in the previous Chapter.

### 4.2.3 Nanowire Arrays Structural and Electrical Characterisation

As before, optical micrographs were acquired using a calibrated microscope (Axioskop II, Carl Zeiss Ltd.) equipped with a charge-coupled detector camera (CCD; DEI-750,

Optronics). Structural characterisation was undertaken using a field emission scanning electron microscope (JSM-6700F, JEOL UK Ltd.) operating at beam voltages between 5 and 10 kV. As a quality control check and to confirm electrical functionality, two-point electrical measurements were performed using a probe station (Model 6200, Micromanipulator Probe Station) in combination with a source meter (Keithly 2400) and a dedicated LabVIEW™ V8.0 program. In these current-voltage measurements, the source electrode was grounded, a bias sweep up to  $\pm 10$  mV was applied to the drain electrode, and the current through the nanowires was measured.

#### 4.2.4 Electrochemical analysis

All electrochemical studies were performed using a CHI660A Electrochemical Analyser and Faraday Cage CHI200B (CH Instruments). All experiments were carried out in a three-electrode electrochemical cell using gold nanowire working electrode arrays, versus the on-chip gold counter and on-chip platinum pseudo-reference electrodes; chips were mounted on a home-made cell. Cyclic voltammetry was conducted in 1 mM ferrocene monocarboxylic acid in 10 mM phosphate buffer saline solution, pH 7.4 and deaerated with nitrogen gas, in the voltage range of -0.15 V to 0.45 V, for a variety of scan rates from 5 to 5,000  $\text{mV}\cdot\text{s}^{-1}$ . Square wave voltammograms were undertaken in 0.1 to 5 mM ferrocene monocarboxylic acid in 10 mM phosphate buffer saline solutions and in 10 mM phosphate buffer saline only, pH 7.4 and deaerated with nitrogen gas, across a voltage range of -0.15 to 0.45 V with an incremental potential of 1 mV, a potential amplitude of 25 mV and a frequency of 25 Hz. Prior to electrochemical experiments, electrodes were cleaned by sequential immersion of chips for 10 minutes in acetone (bath 1), trichloroethylene, acetone (bath 2), and isopropyl alcohol, followed by a thorough rinse with deionised water and dried in a stream of filtered nitrogen.

#### 4.2.5 Chemicals and Glassware

Unless otherwise stated, all chemicals were purchased from Sigma-Aldrich and were used as received. All solutions were freshly prepared on a weekly basis with deionised water of resistivity 18.2  $\text{M}\Omega\cdot\text{cm}$  (ELGA Pure Lab Ultra).

## 4.3 Results and discussion

### 4.3.1 Simulation at Nanowire Electrode Arrays: Assessment of the Inter-electrode Separation

Due to the high aspect ratio of the nanowires within an array, a simplified two dimensional model known as the diffusion domain approach was adopted. In this approach, a cross sectional plane through an array comprising of three nanowires was defined, where each nanowire electrode within an array was assigned its own area; see Figure 4.1 (a). In this manner, each nanowire was outlined by a 50 nm x 100 nm rectangle (height x width) located centrally at the bottom of a much larger rectangle (space domain). To ensure accuracy of the simulations, the domain area is selected so as to be large enough to ensure bulk-like conditions at the boundaries remain unaffected by the electrochemistry occurring at the electrodes. Figure 4.1 (b) depicts the two-dimensional geometry of the model employed with boundary conditions for flux = 0 and for concentration of the reductant species R in the bulk and at the electrode surface with respect to time, respectively  $C_R^*$  and  $C_R(t)$ . During simulations the mesh was duly refined and simulations were allowed to iteratively resolve until a convergence error less than 2% was achieved.

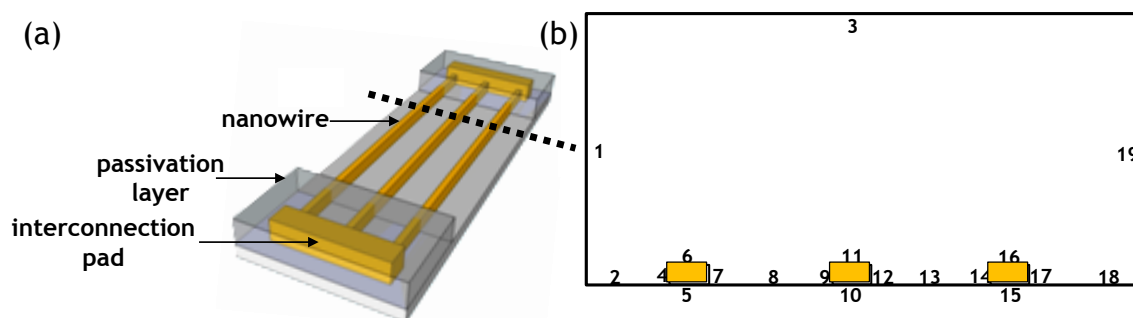


**Figure 4.1:** (a) Schematic diagram of three nanowire electrodes in array. (b) 2D representation of three nanowire electrodes in array, used for simulation of diffusion at nanowire electrodes. Boundaries 1, 3 & 19 define the bulk concentration,  $C^*$ . Boundaries 2, 8, 13 & 18 correspond to flux = 0. No conditions are applicable at boundaries 5, 10 & 15. Boundaries 4, 6, 7, 9, 11, 12, 14, 16, & 17 are the concentration present at the electrode surface with respect to the time step of the electrolysis,  $C_R(t)$ .

In the previous Chapter, we have demonstrated that radial diffusion of 1 mM FcCOOH in 10 mM PBS occurs at single gold nanowire electrodes (50 nm high x 100 nm wide x 45  $\mu\text{m}$  long) using cyclic voltammetry for scan rates ranging from 20  $\text{mV}\cdot\text{s}^{-1}$  to 20,000  $\text{mV}\cdot\text{s}^{-1}$ . At electrode arrays, the inter-electrode separation is the critical factor that

determines whether diffusional profiles overlap when other parameters including: electrode width, solution composition (buffer type, concentration, etc.) and scan rate are kept constant. In this Chapter, arrays containing three nanowires were chosen as they contain only one inner electrode competing for diffusional species on either side. Models were built for  $5,000 \text{ mV}\cdot\text{s}^{-1}$  at three nanowire arrays with increasing inter-electrode separations, i.e., 5, 10, 15 and 20  $\mu\text{m}$ , for which diffusion profiles using 1 mM ferrocene monocarboxylic acid in 10 mM phosphate buffer saline solution under cyclic voltammetric conditions were calculated. The nanowire dimensions were maintained as 100 nm in width and 50 nm in height with  $D_R = 5.4 \times 10^{-6} \text{ cm}^2\cdot\text{s}^{-1}$ ,  $E^0 = 0.155 \text{ V}$ ,  $T = 298.15 \text{ K}$ . As can be clearly seen in Figures 4.2 (a) and (b), overlap of adjacent diffusion layers occurs for three nanowire arrays with inter-electrode separations of 5 and 10  $\mu\text{m}$ . By comparison, in Figures 4.2 (c) and (d), for 15 and 20  $\mu\text{m}$  inter-electrode distances, the diffusion layers at each electrode in the array are completely independent from each other and radial in shape, suggesting that each of the three electrodes in the array should behave as an individual electrode and that the current response of the whole array should be equivalent to three times that of a single nanowire.

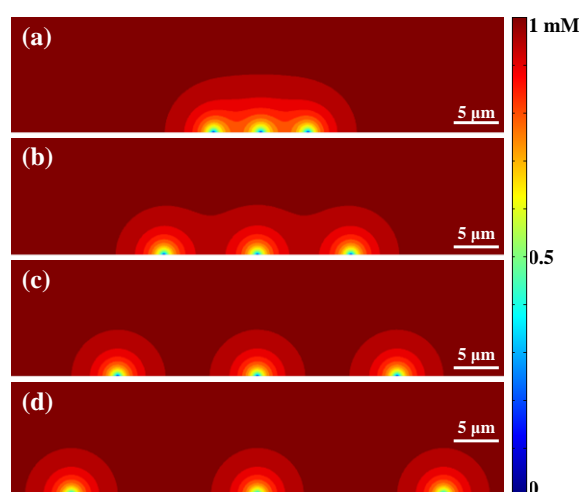


**Figure 4.2:** 2D simulations of FcCOOH concentration profiles at three nanowire arrays separated by: (a) 5  $\mu\text{m}$ , (b) 10  $\mu\text{m}$ , (c) 15  $\mu\text{m}$  and (d) 20  $\mu\text{m}$  at  $5000 \text{ mV}\cdot\text{s}^{-1}$ .

### 4.3.2 Nanowire Electrode Arrays Fabrication and Structural Characterisation

To confirm simulation results, gold nanowire arrays were fabricated using a hybrid electron beam/photolithography process at Si/SiO<sub>2</sub> substrates, as described in the experimental section. Following fabrication, electrodes were structurally characterised using optical, scanning electron and atomic force microscopies.

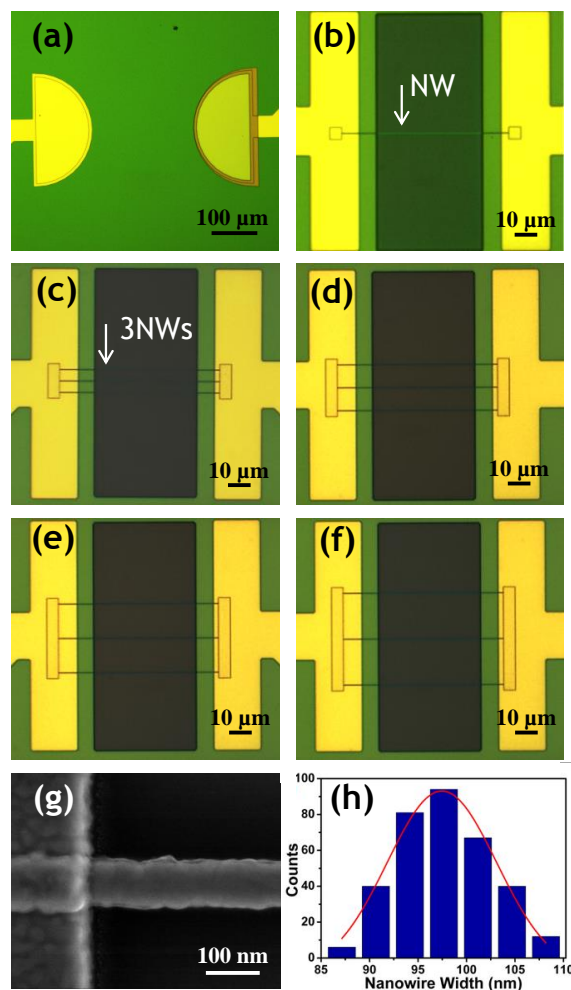


**Figure 4.3:** Optical micrographs of fully integrated and passivated (a) gold counter (left) and platinum pseudo-reference electrodes (right), (b) single gold nanowire electrode. Nanowire electrode arrays containing three nanowires separated by (c) 5  $\mu\text{m}$ , (d) 10  $\mu\text{m}$ , (e) 15  $\mu\text{m}$  and (f) 20  $\mu\text{m}$ . The darker rectangle in the middle corresponds to the trench selectively opened in silicon nitride above the nanowires to allow contact with an electrolyte solution. (g) High magnification scanning electron micrograph of a region of passivated and fully exposed nanowire. (h) Histogram showing the distribution of widths of nanowires obtained from scanning electron micrograph analysis; the solid red line is a Gaussian fit to the data.

Figure 4.3 (a) shows an optical micrograph of an on-chip gold counter electrode (left) and an on-chip platinum pseudo-reference electrode (right). For comparison purposes, an optical image of a fully fabricated, integrated and passivated single nanowire device employed in Chapter 3 is shown in Figure 4.3 (b). The gold squares at both nanowire termini were defined during the electron-beam lithography step to enhance electrical contact with overlaid by the metallic interconnection tracks. Figures 4.3 (c) to (f) are optical micrographs of fully fabricated, integrated and passivated three nanowire electrodes in array separated by 5, 10, 15 and 20  $\mu\text{m}$ , respectively. The gold bars at the nanowire termini were again employed to enhance electrical contact. The width of the

passivation window (central dark rectangle) defined the exposed nanowire length at  $\sim 45$   $\mu\text{m}$  for both single nanowires and nanowire arrays. Visual inspection using scanning electron microscopy reveals excellent registration between nanowire electrodes and the overlaid micron-scale interconnection tracks, ensuring nanowires are well electrically contacted and uniform in width; see Figure 4.3 (g). A statistical analysis at multiple locations across seventeen individual nanowire structures ( $n = 340$ ) from different chips yielded an average nanowire width of  $98 \pm 5$  nm (variation of  $\sim 5.1\%$ ), as presented in Figure 4.3 (h). Nanowire height were characterised as previously by Dr Karen Dawson; nanowires have a height of  $50.6 \pm 0.8$  nm and a roughness factor of  $1.5 \pm 0.2$ . This yielded a calculated nanowire geometric active surface area of  $2.7 \times 10^{-7}$   $\text{cm}^2$  and an average actual surface area of  $\sim 4.05 \times 10^{-7}$   $\text{cm}^2$  available for electrochemical analysis. The average width and height are in excellent agreement with those obtained in Chapter 3. This highlights the high reproducibility of the fabrication process such that very little to no variation in nanowires dimensions form chip to chip and batch to batch were observed.

### 4.3.3 Nanowire Electrode Arrays Electrical Characterisation

Fully fabricated nanowire electrode array devices were electrically characterised using standard two-point current-voltage measurements in air to ensure their functionality prior to electroanalysis. This was performed by contacting the two contact pads related to a nanowire device to two individual measuring probes. A voltage bias of  $\pm 10$  mV was selected to avoid undesired electro-migration effects which may damage the electrodes. All functioning devices displayed ohmic linear and very reproducible responses confirming excellent electrical contact to the electrodes by the overlaid interconnection tracks, see Figure 4.4. Fully packaged nanowires across multiple chips exhibited low resistance ( $539 \pm 26$   $\Omega$ ,  $n = 40$ ) regardless of the inter-electrode separation; shown in the inset of Figure 4.4. This very low variation ( $\sim 5.3\%$ ) in electrical performance is consistent with that observed for nanowire dimensions. Control electrical measurements were obtained in the absence of nanowires, yielding very high resistances ( $\sim 10$   $\text{G}\Omega$ ) typical of an open circuit. This confirms that the underlying silicon oxide functioned as an effective insulating layer preventing electrical coupling with the silicon beneath and that the observed electrical characteristics were

exclusively generated by the nanowire arrays and associated on-chip metal interconnection tracks. Nanowire array devices that exhibited high resistances or open circuit behaviour were discarded.

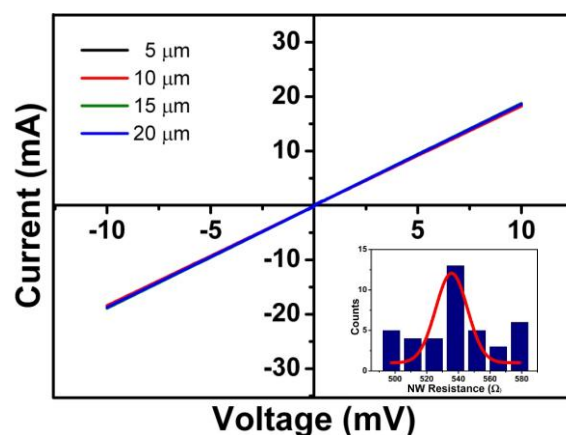


**Figure 4.4:** Typical two-point current-voltage characteristics for three nanowire arrays with inter-electrode separations of 5, 10, 15 and 20  $\mu\text{m}$ . Inset: histogram of the distribution of resistances; solid red line is a Gaussian fit to the data with an average resistance of  $539 \pm 26 \Omega$ .

#### 4.3.4 Cyclic Voltammetry at Nanowire Electrode Arrays: Assessment of the Inter-electrode Separation

Following fabrication of highly reproducible nanowire electrode arrays, cyclic voltammetry experiments corresponding to the simulations presented in Figure 4.2 were performed. Signals recorded at multiple nanowire arrays from different chips ( $n=15$ ) were highly reproducible and typical data at three nanowires separated by 5  $\mu\text{m}$  and 15  $\mu\text{m}$  is shown in Figure 4.5.

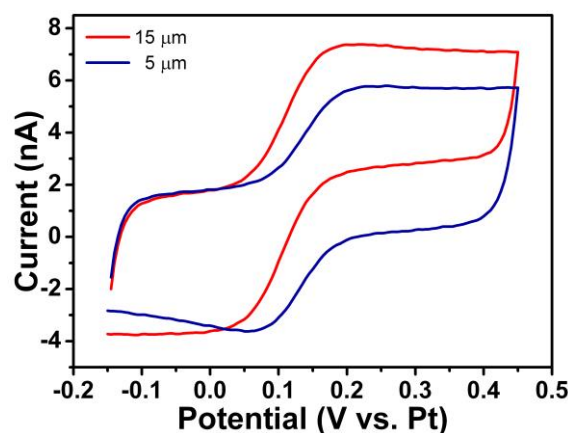


**Figure 4.5:** Cyclic voltammograms at arrays comprising three nanowires separated by 5 and 15  $\mu\text{m}$ , obtained at a  $5,000 \text{ mV}\cdot\text{s}^{-1}$  scan rate in 1 mM FcCOOH in 10 mM PBS.

The forward sweep of the 5  $\mu\text{m}$  spaced array exhibits steady-state behaviour, however, a diffusive peak is evident on the return reduction sweep indicative of diffusional overlap which is in agreement with the simulation results. By contrast, both the forward and backward sweeps of the 15  $\mu\text{m}$  spaced array exhibit steady-state behaviour also in agreement with the simulation results. These data strongly suggest that these electrodes are fully diffusionally independent.

#### 4.3.5 Signal Enhancement at Nanowire Arrays vs. Single Nanowire Electrode

In Chapter 3, cyclic voltammograms at single nanowire electrodes were recorded in 1 mM FcCOOH in 10 mM PBS solution at scan rates ranging from 20 to 20,000  $\text{mV}\cdot\text{s}^{-1}$ . All cyclic voltammograms were sigmoidal, exhibiting highly reproducible steady-state currents, thereby suggesting the analyte mass transport behaviour to a nanowire electrode is radial and is independent of analysis time due to the very small critical dimension of the nanowire electrode. However, the measured steady-state currents were found to increase linearly with increasing scan rate due to charging capacitive currents arising from the high electric fields associated with the metal interconnection tracks, rather than from the nanowire itself. As such, the measured current may be expressed as follows:

$$i_{measured} = C_{dl}v + i_{ss(nanowire)} \quad [4.2]$$

where  $C_{dl}$  is the overall capacitance and  $i_{ss(nanowire)}$  is the nanowire steady-state current. The capacitance and the steady state current were found to respectively be  $0.65 \pm 0.16$  nF and  $1.15 \pm 0.22$  nA. Moreover, when electrodes in an array are diffusionally independent, the faradaic current should be the same as a single electrode multiplied by the number of electrodes in the array. Therefore, for diffusionally independent nanowires, the measured current for three nanowires electrodes in array may be equal to:

$$i_{measured} = C_{dl}v + 3 i_{ss(nanowire)} \quad [4.3]$$

We have also previously demonstrated that the capacitance is principally due to high electric fields associated with the interconnection tracks<sup>17</sup>, and since the fabrication approach and the chip layout for single nanowires and nanowire in array are the same, the capacitance for nanowire arrays is also equal to  $0.65 \pm 0.16$  nF. As such, the

estimated current at diffusionally independent three nanowire electrodes in arrays for a  $5,000 \text{ mV.s}^{-1}$  scan rate is around  $6.70 \text{ nA}$ . For three nanowires with overlapping diffusion profiles, the current is expected to be lower than this value.

Experimentally, the magnitude of the steady-state currents for all nanowire electrode devices were found to be highly reproducible for measurements from separate three nanowire arrays on different chips ( $n=15$  for each array). The average steady-state currents measured at nanowires separated by  $5 \text{ }\mu\text{m}$  and  $10 \text{ }\mu\text{m}$  respectively are  $5.92 \pm 0.27 \text{ nA}$  and  $6.24 \pm 0.32 \text{ nA}$ . These values are slightly lower than the expected value, thereby confirming diffusional overlap between adjacent concentration profiles. The average currents measured for nanoelectrode arrays separated by  $15 \text{ }\mu\text{m}$  and  $20 \text{ }\mu\text{m}$ , respectively  $7.05 \pm 0.51 \text{ nA}$  and  $6.98 \pm 0.39 \text{ nA}$ , are the same (within experimental error) as the expected value. It is therefore likely the case that the increase in measured current for the latter two arrays arises from improved mass transport, i.e., nanowires are diffusionally independent. By subtracting the contribution of the average charging currents ( $C_{dl}v = 3.25 \text{ nA}$ ) from the overall average measured steady-state currents, the average increase in faradaic peak current is  $\sim 42\%$ :  $3.80 \text{ nA}$  for  $15 \text{ }\mu\text{m}$  spaced arrays compared with  $2.67 \text{ nA}$  for the  $5 \text{ }\mu\text{m}$  spaced arrays,

#### 4.3.6 Determination of Heterogeneous Kinetics

Steady-state cyclic voltammograms allow kinetic information for an electronic transfer process occurring at an electrode surface such as the heterogeneous rate of electron transfer  $k_0$  to be determined. Historically, experiments undertaken to determine  $k_0$  using macro and ultra-microelectrodes have been diffusion limited as such that low values have been reported<sup>18-21</sup>. The advent of nanoscale electrodes have eliminated diffusion effects and permitted higher (truer) values to be experimentally determined<sup>10</sup>. To this end, kinetic analysis was undertaken on steady-state cyclic voltammograms of a single electron oxidation of FcCOOH at arrays of three nanowires separated by  $5$  and  $15 \text{ }\mu\text{m}$ . In order to reduce artefacts caused by capacitive currents, we deduced the rate transfer from cyclic voltammograms captured at  $5 \text{ mV.s}^{-1}$ . The oxidative experimental voltammograms at  $5 \text{ mV.s}^{-1}$  were plotted in Origin Pro 8.5 (OriginLab Corporation, USA). Assuming identical diffusion coefficients of the oxidised and reduced species

and a uniformly accessible electrode surface, the steady-state voltammogram of an uncomplicated quasi-reversible one-electron oxidation reaction may be expressed by Butler-Volmer type kinetics<sup>10, 22</sup>:

$$i_{bv} = \frac{i_{mt}}{1 + \exp\left[\frac{-F(E-E^0)'}{RT}\right] + \frac{m}{k^0} \exp\left[\frac{-F(1-\alpha)(E-E^0)'}{RT}\right]} \quad [4.4]$$

where  $i_{mt}$  is the mass transfer diffusion-limited current,  $F$  is the Faraday constant,  $R$  is the molar gas constant,  $T$  is temperature (K),  $E$  is the applied potential,  $E^0'$  is the formal potential of the redox-couple,  $\alpha$  is the transfer coefficient,  $k^0$  is the standard heterogeneous rate constant ( $\text{cm}\cdot\text{s}^{-1}$ ) and  $m$  is the mass transfer coefficient ( $\text{cm}\cdot\text{s}^{-1}$ ). Equation 4.4 was incorporated in Origin Pro 8.5 as a non-linear least square fit equation employing the Levenberg-Marquandt algorithm. The fitting parameters were the ratio  $k_m$  of the mass transfer coefficient  $m$  and the standard heterogeneous rate constant  $k^0$  ( $k_m = m/k^0$ ),  $\alpha$  which was restricted between 0.3 and 0.7, and  $i_{mt}$ . The mass transfer coefficient may then be expressed as  $m = i_{mt}(AFC^*)^{-1}$ , where  $A$  is the electrode surface area and  $C^*$  is the bulk concentration of the electroactive species. Fixed parameters were  $E^0' = 0.155$  V,  $C^* = 1$  mM and  $A = 2.7 \times 10^{-7}$   $\text{cm}^2$  (3 times the geometric area of a single nanowire). The fits were allowed to resolve until experimental cyclic voltammograms may be described excellently by equation 4.4, i.e., until a correlation factor of  $R^2 \geq 0.999$  was obtained, as shown in Figure 4.6. This was repeated at least three times for every type of electrodes.

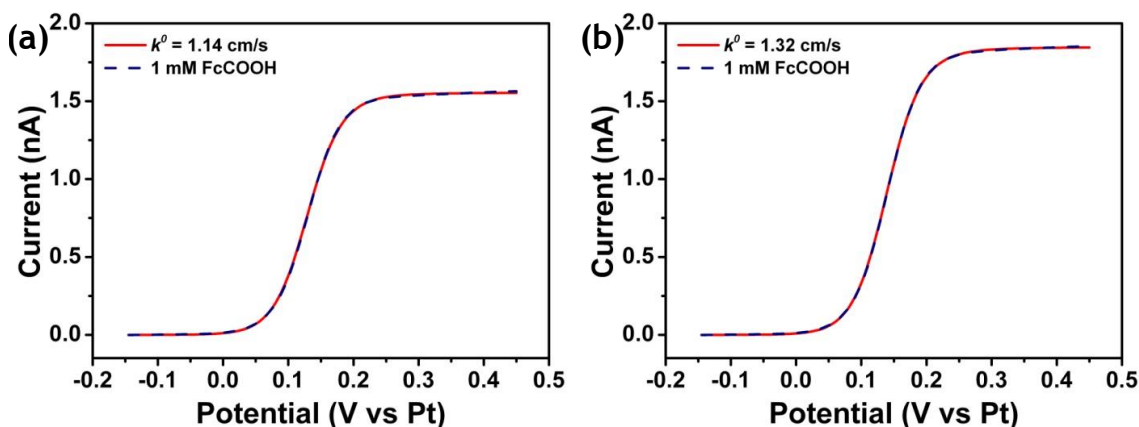


**Figure 4.6:** Fits of Butler-Volmer kinetic equation to experimental cyclic voltammograms obtained for a single electron oxidation of 1 mM FcCOOH in 10 mM PBS at  $5 \text{ mV}\cdot\text{s}^{-1}$  at three nanowire electrodes separated by (a)  $5 \mu\text{m}$  and (b)  $15 \mu\text{m}$ . In both cases  $R^2 = 0.999$ .

Average values of  $k_{m(5\mu\text{m})} = 0.053 \pm 0.020$  and  $k_{m(15\mu\text{m})} = 0.054 \pm 0.015$ ,  $\alpha_{5\mu\text{m}} = 0.58 \pm 0.16$  and  $\alpha_{15\mu\text{m}} = 0.63 \pm 0.09$ , and  $i_{mt(5\mu\text{m})} = 1.55 \pm 0.02$  nA and  $i_{mt(15\mu\text{m})} = 1.85 \pm 0.02$  nA

were extracted from the best generated fits. These values permitted the deduction of the standard heterogeneous rate constant:  $k^0 = i_{\text{mt}}(AFCk_m)^{-1}$ , yielding average values of  $k^0_{(5\mu\text{m})} = 1.14 \pm 0.03 \text{ cm.s}^{-1}$  and  $k^0_{(15\mu\text{m})} = 1.32 \pm 0.03 \text{ cm.s}^{-1}$ . This latter value is in excellent agreement with the average value determined using single (diffusionally independent) nanowires<sup>3</sup>, thereby confirming the diffusional independent nature of the 15  $\mu\text{m}$  spaced arrays. In comparison, the value of  $1.14 \pm 0.03 \text{ cm.s}^{-1}$  is ~12 % lower, which confirms the presence of diffusional overlap at 5  $\mu\text{m}$  spaced arrays.

### 4.3.7 Square Wave Voltammetry at Nanowire Electrode Arrays

In square wave voltammetry, molecules are repeatedly oxidised and reduced as the voltage is pulsed positively and negatively for a series of cycles. During this process, molecules continuously diffuse to and from an electrode surface such that the diffusion layer is not renewed at the beginning of each measurement cycles. Therefore, the initial condition for each cycle is the complex diffusion layer that has evolved from prior pulses. At a single nanowire, the current reaches a maximum around  $E^{0'}$  and then decrease because the cumulative effect of electrolysis through many cycles causes a depletion of species O (or R). By contrast, at nanowire electrode arrays, it is hypothesised that molecules oxidised (or reduced) at one nanowire may diffuse to a neighbouring nanowire rather than to bulk solution so that it may consequently be reduced (or oxidised) during a subsequent voltage step. This should result in more reductive (or oxidative) species at the surface of the electrode between sampling intervals, and consequently in increased signal and higher sensitivity in direct contrast with sweep voltammetry. Furthermore, nanowire arrays with overlapping diffusion profiles should exhibit higher signals as electrodes are closer to each other, thereby reducing the distance for oxidised (or reduced) species to travel from one concentration profile to the neighbouring concentration profile.

To confirm this hypothesis, square wave voltammetric measurements were undertaken for FcCOOH concentrations ranging from 0.1 mM to 5 mM in 10 mM PBS, at single nanowire and at arrays of three nanowires. Figure 4.7 (a) shows typical square wave voltammograms recorded for 5 mM FcCOOH at (i) a single nanowire electrode, (ii) nanowire electrode arrays separated by 5  $\mu\text{m}$  and (iii) nanowire electrode arrays

separated by 15  $\mu\text{m}$ . All recorded signals display current peaks in the voltage range of 0.15 to 0.20 V vs. the on-chip Pt pseudo-reference electrode. Clearly, as expected, an increase in measured current signal was observed when increasing the number of nanowires from one to three within an array; (i) versus (ii) & (iii). Interestingly, a significant increase in signal was observed when the inter-electrode separation is decreased from 15  $\mu\text{m}$  (iii) to 5  $\mu\text{m}$  (ii) confirming that closer nanowire electrodes within an array provide higher signal than nanowire electrodes that are further spaced apart. The signal at arrays with a 5  $\mu\text{m}$  inter-electrode separation is about 3 times higher than that at a single nanowire. The peak currents increased linearly with increasing FcCOOH concentrations. Figure 4.7 (b) shows the calibration plots obtained for FcCOOH concentrations ranging from 0.1 mM to 5 mM in 10 mM PBS for the single nanowire (i) and for the two different nanowire electrode arrays (ii) & (iii) as described above. From these linear relationships and with respect to electrode area, the sensitivity were found to be 5.36  $\text{mA}/\text{cm}^2/\text{mM}$  for a single nanowire, 5.68  $\text{mA}/\text{cm}^2/\text{mM}$  for three nanowires separated by 5  $\mu\text{m}$  and 3.68  $\text{mA}/\text{cm}^2/\text{mM}$  for three nanowires separated by 15  $\mu\text{m}$ .

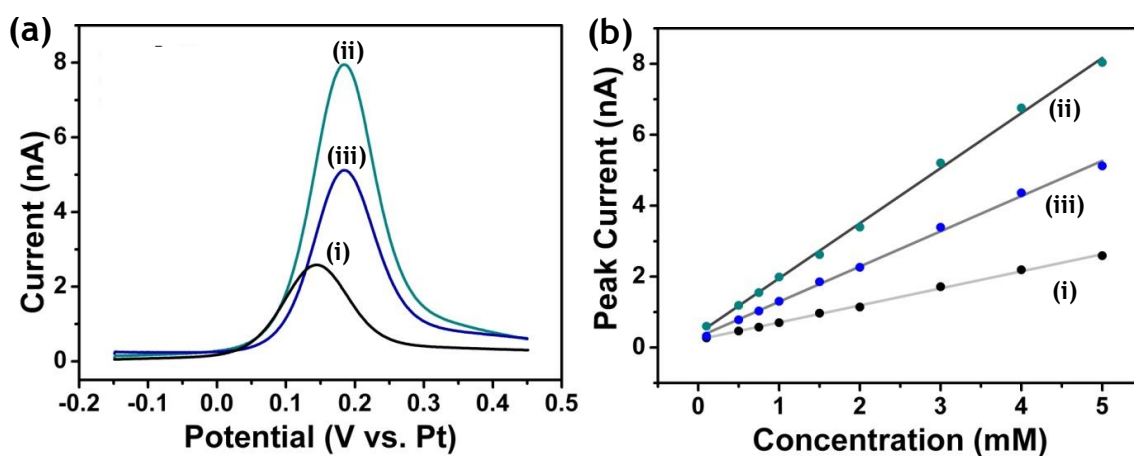


**Figure 4.7:** (a) Typical square wave voltammograms of 5 mM FcCOOH in 10 mM PBS at (i) a single nanowire electrode, (ii) three nanowire electrodes array separated by 5  $\mu\text{m}$  and (iii) three nanowire electrodes array separated by 15  $\mu\text{m}$ . (b) Corresponding calibration plots for a range of FcCOOH concentrations 0.1, 0.5, 0.75, 1, 1.5, 2, 3, 4 & 5 mM in 10 mM PBS,  $R^2 = 0.999$ .

## 4.4 Summary and Conclusion

Nanowire electrode arrays offer the potential for enhancements in electroanalysis including: increased signal-to-noise ratio and increased sensitivity while also allowing quantitative detection at much lower concentrations. However, to achieve this goal a full understanding of the diffusion profiles existing at nanowire arrays would be required. To this end, the effects of altering inter-electrode separations on FcCOOH diffusion for cyclic voltammetry at a very high scan rate ( $5,000 \text{ mV}\cdot\text{s}^{-1}$ ) at arrays of three nanowire electrodes were simulated and then confirmed experimentally. Therefore, in this Chapter, a theoretical and experimental comparative study of the mass transport behaviour at three gold nanowire electrodes is presented. The dimensions of individual nanowires (100 nm wide x 50 nm high x 45  $\mu\text{m}$  long) within an array were the same as that of single nanowires and were fabricated using the same hybrid electron-beam/photolithography process as in Chapter 3. The chip design was the same as previously; it includes twelve gold nanowire working electrode arrays, an on-chip gold counter electrode and an on-chip platinum pseudo reference electrode.

Cyclic voltammetry at these nanowire arrays exhibited measurable currents in the nanoampere regime and displayed steady-state voltammograms even at high scan rates ( $5,000 \text{ mV}\cdot\text{s}^{-1}$ ) indicative of fast analyte mass transport to the electrode. Arrays that are sufficiently spaced so that they have diffusionally independent concentration profiles demonstrated superior electrochemical performance when employing sweep voltammetric techniques compared to arrays with overlapping diffusion profiles. By contrast, arrays with diffusionally overlapping profiles exhibited enhanced performance when employing step voltammetric techniques, e.g., square wave voltammetry. These results show that, to optimise sensitivity in nanoscale electroanalysis the final application needs to be taken into account when initially designing nanoscale electrode arrays. These results are important to nanoscale electroanalysis as they suggest that a ‘design for application’ approach should be adopted prior to electrode fabrication in order to maximise sensitivity. Consequently, this requires either *a priori* knowledge or at least a good appreciation of the diffusion regimes present at nanowire electrodes.

## 4.5 References

1. Shao, Y.; Mirkin, M. V.; Fish, G.; Kokotov, S.; Palanker, D.; Lewis, A., Nanometer-sized electrochemical sensors. *Analytical Chemistry* **1997**, 69, 1627-1634.
2. Conyers, J. L.; White, H. S., Electrochemical characterization of electrodes with submicrometer dimensions. *Analytical chemistry* **2000**, 72, 4441-4446.
3. Dawson, K.; Wahl, A. I.; Murphy, R.; O'Riordan, A., Electroanalysis at Single Gold Nanowire Electrodes. *The Journal of Physical Chemistry C* **2012**, 116, 14665-14673.
4. Guerrette, J. P.; Percival, S. J.; Zhang, B., Voltammetric behavior of gold nanotrench electrodes. *Langmuir* **2011**, 27, 12218-12225.
5. Murray, R. W., Nanoelectrochemistry: metal nanoparticles, nanoelectrodes, and nanopores. *Chemical reviews* **2008**, 108, 2688-2720.
6. Dawson, K.; Wahl, A.; Barry, S.; Barrett, C.; Sassiati, N.; Quinn, A. J.; O'Riordan, A., Fully integrated on-chip nano-electrochemical devices for electroanalytical applications. *Electrochimica Acta* **2014**, 115, 239-246.
7. Arrigan, D. W., Nanoelectrodes, nanoelectrode arrays and their applications. *Analyst* **2004**, 129, 1157-1165.
8. Lanyon, Y. H.; Arrigan, D. W., Recessed nanoband electrodes fabricated by focused ion beam milling. *Sensors and Actuators B: Chemical* **2007**, 121, 341-347.
9. Forrer, P.; Schlottig, F.; Siegenthaler, H.; Textor, M., Electrochemical preparation and surface properties of gold nanowire arrays formed by the template technique. *Journal of Applied Electrochemistry* **2000**, 30, 533-541.
10. Dawson, K.; Strutwolf, J. r.; Rodgers, K. P.; Herzog, G. g.; Arrigan, D. W.; Quinn, A. J.; O'Riordan, A., Single nanoskived nanowires for electrochemical applications. *Analytical chemistry* **2011**, 83, 5535-5540.
11. Berduque, A.; Lanyon, Y. H.; Beni, V.; Herzog, G.; Watson, Y. E.; Rodgers, K.; Stam, F.; Alderman, J.; Arrigan, D. W., Voltammetric characterisation of silicon-based microelectrode arrays and their application to mercury-free stripping voltammetry of copper ions. *Talanta* **2007**, 71, 1022-1030.
12. Cox, J. T.; Zhang, B., Nanoelectrodes: Recent Advances and New Directions. *Annual Review of Analytical Chemistry* **2012**, 5, 253-272.
13. Davies, T. J.; Compton, R. G., The cyclic and linear sweep voltammetry of regular and random arrays of microdisc electrodes: Theory. *Journal of Electroanalytical Chemistry* **2005**, 585, 63-82.

14. Wightman, R. M.; Wipf, D. O., Voltammetry at ultramicroelectrodes. *Electroanalytical chemistry* **1989**, 15, 267-353.
15. Godino, N.; Borriase, X.; Munoz, F. X.; del Campo, F. J.; Compton, R. G., Mass transport to nanoelectrode arrays and limitations of the diffusion domain approach: theory and experiment. *The Journal of Physical Chemistry C* **2009**, 113, 11119-11125.
16. Dawson, K.; Baudequin, M.; Sassiati, N.; Quinn, A. J.; O'Riordan, A., Electroanalysis at discrete arrays of gold nanowire electrodes. *Electrochimica Acta* **2012**.
17. Dawson, K.; Wahl, A.; Pescaglioni, A.; Iacopino, D.; O'Riordan, A., Gold Nanowire Electrode Arrays: Investigations of Non-Faradaic Behavior. *Journal of The Electrochemical Society* **2014**, 161, B3049-B3054.
18. Antiochia, R.; Lavagnini, I.; Magno, F.; Valentini, F.; Palleschi, G., Single-wall carbon nanotube paste electrodes: a comparison with carbon paste, platinum and glassy carbon electrodes via cyclic voltammetric data. *Electroanalysis* **2004**, 16, 1451-1458.
19. Zhang, Y.; Zhou, J.; Lin, L.; Lin, Z., Determination of Electrochemical Electron-Transfer Reaction Standard Rate Constants at Nanoelectrodes: Standard Rate Constants for Ferrocenylmethyltrimethylammonium (III)/(II) and Hexacyanoferrate (III)/(II). *Electroanalysis* **2008**, 20, 1490-1494.
20. Watkins, J. J.; Chen, J.; White, H. S.; Abruña, H. D.; Maisonhaute, E.; Amatore, C., Zeptomole voltammetric detection and electron-transfer rate measurements using platinum electrodes of nanometer dimensions. *Analytical chemistry* **2003**, 75, 3962-3971.
21. Watkins, J. J.; White, H. S., The role of the electrical double layer and ion pairing on the electrochemical oxidation of hexachloroiridate (III) at Pt electrodes of nanometer dimensions. *Langmuir* **2004**, 20, 5474-5483.
22. Heller, I.; Kong, J.; Heering, H. A.; Williams, K. A.; Lemay, S. G.; Dekker, C., Individual single-walled carbon nanotubes as nanoelectrodes for electrochemistry. *Nano letters* **2005**, 5, 137-142.

*Chapter 5*

**Diffusionally Independent Nanowire Arrays**



## 5.1 Introduction

As discussed in previous chapters, nanoelectrodes are the next step towards the miniaturisation of sensors based on electrochemical detection techniques<sup>1-3</sup>. Previously, the main limitation is the unavailability of effective and reproducible fabrication techniques, which consequently restricts the assessment and understanding of nanoelectrode electrochemical performance. In the last few decades, a wide range of methodologies have been developed, such as template electrodeposition<sup>4</sup>, nanoskiving<sup>5</sup>, vapour-liquid-solid growth<sup>6</sup> or chemical vapour deposition<sup>7</sup>, but all these techniques are quite challenging, have poor yield and poor reproducibility, lack of integration methods and/or are time-consuming. For instance, in Chapter 2, we discussed the issues associated with the fabrication of ultra-long metal nanowires by template electrodeposition.

Conversely, recent advances have made possible the fabrication of robust and reproducible nanoelectrodes<sup>8-11</sup>. In particular, electron-beam lithography allows for the fast preparation of high yield and highly reproducible nanostructures, thereby making it an interesting platform for the development of nanowire-based sensing devices<sup>12-15</sup>. As a result, it is possible to truthfully benchmark and further understand nanowires electrochemical capabilities versus commercially available and widely used larger electrodes. In Chapter 3, individual gold nanowire electrodes fabricated on silicon chips by electron-beam lithography and contacted using photolithography, demonstrated enhanced performance compared to commercial gold ultra-microdisc electrodes due to improved mass transport occurring at the nanoscale. This enhanced mass transport comes predominantly from radial diffusion at the nanoscale. Furthermore, to ensure this is the case at nanowire electrode arrays, under the same experimental conditions, each nanowire must be sufficiently spatially resolved to allow independent radial analyte diffusion profiles to form at each electrode. In Chapter 4, we have shown that diffusion layers of neighbouring nanowire electrodes overlap with a 10  $\mu\text{m}$  inter-electrode distance, whereas individual diffusion layers were observed at nanowire electrodes separated by 15  $\mu\text{m}$ . Nanowires within these arrays were of the same dimensions as the single nanowires employed in Chapter 3.

In this chapter, based on results in Chapter 4, we undertook finite element analysis of diffusion profiles existing at arrays of nanowire electrodes with Comsol Multiphysics® to optimise the inter-electrode distance required to allow independent diffusional mass transport to each nanowire electrodes, under cyclic voltammetry at  $5000 \text{ mV.s}^{-1}$ . To confirm our simulations, we once again employed the hybrid electron-beam/photolithography technique to fabricate and fully integrate single nanowire and nanowire arrays on silicon chips, as described in Chapters 3 and 4. These devices include twelve separate electron-beam fields containing single nanowires and arrays of two, three and four nanowire electrodes, an on-chip gold counter electrode, an on-chip platinum pseudo-reference electrode and peripheral contact pads to facilitate direct electrical and electrochemical probing. Arrays were designed to possess sufficient inter-nanowire spacing ( $13 \mu\text{m}$ ) so as to prevent overlap of diffusion layers of adjacent nanowire electrodes at  $5,000 \text{ mV.s}^{-1}$ . Critical dimensions of individual nanowires were characterised using a combination of optical, scanning electron and atomic force microscopies. Electrochemical characterisation of the electrodes was undertaken to explore the diffusional process occurring at arrays with increasing number of nanowires. We show that experimental results are in excellent agreement with simulated results. Furthermore, single nanowire display steady-state behaviour up to  $50,000 \text{ mV.s}^{-1}$ . Nanowires separated by  $13 \mu\text{m}$  are diffusional independent for scan rates ranging from  $5,000$  up to  $50,000 \text{ mV.s}^{-1}$ ; the currents are a multiple of that at a single nanowire. However, large charging currents were observed at nanowires due to the high electric fields associated with metal interconnection tracks, rather than from the nanowires.

## 5.2 Experimental

### 5.2.1 Finite-Element Simulations

Same as previously, see subsection 3.2.7, concentration profiles for the oxidation of FcCOOH at single nanowire electrode and arrays containing two, three or four nanowires electrodes were simulated using the ‘transport of diluted species’ modelling platform in the ‘chemical species transport’ module comprised in the commercial finite element software package Comsol Multiphysics<sup>®</sup> 4.1. (Comsol, SE). The objective of these simulations is to optimise the distance required between adjacent nanowires to allow independent diffusional mass transport to each nanowire electrodes, at high scan rates using cyclic voltammetry, based on results in Chapter 4. Simulations were carried out prior to electrode fabrication.

### 5.2.2 Nanowire Electrode Array Design, Fabrication and Cell Set-up

As mentioned before, electron-beam lithography masks are software based so that patterns can be easily altered. The chip layout and fabrication approach employed in Chapters 3 was used again. The mask design was changed such that individual nanowire electrodes as well as arrays of two, three and four nanowire electrodes separated by 13  $\mu\text{m}$  were patterned into the twelve different central 80  $\mu\text{m}$  x 80  $\mu\text{m}$  electron-beam fields of each silicon chip. The same hybrid process was employed, whereby only the nanowire structures were defined by electron-beam lithography and photolithography was employed to overlay interconnection tracks, as well as an on-chip gold counter electrode, an on-chip platinum pseudo-reference electrode and peripheral contact pads; a passivation layer selectively insulated these structures. Following fabrication, wafers were diced into 16 x 16 mm chips, which were then mounted in the same electrochemical cell set-up employed in the previous Chapter.

### 5.2.3 Nanowire Structural and Electrical Characterisation

Optical micrographs were again acquired using a calibrated microscope (Axioskop II, Carl Zeiss Ltd.) equipped with a charge-coupled detector camera (CCD; DEI-750, Optronics). Structural characterisation was undertaken using a field emission scanning

electron microscope (JSM-6700F, JEOL UK Ltd.) operating at beam voltages between 5 and 10 kV. As a quality control check and to confirm electrical functionality, two-point electrical measurements were performed using a probe station (Model 6200, Micromanipulator Probe Station) in combination with a source meter (Keithly 2400) and a dedicated LabVIEW™ V8.0 program. In these current-voltage measurements, the source electrode was grounded, a bias sweep up to  $\pm 10$  mV was applied to the drain electrode, and the current through the nanowires was measured.

#### 5.2.4 Electrochemical analysis

All electrochemical studies were performed using a CHI660A Electrochemical Analyser and Faraday Cage CHI200B (CH Instruments). All experiments were performed in a home-made cell with a typical sample volume of  $\sim 150$   $\mu\text{L}$ , employing single gold nanowire electrode or gold nanowire arrays working electrodes, versus on-chip gold counter electrode and platinum pseudo-reference electrode. Cyclic voltammetry was conducted in 1 mM ferrocene monocarboxylic acid in 10 mM phosphate buffer saline solution, pH 7.4 and deaerated with nitrogen gas, in the voltage range of -0.15 V to 0.45 V, for a variety of scan rates from 20 to 50,000  $\text{mV}\cdot\text{s}^{-1}$  (maximum possible scan rate according to instrument specifications). Prior to electrochemical experiments, electrodes were cleaned by sequential immersion of chips for 10 minutes in acetone (bath 1), trichloroethylene, acetone (bath 2), and isopropyl alcohol, followed by a thorough rinse with deionised water and dried in a stream of filtered nitrogen.

#### 5.2.5 Chemicals and Glassware

Unless otherwise stated, all chemicals were purchased from Sigma-Aldrich and were used as received. All solutions were freshly prepared on a weekly basis with deionised water of resistivity 18.2  $\text{M}\Omega\cdot\text{cm}$  (Millipore Q).

## 5.3 Results and discussion

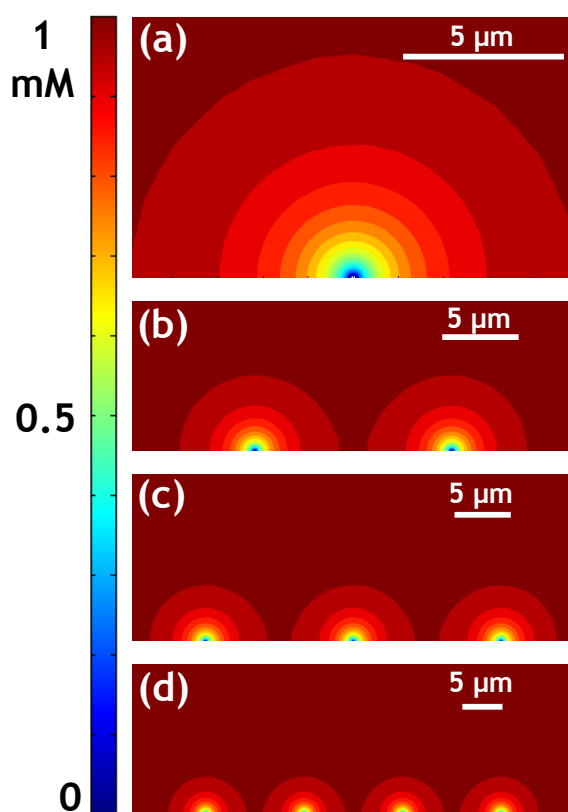
### 5.3.1 Simulation at Nanowire Electrode Arrays: Optimisation of the Inter-electrode Separation

Simulations were undertaken again using a simplified two dimensional model known as the diffusion domain approach was adopted. In brief, each nanowire was outlined by a 50 nm x 100 nm rectangle (height x width) located centrally at the bottom of a much larger rectangle (space domain), with an inter-electrode distance varying between 10 and 15  $\mu\text{m}$  for arrays. To ensure accuracy of the simulations, the domain area is selected so as to be large enough to ensure bulk-like conditions at the boundaries remain unaffected by the electrochemistry occurring at the electrodes. During simulations the mesh was duly refined and simulations were allowed to iteratively resolve until a convergence error less than 2% was achieved.

In Chapter 3, radial diffusion of 1 mM FcCOOH in 10 mM PBS was demonstrated at single gold nanowires (50 nm x 100 nm x 45  $\mu\text{m}$ ) using cyclic voltammetry for scan rates up to 20,000  $\text{mV}\cdot\text{s}^{-1}$ . This permits rapid analyte transport and ideal steady-state responses. To ensure this is the case at nanowire electrode arrays, under the same experimental conditions, each nanowire must be sufficiently spatially resolved to allow independent radial analyte diffusion profiles to form at each electrode. In Chapter 4, for nanowire arrays (50 nm x 100 nm x 45  $\mu\text{m}$ ), diffusion layers of neighbouring nanowire electrodes were shown to overlap with a 10  $\mu\text{m}$  inter-electrode distance, whereas individual diffusion layers were observed at nanowire electrodes separated by 15  $\mu\text{m}$ .

In this Chapter, the objective is to optimise the distance where diffusional independence occurs, and apply it to arrays of two, three and four nanowire electrodes. Models were built to reflect the diffusion of 1 mM ferrocene monocarboxylic acid in 10 mM phosphate buffer saline solution at nanowire arrays during an experiment where the potential was swept from -0.15 V to 0.45 V at 5000  $\text{mV}\cdot\text{s}^{-1}$ . The nanowire dimensions were maintained as 100 nm in width and 50 nm in height with  $D_R = 5.4 \times 10^{-6} \text{ cm}^2\cdot\text{s}^{-1}$ ,  $E^0 = 0.155 \text{ V}$ ,  $T = 298.15 \text{ K}$ . Within the limitations of the software package, a separation of 13  $\mu\text{m}$  was found to be the minimum distance allowing independent radial diffusion at each nanowire electrode in an array.

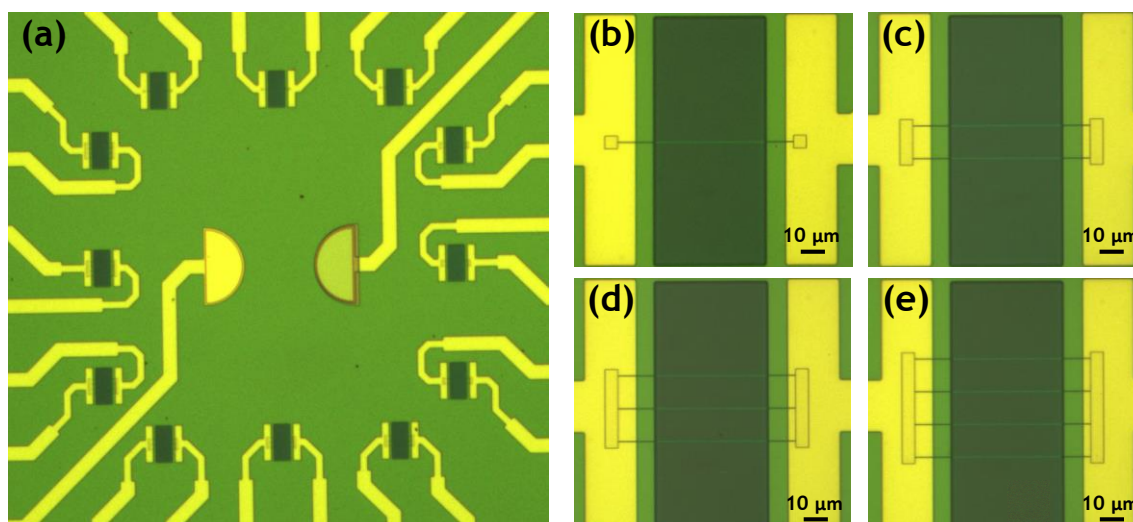
As discussed in Chapter 3 and shown here in Figure 5.1 (a), the diffusion layer thickness at a single nanowire is uniform and much larger than the nanowire width, which strongly suggests that analyte mass transport behaviour is dominated by radial diffusion. As can be seen in Figures 5.1 (b) to (d), the diffusion layers at each nanowire electrode separated by 13  $\mu\text{m}$  within an array of respectively two, three and four nanowires are much larger than the nanowire width and completely independent from each other. Moreover the thickness of the individual diffusion layers is consistent with the thickness of the diffusion layer at a single nanowire. This suggests that each nanowire electrode behaves as an individual electrode and that the current response of the whole array should be equivalent to that of a single nanowire multiplied by the number of nanowires in the array, for a scan rate of  $5,000 \text{ mV}\cdot\text{s}^{-1}$  and possibly higher. It is also expected that for lower scan rates, the current at array would be lower than that of a multiple of the current at a single nanowire.



**Figure 5.1:** 2D simulations of FcCOOH concentration profiles normal to (a) a single nanowire electrode, and arrays of (b) two, (c) three and (d) four nanowire electrodes separated by 13  $\mu\text{m}$ . Nanowires are 50 nm in height and 100 nm in width.  $C_R^* = 1 \text{ mM}$  in 10 mM PBS,  $\nu = 5,000 \text{ mV}\cdot\text{s}^{-1}$ ,  $D_R = 5.4 \times 10^{-6} \text{ cm}^2\cdot\text{s}^{-1}$ ,  $E^{0'} = 0.155 \text{ V}$ ,  $T = 298.15 \text{ K}$ .

### 5.3.2 Nanowire Electrodes Fabrication and Structural Characterisation

To confirm simulation results, single gold nanowire electrodes and arrays of two, three and four nanowire electrodes were fabricated using a hybrid electron beam/photolithography process at Si/SiO<sub>2</sub> substrates, as described in the experimental section. Following fabrication, electrodes were structurally characterised using optical, scanning electron and atomic force microscopies.



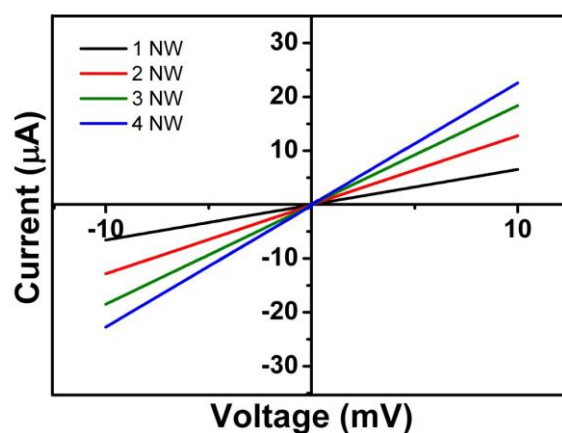
**Figure 5.2:** (a) Optical micrograph of the central field of a fully fabricated chip comprising twelve individually electrically contacted gold nanowire working electrode devices, a gold counter electrode (centre left), a platinum reference electrode (centre right), and interconnection tracks. High magnification optical micrographs of fully integrated and passivated (b) single nanowire electrode, and array of (c) two, (d) three and (e) four nanowire electrodes separated by 13  $\mu\text{m}$ , with overlaid electrical contact electrodes and silicon nitride passivation. The darker rectangle in the middle corresponds to the trench selectively opened in the passivation layer above the nanowire electrodes to allow contact with an electrolyte solution.

Figure 5.2 (a) shows an optical micrograph at the centre of a fully fabricated on-chip electrochemical cell. It comprises twelve individually addressable discrete working electrode devices, which population range from a single gold nanowire to four gold nanowires in array, as well as a gold counter electrode (left) and a platinum pseudo-reference electrode (right). Figures 5.2 (b) to (e) respectively are optical micrographs of fully fabricated, integrated and passivated single nanowire and arrays of two, three and four nanowire electrodes separated by 13  $\mu\text{m}$ . The gold squares or bars at both nanowire termini were defined during the electron-beam lithography step to enhance electrical contact with overlaid metallic interconnection tracks. The dimensions of the passivation window (central dark rectangle) defined the electrode length; typically fabricated nanowires have an exposed length of  $\sim 45 \mu\text{m}$ . Same as previously, visual

inspection using scanning electron microscopy clearly showed that the silicon nitride layer was fully removed from the entire target area, thereby exposing the underlying nanowire electrodes. The fabrication process was found to be highly reproducible with an average width of  $98 \pm 5$  nm and an average height of  $50.6 \pm 0.8$  nm. This is very consistent with the average values obtained in Chapters 3 and 4. Once again, this demonstrates that the fabrication process is very reproducible such that there is very little to no variation in nanowires dimensions form chip to chip and batch to batch.

### 5.3.3 Nanowire Electrodes Electrical Characterisation

As before, electrical characterisation was performed using standard two-point current-voltage measurements to ensure fully fabricated nanowire electrode devices were functional and defect free prior to electroanalysis. This was done by contacting the two contact pads related to a nanowire device to two individual measuring probes. All functioning devices displayed ohmic linear and very reproducible responses confirming excellent electrical contact to the electrodes by the overlaid interconnection tracks.



**Figure 5.3:** Two point current-voltage characteristics measured for typical fully integrated and packaged single nanowire electrodes and arrays of two, three and four nanowires separated by  $13 \mu\text{m}$  exhibiting ohmic behaviour.

It was observed that the measured resistance decreased with increasing nanowire population, which is consistent with the increase in number of conductive pathways:  $1323 \pm 79 \Omega$  ( $n = 15$ ) for a single nanowire,  $729 \pm 60 \Omega$  ( $n = 15$ ) for two nanowires,  $527 \pm 55 \Omega$  ( $n = 15$ ) for three nanowires and  $426 \pm 46 \Omega$  ( $n = 15$ ) for four nanowires; see Figure 5.3. For each type of nanowire devices, the small variations observed in the resistance correspond to the small variations in the critical dimensions. Control

electrical measurements were obtained in the absence of nanowire devices, yielding very high resistances ( $\sim 10\text{ G}\Omega$ ) typical of an open circuit. This confirmed that the observed ohmic behaviour of the nanowire devices was exclusively due to the nanowires and associated on-chip metal interconnection tracks with no contribution from the underlying silicon oxide layer. Nanowire devices that exhibited non-ohmic behaviour or high resistance indicative of an open circuit behaviour were discarded.

The resistances obtained for single nanowire electrodes in this Chapter are the same (within experimental error) as described previously. These values are also in excellent agreement with those published elsewhere<sup>16, 17</sup>. This further confirms the high reproducibility of the fabrication method.

### 5.3.4 Cyclic Voltammetry at Nanowire Electrode Arrays: Optimisation of the Inter-electrode Separation

Following fabrication and characterisation, cyclic voltammetry experiments corresponding to the simulations presented in Figure 5.1 were performed. Typical cyclic voltammograms acquired at a single nanowire and at arrays of two, three and four nanowires in 1 mM FcCOOH in 10 mM PBS at  $5000\text{ mV}\cdot\text{s}^{-1}$  are presented in Figure 5.4. Both the forward and backward sweeps of voltammograms were observed to be sigmoidal and exhibited steady-state currents, as expected. These data strongly suggest that electrodes within an array are fully diffusionally independent at  $5,000\text{ mV}\cdot\text{s}^{-1}$ .

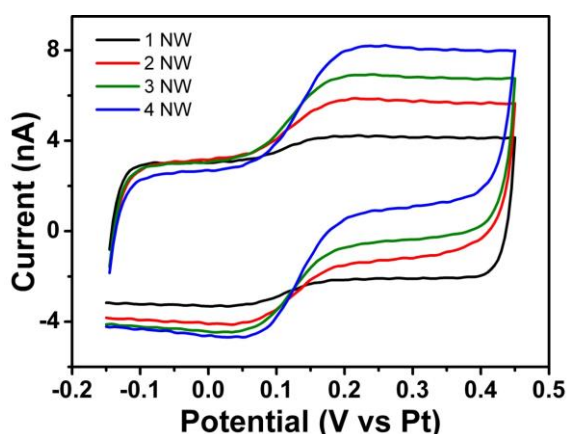


**Figure 5.4:** Cyclic voltammograms at a single nanowire and arrays of two, three and four nanowires separated by  $13\ \mu\text{m}$ , obtained at a  $5,000\text{ mV}\cdot\text{s}^{-1}$  scan rate in 1 mM FcCOOH in 10 mM PBS.

### 5.3.5 Signal Enhancement at Nanowire Arrays vs. Single Nanowire

In Chapter 3, cyclic voltammograms at single nanowire electrodes were recorded in 1 mM FcCOOH in 10 mM PBS solution at scan rates ranging from 20 to 20,000  $\text{mV}\cdot\text{s}^{-1}$ . It was proposed that the measured current may be expressed as follows:

$$i_{\text{measured}} = C_{dl}v + i_{ss(\text{nanowire})} \quad [3.12]$$

where  $C_{dl}$  is the overall capacitance and  $i_{ss(\text{nanowire})}$  is the nanowire steady-state current. The capacitance and the steady state current were found to respectively be  $0.65 \pm 0.16$  nF and  $1.15 \pm 0.22$  nA. As mentioned in Chapter 4, for diffusionally independent nanowire electrodes within an array, the faradaic current should be the same as a single electrode multiplied by the number  $N$  of nanowires in the array, such that the measured current may be expressed as:

$$i_{\text{measured}} = C_{dl}v + N i_{ss(\text{nanowire})} \quad [5.2]$$

We have also previously demonstrated that the overall capacitance is the same for nanowire and nanowire arrays, i.e.,  $0.65 \pm 0.16$  nF. As such, the estimated current at a single nanowire and at arrays of two, three or four diffusionally independent nanowire electrodes at  $5000 \text{ mV}\cdot\text{s}^{-1}$  respectively are around: 4.40 nA, 5.55 nA, 6.70 nA and 7.85 nA. For nanowires with overlapping diffusion profiles, the current is expected to be lower than these values, respectively.

Experimentally, the magnitude of the steady-state currents at  $5,000 \text{ mV}\cdot\text{s}^{-1}$  for all nanowire electrodes devices was found to be highly reproducible from separate devices on different chips ( $n = 15$ ):  $4.54 \pm 0.26$  nA for single nanowire,  $5.82 \pm 0.38$  nA for two nanowires,  $6.96 \pm 0.67$  nA for three nanowires and  $8.14 \pm 1.23$  nA for four nanowires. These average measured currents are the same (within experimental error) as their respective expected values. It is therefore likely the case that the increase in observed current arises from improved mass transport, i.e., nanowires are diffusionally independent. By subtracting the contribution of the average charging currents ( $C_{dl}v = 3.25$  nA) from the overall average measured steady-state currents, the average faradaic peak currents were found to be: 1.29 nA for a single nanowire, 2.57 nA for two nanowires, 3.71 nA for three nanowires and 4.89 nA for four nanowires. It is clear that the faradaic current at each nanowire array is a multiple of that at a single nanowire, thereby confirming the diffusional independence of each nanowire within the array.

### 5.3.6 Ultra-Rapid Analysis at Nanowire and Nanowire Arrays

Cyclic voltammograms were also recorded at single and arrays of two, three and four nanowire electrodes in 1 mM FcCOOH in 10 mM PBS for scan rates ranging from 20  $\text{mV}\cdot\text{s}^{-1}$  up to 50,000  $\text{mV}\cdot\text{s}^{-1}$  (fastest instrument capability). Figures 5.5 (a), (d), (g) and (j) respectively show typical responses acquired at a single nanowire and at arrays of two, three and four nanowires. Although the faradaic signals were swamped by the capacitive charging currents, all cyclic voltammograms displayed sigmoidal and exhibited highly reproducible steady-state responses.

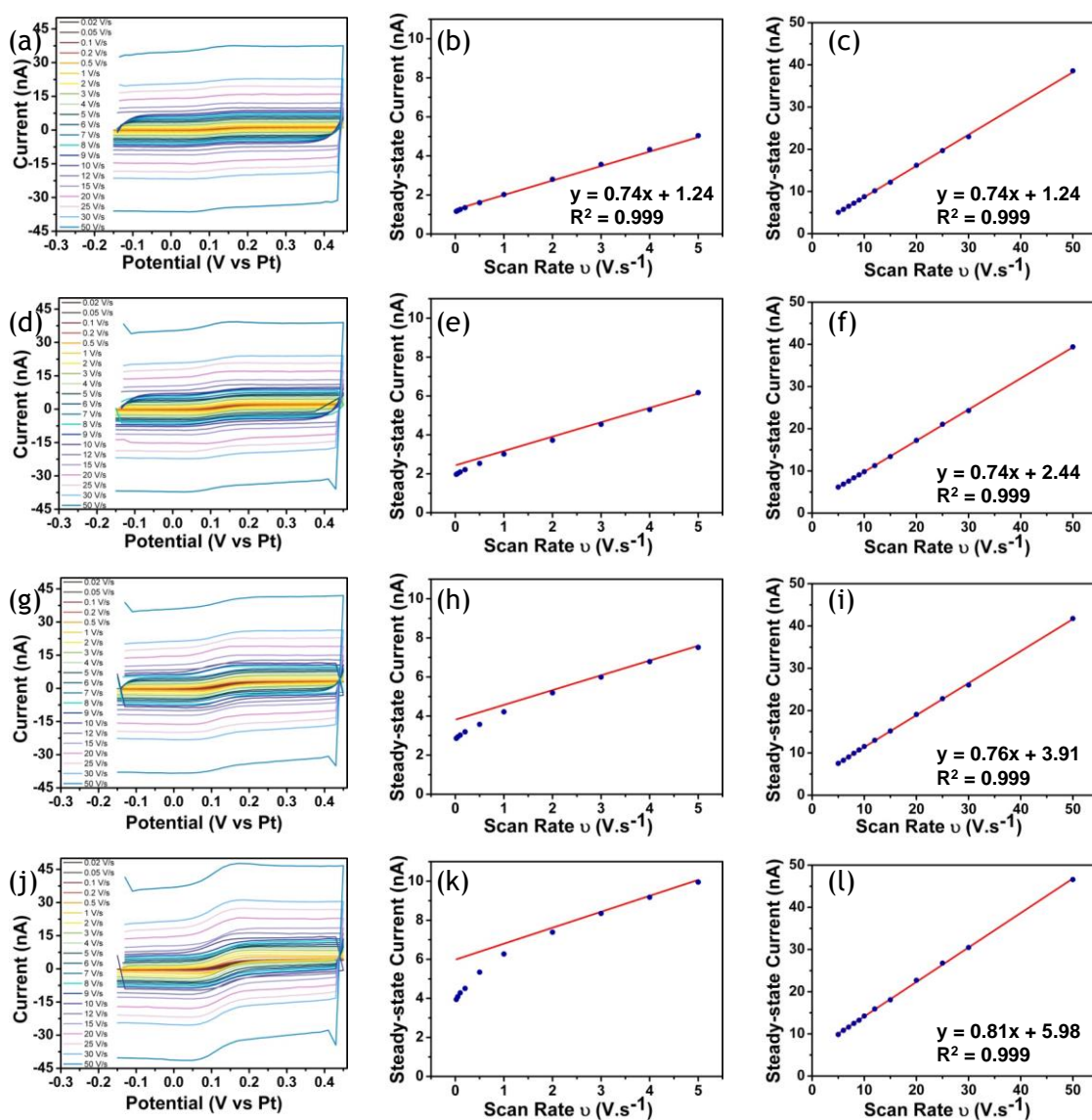


**Figure 5.5:** (a) Typical cyclic voltammograms obtained at a single nanowire in 1 mM FcCOOH in 10 mM PBS for scan rates ranging from 20 up to 50,000  $\text{mV}\cdot\text{s}^{-1}$ . (b) Plot of steady-state currents at a single nanowire versus scan rates between 20 and 5,000  $\text{mV}\cdot\text{s}^{-1}$ . (c) Plot of steady-state currents at a single nanowire versus scan rates between 5,000 and 50,000  $\text{mV}\cdot\text{s}^{-1}$ . (d), (e) and (f) are the equivalent for an array of two nanowires. (g), (h) and (i) are the equivalent for an arrays of three nanowires. (j), (k) and (l) are the equivalent for an array of four nanowires. All red lines are based on equation 5.2.

At a single nanowire, as expected, the measured currents were found to increase linearly with increasing scan rates, from 20 up to 50,000  $\text{mV}\cdot\text{s}^{-1}$ , as shown in Figures 5.5 (b) and (c). In this case, the capacitance is 0.74 nF and the steady-state current is 1.24 nA. These values are in very good agreement with the average experimental values. This strongly suggests that the analyte mass transport behaviour to a nanowire electrode is radial and does not change regardless of the analysis time such that the currents reach a time-independent steady state value, arising from the very small critical dimension of the nanowire electrode. These data agree with the simulated concentration profile and with results presented in Chapter 3. A cyclic sweep at 50,000  $\text{mV}\cdot\text{s}^{-1}$  takes approximately 20-30 ms (depending on the potential window) without the loss of the steady-state and time-independent current behaviour, thereby reducing analysis time by a factor up to 750 compared to ultra-microdisc electrodes. Thus ultra-rapid signal acquisition, which is critical for sensing applications, is possible with electron-beam lithography fabricated single nanowires.

At an array of two nanowires, the measured currents (data points) were found to be lower than the expected values (line based on equation 5.2) for scan rates ranging from 20 to 5,000  $\text{mV}\cdot\text{s}^{-1}$ , see Figure 5.5 (e). This shows diffusional overlap between neighbouring diffusion layers resulting in non-linear behaviour. With increasing scan rate, the degree of overlap lessens and the measured values become progressively closer to the expected values. Above 5,000  $\text{mV}\cdot\text{s}^{-1}$ , the measured currents increased linearly with increasing scan rates up to 50,000  $\text{mV}\cdot\text{s}^{-1}$ , as expected, see Figure 5.5 (f). This clearly shows independent diffusion layers are forming at each nanowire. In this example, the capacitance is 0.74 nF and the steady-state current is 2.44 nA. These values are in very good agreement with the average experimental values and consistent with that of a single nanowire. This behaviour was even more apparent at arrays of three and four nanowires; with respectively capacitances of 0.76 and 0.81 nF, and steady-state currents of 3.91 and 5.98 nA. Note that at the array of four nanowires, the capacitance is slightly higher compared to that at the single nanowire and to the arrays of two and three nanowires; this could be due to shorter interconnection tracks. The steady-state current is also a bit more than four times that at a single nanowire, maybe due to the fact that the outer nanowires are closer to the edges in the opening window in the passivation layer.

Consequently, diffusionally independent nanowires contained in an array allow for the employment of significantly high analysis rates with linear increase of the faradaic signal with increasing number of nanowire electrodes, such that the signal acquired within 20-30 ms can be multiplied by a factor of 2 or more.  $50,000 \text{ mV}\cdot\text{s}^{-1}$  is the fastest scan rate in the instrument, there may be diffusional independence at even higher scan rates. Work is now on-going to block or eliminate the capacitive currents associated with the interconnection tracks by the inclusion of an on-chip faradaic shield in order to permit even faster analysis.

## 5.4 Summary and Conclusion

As discussed before, nanowire electrode arrays offer the potential for enhancements in electroanalysis including: increased signal-to-noise ratio and increased sensitivity while also allowing quantitative detection at much lower concentrations. In this Chapter, the distance where diffusional independence occurs under sweep voltammetric conditions was optimised to 13  $\mu\text{m}$  based on results presented in Chapter 4. Single nanowire as well as arrays of two, three and four nanowire electrodes (100 nm wide x 50 nm high x 45  $\mu\text{m}$  long) separated by 13  $\mu\text{m}$  were fabricated by using again the hybrid electron-beam/photolithography process. The chip design was the same as previously; it includes twelve gold nanowire working electrode arrays, an on-chip gold counter electrode and an on-chip platinum pseudo reference electrode.

Experimental results were in excellent agreement with simulated results. Single nanowire display steady-state behaviour up to 50,000  $\text{mV}\cdot\text{s}^{-1}$ , thereby reducing the analysis time down to 20-30 ms (depending on the potential window). Compared to ultra-microdisc electrode, this constitutes a decrease in analysis time by a factor up to 750. Furthermore, nanowires separated by 13  $\mu\text{m}$  are diffusional independent for scan rates ranging from 5,000 up to 50,000  $\text{mV}\cdot\text{s}^{-1}$  and the faradaic currents are a multiple of that at a single nanowire, such that the signal acquired within 20-30 ms can be multiplied by a factor of 2 or more. However, large charging currents were observed at nanowires due to the high electric fields associated with metal interconnection tracks, rather than from the nanowires.

## 5.5 References

1. Koehne, J. E.; Chen, H.; Cassell, A. M.; Ye, Q.; Han, J.; Meyyappan, M.; Li, J., Miniaturized multiplex label-free electronic chip for rapid nucleic acid analysis based on carbon nanotube nanoelectrode arrays. *Clinical chemistry* **2004**, 50, 1886-1893.
2. Arrigan, D. W., Nanoelectrodes, nanoelectrode arrays and their applications. *Analyst* **2004**, 129, 1157-1165.
3. Sablon, K., Nanoelectrodes for molecular devices: a controllable fabrication. *Nanoscale Research Letters* **2008**, 3, 268-270.
4. Forrer, P.; Schlottig, F.; Siegenthaler, H.; Textor, M., Electrochemical preparation and surface properties of gold nanowire arrays formed by the template technique. *Journal of Applied Electrochemistry* **2000**, 30, 533-541.
5. Dawson, K.; Strutwolf, J. r.; Rodgers, K. P.; Herzog, G. g.; Arrigan, D. W.; Quinn, A. J.; O'Riordan, A., Single nanoskived nanowires for electrochemical applications. *Analytical chemistry* **2011**, 83, 5535-5540.
6. Mårtensson, T.; Borgström, M.; Seifert, W.; Ohlsson, B.; Samuelson, L., Fabrication of individually seeded nanowire arrays by vapour-liquid-solid growth. *Nanotechnology* **2003**, 14, 1255.
7. Iacopi, F.; Vereecken, P.; Schaekers, M.; Caymax, M.; Moelans, N.; Blanpain, B.; Richard, O.; Detavernier, C.; Griffiths, H., Plasma-enhanced chemical vapour deposition growth of Si nanowires with low melting point metal catalysts: an effective alternative to Au-mediated growth. *Nanotechnology* **2007**, 18, 505307.
8. Gamo, K., Recent advances of focused ion beam technology. *Nuclear Instruments and Methods in Physics Research Section B: Beam Interactions with Materials and Atoms* **1997**, 121, 464-469.
9. Quake, S. R.; Scherer, A., From micro-to nanofabrication with soft materials. *Science* **2000**, 290, 1536-1540.
10. Gates, B. D.; Xu, Q.; Stewart, M.; Ryan, D.; Willson, C. G.; Whitesides, G. M., New approaches to nanofabrication: molding, printing, and other techniques. *Chemical reviews* **2005**, 105, 1171-1196.
11. Chen, Y.; Pepin, A., Nanofabrication: Conventional and nonconventional methods. *Electrophoresis* **2001**, 22, 187-207.
12. Contreras, A. M.; Grunes, J.; Yan, X.-M.; Liddle, A.; Somorjai, G., Fabrication of platinum nanoparticles and nanowires by electron beam lithography (EBL) and nanoimprint lithography (NIL): comparison of ethylene hydrogenation kinetics. *Catalysis letters* **2005**, 100, 115-124.

13. Pease, R., Electron beam lithography. *Contemporary Physics* **1981**, 22, 265-290.
14. Hu, W.; Sarveswaran, K.; Lieberman, M.; Bernstein, G. H., High-resolution electron beam lithography and DNA nano-patterning for molecular QCA. *Nanotechnology, IEEE Transactions on* **2005**, 4, 312-316.
15. Tseng, A. A.; Chen, K.; Chen, C. D.; Ma, K. J., Electron beam lithography in nanoscale fabrication: recent development. *Electronics Packaging Manufacturing, IEEE Transactions on* **2003**, 26, 141-149.
16. Dawson, K.; Wahl, A. I.; Murphy, R.; O'Riordan, A., Electroanalysis at Single Gold Nanowire Electrodes. *The Journal of Physical Chemistry C* **2012**, 116, 14665-14673.
17. Dawson, K.; Baudequin, M.; Sassiati, N.; Quinn, A. J.; O'Riordan, A., Electroanalysis at discrete arrays of gold nanowire electrodes. *Electrochimica Acta* **2012**.

## **Appendices**



## A1. Abbreviations and Acronyms

1-D	1-Dimensional
2-D	2-Dimensional
3-D	3-Dimensional
AAO	Anodic Alumina Oxide
AFM	Atomic Force Microscopy
Ag/AgCl	Silver/Silver Chloride
Au	Gold
CV	Cyclic Voltammetry
D	Diffusion Coefficient
E	Applied potential
$E^{0'}$	Formal potential of a redox couple
$E_{eq}$	Equilibrium potential
EBL	Electron Beam Lithography
FcCOOH	Ferrocenemonocarboxylic Acid
FIB	Focussed Ion Beam
HOMO	Highest Occupied Molecular Orbital
<i>I-V</i>	Current-Voltage
$k_0$	Standard heterogeneous rate constant
LPNE	Lithographically Patterned Nanowire Electrodeposition
LUMO	Lowest Unoccupied Molecular Orbital
MWCNT	Multi-Walled Carbon Nanotube
NW	Nanowire
PBS	Phosphate Buffered Saline
PCB	Printed Circuit Board
PDMS	Polydimethylsiloxane
PECVD	Plasma-Enhanced Chemical Vapour Deposition
Pt	Platinum
PTFE	Polytetrafluoroethylene
PVD	Physical Vapour Deposition
rpm	Rotation per Minute

S/N	Signal To Noise
SEM	Scanning Electron Microscopy
SiN	Silicon Nitride
SWCNT	Single-Walled Carbon Nanotube
SWV	Square Wave Voltammetry
Ti	Titanium

## A2. Data

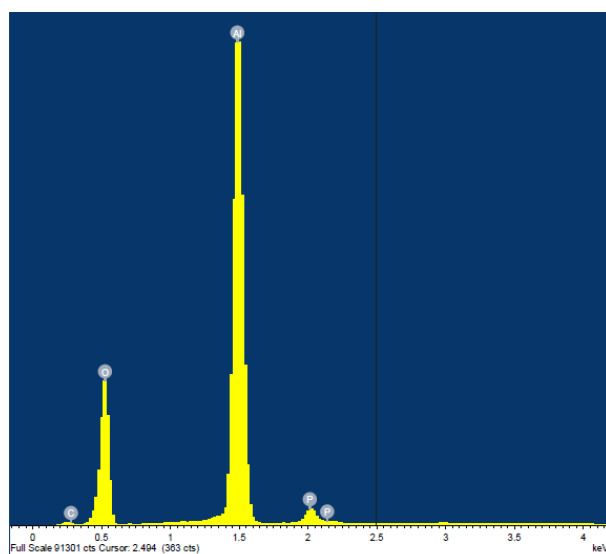


**Figure A.1:** Energy-dispersive X-ray spectrum taken on an empty AAO membrane

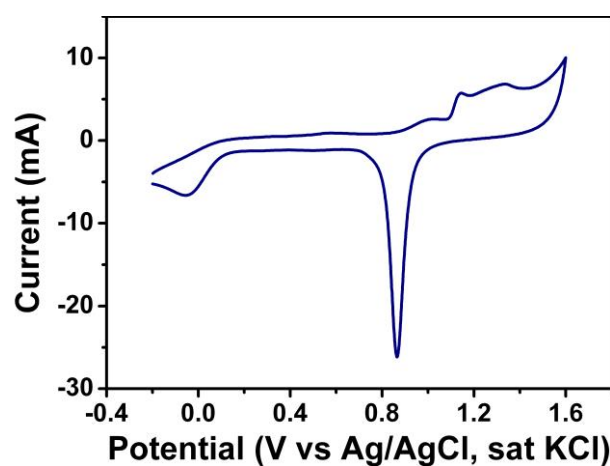


**Figure A.2:** Typical cyclic voltammogram in 0.1 M H<sub>2</sub>SO<sub>4</sub> at 100 mV.s<sup>-1</sup> measured at a 1 mm radius gold macrodisc electrode.

### A3. Peer Reviewed Publications

1. **Wahl, A.**; Dawson, K.; O'Riordan, A., Nanomolar Trace Metal Analysis of Copper at Gold Microband Arrays. *Journal of Physics: Conference Series* **2011**, 307 (1), 012061.
2. **Wahl, A.**; Dawson, K; MacHale, J; Barry, S; Quinn, A.J and O'Riordan, A, 'Gold Nanowire Electrodes in Array: Simulation Study and Experiments', *Faraday Discussions*, 164, 377 (**2013**)
3. **Wahl, A.**; Barry, S; Dawson, K; MacHale, J; Barry, S; Quinn, A.J and O'Riordan, A, 'Electroanalysis at Ultramicro and Nanoscale Electrodes: A Comparative Study', *Journal of The Electrochemical Society*, 161 (2) B1-B6 (**2014**)
4. K. Dawson, **A. Wahl**, R. Murphy and A. O'Riordan, 'Electroanalysis at Single Gold Nanowire Electrodes', *Journal of Physical Chemistry C*, 116, 14665 (**2012**).
5. Dawson, K; **Wahl, A.**; Pescaglioni, A; Barrett, C; Iacopino, D and A. O'Riordan 'Gold Nanowire Electrode Arrays: Investigations of non-Faradaic Behaviour' (**2013**)
6. Dawson, K.; **Wahl, A.**; Barry, S.; Barrett, C.; Sassiati, N.; Quinn, A. J.; O'Riordan, A., Fully integrated on-chip nano-electrochemical devices for electroanalytical applications. *Electrochimica Acta* **2014**, 115, 239-246.

### A4. Conferences Attended

1. Institute of Physics: Sensors & their Applications XVI, Tyndall National Institute, Cork, Ireland (*Oral Presentation*), **2011**
2. Royal Society of Chemistry: Electrochem, Dublin (*Oral Presentation*), **2012**

3. Royal Society of Chemistry: Faraday Discussions 164 “Electroanalysis at the Nanoscale”, Durham (*Oral Presentation*), **2013**

4. Royal Society of Chemistry: Electrochem, Southampton (*Oral Presentation*), **2013**

## **A5. Awards**

1. First place, Poster presentation at Institute of Physics: Sensors & their Applications XVI, Tyndall National Institute, Cork, Ireland (*Oral Presentation*), **2011**